

Three-dimensional facial measurement
by portrait holography
and texture-based focus detection

I n a u g u r a l - D i s s e r t a t i o n

zur
Erlangung des Doktorgrades der
Mathematisch-Naturwissenschaftlichen Fakultät
der Heinrich-Heine-Universität Düsseldorf

vorgelegt von
Susanne Frey
aus Erlangen

Düsseldorf
2005

Referent: Prof. Dr. P. Hering
Korreferent: Prof. Dr. G. Pretzler

Tag der mündlichen Prüfung: 7.7.2005

Gedruckt mit der Genehmigung der Mathematisch-Naturwissenschaftlichen Fakultät der
Heinrich-Heine-Universität Düsseldorf

Kurzfassung

Die vorliegende Arbeit behandelt das Problem der automatischen dreidimensionalen Gesichtsvermessung unter Verwendung des reellen Bildes eines analogen Hologramms durch die Detektion des Bildkontrastes, der durch die natürliche Struktur der Hautoberfläche entsteht. Damit ist es zum ersten Mal möglich, digitale Modelle von Gesichtsoberflächen aus Portraithologrammen zu erstellen, die eine hochauflösende Textur beinhalten, die pixelgenau der Oberfläche zugeordnet werden kann. Die vorgestellten Verbesserungen des Systems ermöglichen zudem augensichere Aufnahmen des Gesichts. Diese beiden Aspekte sind von entscheidender Bedeutung für das Hauptanwendungsgebiet der holografischen Gesichtsvermessung, nämlich die Planung und Bewertung von Operationen in der Mund-, Kiefer- und Gesichtschirurgie.

Die Aufnahmen von Portraithologrammen werden mit einer holografischen Kamera durchgeführt, die mit einem gepulsten Laser arbeitet. Das reelle Bild der Objektwelle wird optisch rekonstruiert. Schnittbilder des dreidimensionalen reellen Bildes des Portraithologramms werden digital aufgezeichnet und numerisch ausgewertet.

Das optische Auslesen des Hologramms wird im Rahmen dieser Arbeit durch die Kompensation von Abbildungsfehlern verbessert. Durch die so erreichte laterale Auflösung im reellen Bild ($<100\mu\text{m}$) ist es möglich, einzelne Hautporen der Gesichtsoberfläche kontrastreich darzustellen. Damit kann die bisher notwendige Musterprojektion zur Kontrastverstärkung vermieden werden. Das hat den entscheidenden Vorteil, dass Streuscheiben zur Beleuchtung des Gesichts verwendet werden können, wodurch Augensicherheit bei der Aufnahme der Hologramme erreicht wird. Die Aufnahme der Schnittbilder des reellen Bildes wird verbessert, indem die bisherige Abbildung der Schnittbilder mittels einer Streuscheibe durch ein direktes Einlesen der Schnittbilder mit einem CMOS Dokumentenscanner ersetzt wird. Weiterhin wird ein komplementäres Schema zur Bestimmung der Objekt Oberfläche aus dem Hologramm untersucht, das auf Interferenz zwischen dem Referenzstrahl und dem virtuellen Bild des Referenzstrahls beruht.

Zur Gewinnung der Objekt Oberfläche aus einer Schnittbildserie des reellen Bildes wird digitale Bildverarbeitung angewendet. Ein Standardverfahren zur Fokusedetektion ist Kontrastmaximierung in einer lokalen lateralen Pixelumgebung. Ein solches Verfahren wird in Verbindung mit räumlicher Filterung zur Reduzierung von unscharfen Überlagerungen und Bildrauschen auf die holografischen Daten angewendet. Die Ergebnisse werden mit denen eines neu entwickelten Ansatzes verglichen, der auf der Detektion axialer Fokuseigenschaften beruht. Kontrastmaximierung liefert aufgrund der guten Robustheit gegenüber Bildrauschen eine gute Annäherung an die gesuchte Oberfläche. Das Ergebnis kann dann durch axiale Fokusedetektion deutlich verfeinert werden.

Als Ergebnis der beschriebenen Prozedur werden texturierte Computermodelle der Gesichtsoberfläche gewonnen. Als Textur, die den Modellen zugeordnet wird, dient die Helligkeitsinformation aus dem reellen Bild an der Stelle der detektierten Oberfläche. Zudem ist es nun auch möglich, Computermodelle aus Spiegelbildern zu erstellen, die im Hologramm aufgenommen werden. So können beispielsweise drei Ansichten eines Gesichts in einem einzigen Hologramm zeitgleich aufgezeichnet und anschließend drei Computermodelle der Teilansichten gewonnen werden. Grundsätzlich lassen sich so auch Panorama-Aufnahmen eines Gegenstandes in einem einzigen Hologramm erfassen, wie anhand eines Testobjekts gezeigt wird.

Schließlich werden Anwendungsbeispiele präsentiert. Als typische medizinische Anwendung wird eine Epithesenanpassung vorgestellt. Die holografische Technologie kann künftig unter Verwendung einer mobilen Holografiekamera in größerem Maßstab in Kliniken eingesetzt werden. Eine Anwendung aus dem Bereich der Archäologie wird präsentiert. Außerdem wird anhand eines konkreten Falls gezeigt, dass Weichgewebedaten aus holografischer Gesichtsvermessung zur Bewertung verschiedener Verfahren der forensischen Gesichtsrekonstruktion verwendet werden können.

Abstract

This work presents three-dimensional metrology of the facial surface by detection of the natural skin contrast that appears in the real image of an analogue portrait hologram. For the first time, a holographic surface measurement method is presented that provides facial computer models including a high resolution texture that precisely matches the object surface. Furthermore, the presented improvements allow for eye-safe recordings of faces. Both aspects are crucial for the main purpose of holographic facial measurement, which is planning and evaluation of cranio-facial surgery.

A holographic camera comprising a pulsed laser system is used to record portrait holograms. The real image of a portrait hologram is reconstructed optically. The real image volume is digitized by scanning projections of the real image. Digital image processing is applied to these sectional images to retrieve the object surface.

The optical reconstruction of the holographic real image is improved in this work by introducing a set-up that allows to compensate for image aberrations. High image resolution ($<100\mu\text{m}$) is achieved and hence skin pores appear in the real image and may be detected numerically. Thus pattern projection which was used in earlier work to enhance the image contrast becomes unnecessary. Consequently, it is possible to use diffusor plates to illuminate the face leading to eye-safe recordings. Digitization of the real image is improved by replacing the previous intermediate imaging step on a diffusing screen by a direct scan of the real image with a CMOS line scanner. Furthermore, a complementary focus detection scheme is investigated that uses interference between the original reference beam and the virtual image of the reference beam as focus measure.

Digital image processing is applied to detect the object surface in the scanned real image volume. A standard *Shape-from-Focus* technique uses contrast maximization in a local lateral pixel neighborhood. Such a procedure is tested in combination with spatial filtering for image deblurring and noise reduction. The results are compared to those of a newly developed focus detection method based on axial focus features. Contrast maximization yields a good first approximation to the object surface and features a preferable robustness against image noise for large local pixel neighborhoods. It is demonstrated that a detected surface may be refined by axial focus detection for improved quality concerning surface smoothness and resolution.

Three-dimensional facial models result from the described procedure. The intensity information from the real image at the position of the detected surface serves as high resolution texture information that is added to the surface models. Because this texture is taken from the real image of the hologram it matches the surface precisely without an intermediate registration step. It is also possible to gain computer models from mirror images that are recorded in the hologram. Textured computer models of a frontal view and two side views of a sitting person are presented which are recorded in a single shot hologram. In general, mirror arrangements may provide panoramic imaging in a single hologram as shown for a test object.

Examples of applications of holographic facial measurement are presented. The adaption of an epithesis is given as an example of a medical application. The holographic technology may in future be used in hospitals employing a new mobile holographic camera. An example of archaeological imaging is presented. Finally it is shown that holographic facial measurement may contribute to the improvement of forensic facial reconstructions. The face of a real living person is reconstructed from medical CT data by several methods, and a holographic facial model of the person is used to evaluate the results.

Contents

1	Introduction	1
1.1	Scientific holographic imaging	2
1.2	Medical facial imaging	4
1.3	Preceding work	5
1.4	Structure of the thesis	6
2	Theory of holographic imaging	8
2.1	Wavefront recording and reconstruction	9
2.1.1	Plane and volume holograms	9
2.1.2	In-line and off-axis holography	11
2.1.3	Resolution of the recording material	11
2.1.4	Intensity distribution on the hologram plate	11
2.1.5	Amplitude and phase holograms	12
2.1.6	Wavefield reconstruction	14
2.1.7	Diffraction efficiency	14
2.2	Laser source requirements	16
2.2.1	Complex degree of coherence	16
2.2.2	Fringe visibility	16
2.2.3	Spatial and temporal coherence	17
2.2.4	Laser requirements for hologram read-out	18
2.3	Imaging equations and aberrations	18
2.3.1	Wavelength shift and scaling	23
2.4	Summary	24
3	Experimental implementation of holographic facial measurement	26
3.1	Holographic camera	28
3.1.1	Single-frequency pulsed laser system	30
3.1.2	Mobile holography	31
3.2	Eye-safe recording of portrait holograms	32
3.3	Mirror images	34
3.3.1	Lying objects	35
3.3.2	Side views	35
3.3.3	Panoramic imaging	37
3.4	Hologram processing	37
3.4.1	Automated system	39
3.5	Optical hologram read-out	40
3.5.1	Alignment	40

3.6	Digital recording of image projections	43
3.7	Surface identification by reference beam detection	48
3.7.1	Experimental set-up	49
3.7.2	Diffuse object	51
3.7.3	Phase shifting signals	53
3.8	Summary	57
4	Shape-from-focus in the real image	59
4.1	Focus features and geometry	60
4.1.1	Image representation and pre-processing	63
4.2	Image deblurring	64
4.2.1	Fourier-based filtering	65
4.2.2	Spatial filtering	68
4.3	Contrast maximization	69
4.4	Focus detection based on axial features	70
4.4.1	Contours	75
4.4.2	Symmetry	76
4.5	Results and discussion	78
4.5.1	Data noise	79
4.5.2	Smoothness of the reconstructed surfaces	80
4.5.3	Textured facial models	83
4.5.4	Mirror images	86
4.6	Summary	86
5	Fields of applications	89
5.1	Medical facial measurement	89
5.2	Imaging cultural heritage	91
5.3	Forensic facial reconstruction	92
6	Summary	98
6.1	Future developments	100
A	Seidel aberrations in holographic imaging	101

Chapter 1

Introduction

The subject of this work is three-dimensional metrology of the facial surface by detection of the natural skin contrast that appears in the real image of a portrait hologram. Analogue pulsed holography is used to record the portrait hologram. The method provides precisely textured facial computer models for planning and evaluation of cranio-facial surgery. Due to the nature of facial surface measurement for surgery planning in a clinical environment, sub-mm resolution must be provided, highly recognizable facial computer models are needed and thus, texture must be included in the facial models. The system operating in a clinical environment should be characterized by easy handling for the operator and the patient alike. Furthermore, eye-safety and a short recording time to prevent movement artifacts are crucial for such a system.

As an example of reviews on three-dimensional imaging systems see [Bla04] and [CBS00], for instance. Commonly used apparatuses for facial metrology are photogrammetric systems, laser scanners and range sensors based on fringe projection [D'A], [otFifAOI01]. There are certain weaknesses inherent with these systems, leading to sub-optimal results of the digitized surfaces: Range sensors based on laser scanning and fringe projection would provide sufficiently high image quality, but only assuming a perfect relative stability between the object and the scanner. Unfortunately, the scan duration increases with the required image resolution, leading to serious distortions of the reconstructed surfaces for moving objects. This has been studied in [BPG], for instance, proposing speed and acceleration compensation for each point of the model by recursively optimized motion estimation of the object surface, for a moving rigid object. Nevertheless, changing facial expressions and larger movements of patients have to be dealt with in a clinical environment. A fast recording time is the main advantage of photogrammetric systems. Such systems use a set of digital images of an object from different perspectives to calculate the shape of a facial surface by finding correspondences in these images. This is usually supported by pattern projection, as the natural image contrast is insufficient for reliable feature detection [D'A].

Still, in practice, these systems are fast, but the resulting quality of the models appears critical for medical use [Bon02].

Therefore, in order to provide a physical solution for three-dimensional metrology that offers both high image resolution and fast data recording, pulsed analogue holography with its precise imaging properties seems to be an optimal starting point, provided that the holographic information can be digitized in second step. An analogue hologram of (30×40) cm², recorded with a single frequency pulsed laser, can store and replay scenes of several cubic meters with an image resolution of a few μm . The system used in this thesis comprises a single frequency pulsed laser operating at the wavelength of 526.5 nm. The recording time is determined by the pulse duration of 35 ns. This prevents movement artifacts by unintended patient movements as well as by instabilities of the measurement environment.

While holographic cameras for portrait holography are at hand, the real image of a portrait hologram has to be reconstructed with high accuracy and image contrast, even though the image volume which has to be evaluated by far exceeds that of other common real image applications like holographic particle image velocimetry [MPPW04], [HZL85]. Based on the optical reconstruction of the real image, a projection imaging technique and numerical procedures for digital image processing are developed to recover a precisely textured facial model from the hologram.

1.1 Scientific holographic imaging

A hologram is the recording of the intensity of an interference pattern formed by two coherent superimposed waves. Given the hologram and the knowledge of one of the two beams (called reference wave), the second wavefront can be replayed from the hologram. A characteristic of a hologram is the potential to store arbitrary phase fronts of waves that are scattered by an object (the object wave), and to reconstruct the phase fronts to form a virtual or a real image of an object. Thus, when suitably illuminated, the hologram can focus a wavefront into the position where the object was during recording. This is a very general approach, and, accordingly, the number of variations and applications of the holographic principle which evolved since the first discovery in 1948 by Dennis Gabor [Gab48] is enormous and will not be covered here.

There are, however, some fundamental steps that affect most fields of holography and the presented system in particular. Leith and Upatnieks introduced *off-axis holography* using lasers for hologram recording [LU62], [LU63]. Pulsed laser systems made it possible

to record moving objects and living people holographically and led to the establishment of eye-safe human portrait holography [BHWB65], [Sie67], [Sie68], [Ans70]. Gabor's motivation to develop the concept of holographic imaging was to overcome a problem in electron microscopy: The resolution of electron microscopy systems was not limited by the wavelength but strongly degraded by spherical aberration of electron lenses. It was Gabor's idea to record the aberrated image holographically, and then, in a second step, to reconstruct the image optically and correct the distortions [Gab48], [Gab49]. Even though this concept was not implemented successfully, a key feature of holography is that it works without lenses. This feature and also the development of suitable light sources have led to an increasing use of holography, in cases where the fabrication of diffractive optics limits the resolution of an imaging system, such as in the x-ray regime [WYJ03], [S+03]. For example, recently, random magnetic structures were imaged holographically with an image resolution of 50 nm using x-rays from spectrally and spatially filtered synchrotron radiation at a wavelength of 1.59 nm [ELS+04].

X-ray microscopy for high resolution imaging of biological specimen has been implemented successfully even yielding three-dimensional information by computed tomography [WSN+00]. The employment of pulsed micro-holography with x-rays in this field, for example to image a living cell, would allow to examine cell structures in their natural environment and may provide improved resolution [SBHR90].

Aside from applications for electron or x-ray imaging, holography at optical wavelengths has a strong impact, because at these wavelengths, lasers provide coherent light sources that allow for large scale imaging. The holographic system presented in this work can be regarded as a real image application of optical holography. As mentioned above, the hologram replays the object wave as real image. Established applications of this real image are the study of particles or bubbles in an image volume, which is recorded holographically on an analogue recording material, and then read out optically. The three-dimensional real image is projected onto a digital light sensor which scans the field. Numerical processing is then used to examine the density and size of certain structures in the image volume (see [HZL85], [HL80]). Further development of this system leads to the active research area of digital holographic particle image velocimetry [Hin02], [PM]. A further example of real image applications is holographic optical tweezers [Gri03], [JFBRM04]. Optical tweezers use forces induced by intensity gradients in strongly focused beams of light to trap and to manipulate particles. Computer generated holograms are used to tailor optical fields for variable trapping patterns. In this way, a system may be probed at many points simultaneously. Liquid crystal spatial light modulators can be employed to form holograms dynamically and apply sequences of trapping patterns to the system under study.

In the holographic imaging system considered here, the real image of the hologram is

projected onto a digital scanning unit and sectional images of the real image volume are recorded and evaluated by digital image processing to extract precisely the shape of the surface that is recorded on the hologram. The fast recording time and the high image resolution of the hologram are used to meet the medical requirements of the measurement. To image a high volume with sufficient resolution and image contrast from a hologram which is recorded in an eye-safe way and to process the data optically and numerically for surface detection are the main tasks to provide good performance of the system.

Before introducing preceding work on holographic facial measurement and the content of this thesis, the purpose - facial measurement - is summarized below.

1.2 Medical facial imaging

A detailed description of the medical need and use of facial surface data, benefiting from expanding modalities in digital imaging and digital image processing, is given in [Bon02]. Some central aspects of medical facial imaging are outlined in brief:

To plan and to evaluate the outcome of a surgical intervention, various imaging procedures are combined: The three-dimensional bone structure is measured by Computer Tomography (CT); soft tissue containing vessels, fat tissue, nerves and muscles, is visualized by Magnetic Resonance Imaging (MRI) or sonography [P+02]. In reconstructive surgery, not only is it important to recover the full functionality of the face, but also the esthetic result of a surgery is essential for a patient's rehabilitation. Therefore proper documentation of the surgery by precise three-dimensional facial measurement is indispensable in this field. Furthermore, there are a number of surgery methods that differ in the soft tissue behavior after the intervention while the bone structure is unaffected. To gain control over these effects and to find the best method, the three-dimensional surface of a patient has to be characterized in certain time intervals. Modeling of epitheses is another task that requires three-dimensional facial data.

In these cases, CT and MRI are inappropriate because of radiation damage (CT) or the high cost of operation and low image resolution (MRI) and surgeons fall back on industrial surface recording solutions such as line scanners, fringe projection or photogrammetric systems. These systems have the disadvantage either of long recording times leading to considerable movement artifacts, or a low image resolution. Both aspects ultimately lead to facial data that doesn't meet the resolution requirements in medical imaging and shows low recognizability of the models. Further aspects of this can be found in previous work [Bon02].

One aim of computer aided surgery is to make surgery results predictable by using multi-modal data in combination with mathematical methods [Bie03], [Gla02]. To develop and test these methods precise facial data has to be included in the simulations.

A different problem arises in the field of forensic medicine. It is often necessary to determine the appearance of a face from a skull for identification [R.P84]. In forensic science, such a reconstruction is needed for comparisons with photographs of missed persons, for example. Another example is to be found in archaeology. Reconstructions of faces of unearthed skulls are made to give a life-like picture of people from ancient times, so the viewing public in a museum can gain intimate contact with historical events.

There are several ways of recreating a face from a skull [Wil04]. To compare these methods with the aim of improving them, precise facial measurement combined with CT data is essential. A broad facial soft tissue data base would allow new highly automated ways for facial reconstructions.

Finally, three-dimensional imaging of the facial surface with a μm resolution can be used to study the behavior of skin pores under the influence of cosmetic treatment.

Besides these medical applications, the main problems that appear in the task of facial measurement, such as recording speed, handling of reflexes and varying reflectivities, shading, high accuracy and easy handling are crucial for many industrial application as well, which are of course not excluded from consideration.

The general feasibility of pulsed holography for medical tasks has already been demonstrated in preceding work on holographic surface measurement, which is reviewed in the following section.

1.3 Preceding work

As reported in [Bon02] facial measurement was implemented successfully in former work by the *Holography and Laser Technology* group at the *caesar* foundation in Bonn (*caesar* stands for *Center of Advanced European Studies and Research*). The replayed real image was dissected by a diffusing screen. The real image projections were recorded on a CCD camera. The recorded surface was extracted from the projection sequence by maximization of a local contrast measure. In order to achieve sufficient image contrast in the real image, the object illumination beam was modulated so as to project a high contrast pattern onto the facial surface of the patient. This work was followed by a detailed analysis of the

system with special emphasis on numerical data processing [Gie03], including a feasibility study of inverse filtering techniques from extended focus microscopy for the analysis of the holographic real image projections. Furthermore, the influence of moving apertures and additional aperture by added mirrors was discussed. Contrast maximization for surface detection was successfully improved by [The03], by iterative compensation of off-axis effects in the numerical data processing.

Based on this work, this thesis presents an optical and numerical procedure, which works without the need for pattern projection, leading to a simplified recording step and providing eye-safety. These features are essential for the employment of the system in a hospital environment. Furthermore, it offers precise high resolution texture of the models and the option of including mirror images and panoramic images in single shot holographic recordings.

1.4 Structure of the thesis

In effect, there are three main sources for the necessity of contrast enhancing pattern projection. These are image distortions in the optical read-out of the hologram, image noise introduced in the digitization step of the holographic projections and misinterpretation of the digitized image volume during digital image processing.

The first may be considered in more detail. The hologram is recorded by coherently superimposing the object wave with a reference wave. To reconstruct the hologram information optically, as in the particular case here, an exact copy of the phase conjugate reference wave has to be generated. Due to the large aperture of the holographic recording, this step is very sensitive even to small deviations of the reconstructive wavefront. Special arrangements have to be made to avoid degraded image quality concerning image resolution and image contrast.

Secondly, regarding the digitization unit, a digital detection has to be installed which allows for efficient noise suppression and filtering for clearly distinguishable image contrast originating from the natural facial texture in the focused regions of the facial surface. To achieve this, the combination of a diffusing screen and a CCD camera has been replaced by a direct scan of the real image with a CMOS line scanner, not only leading to improved imaging properties, but also avoiding calibration errors in the additional imaging step from the screen to the CCD chip.

In order to improve the numerical focus detection procedure and to make it work without contrast enhancing patterns, it has to be robust against fluctuations of the surface texture of the object affecting the size of the detected structures as well as their intensity. Contrast maximization and data filtering are refined by a flexible surface search strategy

which is adapted to this task.

For an in-depth presentation of these aspects, the thesis is divided into the following chapters:

Chapter 2 gives an overview of the basic mathematical formulation of holographic imaging which is, of course, regarding the wide variety of holographic systems and set-ups, strictly confined to essential aspects of the holographic system presented here.

In chapter 3, the experimental realization of hologram recording, high resolution projection imaging and image digitization is demonstrated. Possible extensions of the recording and the read-out geometry for panoramic imaging are presented. Finally, it is discussed in how far correlation signals of the reference beam can be utilized for the purpose of surface detection of a diffusely scattering object.

Numerical focus detection from projection image sequences is treated in chapter 4. The standard procedure of lateral contrast maximization is compared to a newly developed search strategy that solely relies on axial focus features. The chapter closes with a presentation of results, showing textured facial models retrieved from portrait holograms.

Selected applications in facial reconstructive surgery, archaeology and forensic science are presented in chapter 5.

Chapter 6 provides a summary and conclusion of the thesis.

Chapter 2

Theory of holographic imaging

Holography is a method for wavefield recording: The phase and the amplitude of a wave are stored on photosensitive material. This is accomplished by superimposing the wave that is studied (the object wave) onto a coherent background wave (reference wave) in the plane of the recording medium. The intensity distribution of the interference pattern of the two waves is recorded. This is depicted in Fig. 2.1 (a) for a plane reference beam and a spherical object beam that interfere on a photographic plate H . The read-out offers two options, as shown in Fig. 2.1 (b) and (c): The object wave can be reconstructed optically from the recorded interference pattern, either as virtual image (Fig. 2.1 (b)) or as real image (Fig. 2.1 (c)). For the reconstruction of the object wave, both the interference pattern and the phase front of the reference wave used for the recording must be known. To gain the virtual image of the hologram, it is illuminated with the reference wave. In this case, the hologram acts as a window, and the viewer sees the object behind the hologram plate. The virtual image is a divergent wave. In contrast, the real image is a convergent image forming wave, the phase conjugate object wave. To display the real image the hologram is illuminated with the phase conjugate reference wave.

In the application presented here, the real image of a hologram is used for surface measurement. This is done by high resolution digital projection imaging of the real image and digital image processing. The aspects of digital image processing are not mentioned here and are dealt with in chapter 4. This chapter and the next describe the optical implementation of holographic imaging.

In the following paragraphs, several terms and dependent factors are pointed out which affect the optical holographic recording and reconstruction of a scene with the aim of projection imaging of the holographic real image. This is done following the comprehensive presentation of theoretical and practical issues of holography in [CBL71] and [Har96], and the theoretical discussion on optics given in [BW02] and [LKW99]. A high image quality has to be achieved according to the parameters of image contrast, brightness and reso-

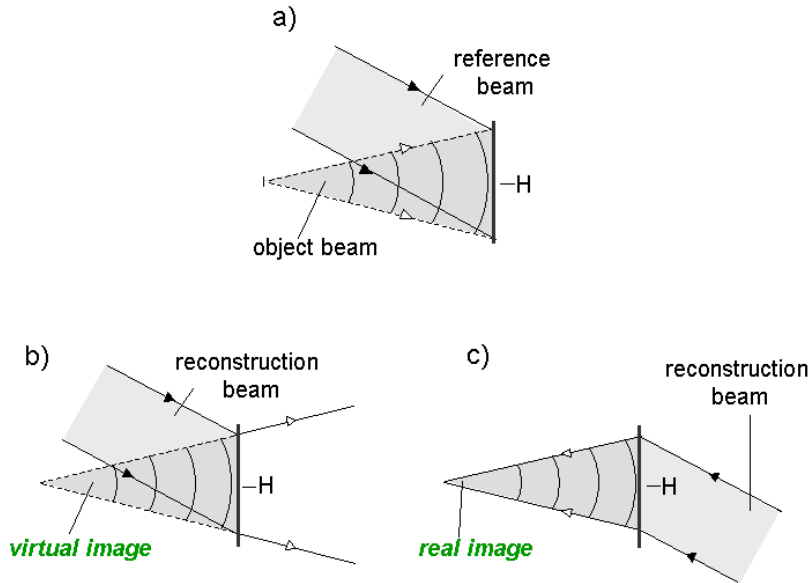


Figure 2.1: (a) A spherical object wave is coherently superimposed with a reference wave on a photographic plate. The recorded interference pattern is called hologram (H). (b) The object wave is reconstructed as a virtual image by illuminating the hologram with the reference wave. (c) The object wave is reconstructed as a real image, if the hologram is illuminated with the phase conjugate reference wave.

lution in a large image volume of up to $\approx 1m^3$. To achieve this, hologram parameters and processing have to be optimized, and the laser parameters for the recording and the reconstruction are affected, too. To gain high resolution, image contrast and accuracy in the replayed real image, minimization of image aberrations is crucial.

In the next section, basic aspects of hologram recording and reconstruction are presented. Laser source requirements for the recording and the read-out of the hologram are discussed in section 2.2, and section 2.3 addresses image aberrations.

2.1 Wavefront recording and reconstruction

The holograms used in this work are plane off-axis phase holograms. This term is explained in the following sections, and the basic imaging properties of the hologram are derived.

2.1.1 Plane and volume holograms

The general formation of the hologram in the photographic emulsion is sketched in Fig. 2.2 for two plane waves (beam 1 and beam 2) and an emulsion thickness h . The waves

impinge on the photographic plate forming the angle γ . The distance d between the fringes in the resulting interference pattern is determined by

$$2d\sin(\gamma/2) = \lambda. \quad (2.1)$$

In the holographic camera used in this study two waves of the wavelength $\lambda = 527$ nm interfere at an angle γ of 56 degrees (see section 3.1). This corresponds to a fringe spacing of $0.6 \mu\text{m}$. Taking into account the emulsion thickness of $\approx 10 \mu\text{m}$ the hologram formed can not formally be regarded as two-dimensional. Still, the angle between the two beams that form the interference pattern has a strong influence as well: The direction of the interference pattern follows the bisecting line of the angle γ .

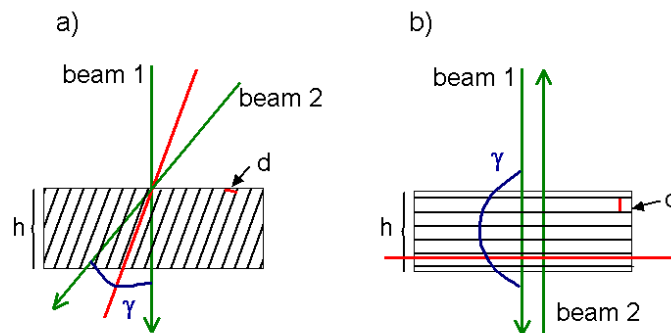


Figure 2.2: The direction of the interference pattern formed by the coherent plane waves beam 1 and beam 2 follows the bisection line of the angle γ . Therefore, despite the fact that the fringe spacing d is smaller than the emulsion thickness, the hologram with a recording geometry as shown in part (a) is considered as a plane hologram. The recording geometry shown in part (b) demonstrates the special case where $\gamma=180$ degrees as example of a recording geometry that creates a volume hologram.

Two cases are shown in Fig. 2.2: The different orientation of the interference patterns for changing beam geometries leads to a different behavior in the hologram read-out. The interference pattern turns into a reflecting Bragg grating if the two waves impinge on the hologram plate from opposite sides, as shown in part (b). In this case, the thickness of the hologram is a decisive parameter in the description of the hologram, and such holograms are called volume holograms (see Fig. 2.2). Volume holograms can be read out with white light. This characteristic leads to the useful application of display holography for exhibition of portraits or cultural heritage (see chapter 5).

For facial measurement, which is the primary purpose of the holographic set-up, holograms are recorded as shown in part (a) of Fig. 2.2. The important hologram features of such a recording are met by the assumption of a plane hologram, which is therefore taken as theoretical framework.

2.1.2 In-line and off-axis holography

The hologram geometry used in our set-up corresponds to *off-axis holography*. In this case, an angle is introduced between the reference beam and the object beam as depicted in Fig. 2.1(a). In contrast, *in-line holography* refers to a set-up with the reference wave and the object wave both being placed on an optical axis given by the normal of the hologram plane [Gab48], [Gab49]. Then, the image forming wave in the reconstructed image is overlapped with zero-order contributions of the reconstructed wave (see below). To avoid this, an angle is introduced between the reference and the object wave [LU62], [LU63]. The off-axis method allows for separation of the diffracted waves with the set back of a higher spatial resolution that is needed in the recording material (see Eq. 2.1). Since analogue holograms are recorded on high resolution photographic emulsions, this aspect is not critical, as is explained below.

2.1.3 Resolution of the recording material

The limited resolution of the recording material can be treated as a cut-off spatial frequency. Structures in the interference pattern of spatial frequencies which exceed this cut-off frequency are not recorded on the hologram. The fringe spacing for two plane waves is given by Eq. 2.1. For an in-line geometry, maximum fringe spacing is achieved. The interference structure becomes finer with a growing off-axis angle of the reference beam. The object size also has to be taken into account: The finite size of an object leads to a skewness of the object light beams from off-axis object points relative to the hologram normal. For in-line holography, the tolerable object angle recorded by a CCD medium with a spatial resolution of $d=5 \mu\text{m}$ is according to Eq. 2.1 $\gamma \approx 6$ degrees. In comparison, the line spacing for an analogue recording medium is >3000 lines/mm, which corresponds to a spacing $d \approx 0.3 \mu\text{m}$. This results in a tolerable angle $\gamma \approx 120$ degrees. Therefore, holograms with an off-axis angle of 56 degrees for the reference beam can easily be recorded on analogue material. Large objects and a wide viewing angle of the recorded scenes can also be imaged.

2.1.4 Intensity distribution on the hologram plate

Holography is a two-step technique for imaging a wave field scattered by an object. The first step is the recording of the amplitude and phase of this object wave. To access the phase information, the object wave is coherently superimposed onto a second wavefield which can be considered as a coherent background. The phase information of the object wave is written onto this coherent background. The two waves interfere and form the diffraction pattern called hologram H . It is recorded on photo sensitive material or on a

digital light sensor.

The light fields, oscillating at the frequency f are of the form

$$\underline{\mathbf{v}} = \underline{a} \exp(i\varphi) \exp(2\pi i f t) = \underline{\mathbf{a}} \exp(2\pi i f t). \quad (2.2)$$

In the following, the waves are assumed as linearly polarized waves propagating in z -direction, so scalar notation is used:

$$\mathbf{v} = a \exp(i\varphi) \exp(2\pi i f t) = \mathbf{a} \exp(2\pi i f t). \quad (2.3)$$

Bold letters mean complex variables. Monochromatic waves are assumed, so the time varying factor is suppressed. The wavefields are then described by their complex amplitudes \mathbf{a} . The subject of partial coherence is addressed later (see section 2.2.1), at which point this simplification is no longer valid, and the field will be described by Eq. 2.3.

Referring to the hologram geometry, the complex amplitude \mathbf{a} is substituted by the letters

- o** object wave
- r** reference wave
- c** reconstruction wave
- i** image wave
- h** electromagnetic field in the hologram plane.

The cartesian coordinate system (x, y, z) is chosen with the hologram in the plane $z=0$. For points (x, y) on the hologram the field \mathbf{h} is given as sum of the object wave and the reference wave

$$\mathbf{h}(x, y) = \mathbf{r}(x, y) + \mathbf{o}(x, y). \quad (2.4)$$

(The spatial variables (x, y, z) are dropped in some expressions for the sake of readability.) Accordingly, the intensity I becomes

$$I = \mathbf{h}\mathbf{h}^* = (\mathbf{r} + \mathbf{o})(\mathbf{r} + \mathbf{o})^* = \mathbf{r}\mathbf{r}^* + \mathbf{o}\mathbf{o}^* + \mathbf{r}^*\mathbf{o} + \mathbf{r}\mathbf{o}^* = a_r^2 + a_o^2 + 2a_r a_o \cos(\varphi_o - \varphi_r) \quad (2.5)$$

with $*$ meaning complex conjugation.

2.1.5 Amplitude and phase holograms

To record the intensity pattern given by Eq. 2.5, a photographic plate is placed in the hologram plane.

The exposure $B(x, y)$ on the hologram plate in the position (x, y) is determined by the time t_b of the exposure and the intensity $I = a^2$

$$B(x, y) = \int_0^{t_b} I(x, y, t) dt. \quad (2.6)$$

This exposure leads to a complex transmission factor $\tau(x, y)$ of the plate in (x, y) which is defined as the ratio of the complex amplitude \mathbf{a}_2 behind the plate to that of an incident wave \mathbf{a}_1 :

$$\tau(x, y) = \frac{\mathbf{a}_2}{\mathbf{a}_1} = T(x, y) \exp[i\varphi(x, y)]. \quad (2.7)$$

For pure absorption τ is a real number, otherwise a phase change occurs. The case $T = \text{constant}$ corresponds to a *phase hologram*, $\varphi = \text{constant}$ to an *amplitude hologram* (also called *absorption hologram*).

In the following, uniform intensity over the exposure time t_b is assumed. Additionally, the phase or the amplitude transmission are assumed as linear functions of the exposure B over a certain exposure range for the respective hologram type. This is depicted in Fig. 2.3 for an absorption hologram. The transmission in this case is of the form

$$T = \text{const} - mB. \quad (2.8)$$

For a phase hologram, the corresponding relation is

$$\varphi(I) = \text{const}' - m'B. \quad (2.9)$$

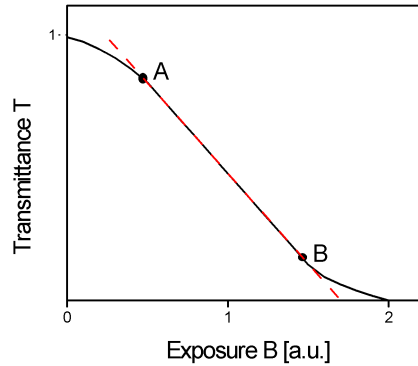


Figure 2.3: The amplitude transmission is depicted against the exposure. The curve is considered linear between A and B.

2.1.6 Wavefield reconstruction

For the optical reconstruction of the object wave the hologram is illuminated with a read-out laser beam \mathbf{c} . The image wave \mathbf{i} emerges from the hologram plate (for an absorption hologram):

$$\mathbf{i} = T * \mathbf{c} = \underbrace{c_0 \mathbf{c}}_{(0)} + mt_b (\underbrace{\mathbf{crr}^*}_{(1)} + \underbrace{\mathbf{c oo}^*}_{(2)} + \underbrace{\mathbf{cr}^* \mathbf{o}}_{(3)} + \underbrace{\mathbf{cro}^*}_{(4)}). \quad (2.10)$$

The real image of the hologram is obtained without distortion for $\mathbf{c} = \mathbf{r}^*$. The rays of the phase conjugate reference wave in any plane are anti-parallel to the rays of the reference wave. With a divergent spherical reference wave, the phase conjugate wave is a spherical convergent wave. The indicated parts of Eq. 2.10 for $\mathbf{c} = \mathbf{r}^*$ become

- (0) $c_0 \mathbf{r}^* \propto \mathbf{r}^*$,
- (1) $\mathbf{r}^* \mathbf{r} \mathbf{r}^* \propto \mathbf{r}^*$,
- (2) $\mathbf{r}^* \mathbf{oo}^* \propto \mathbf{r}^*$,
- (3) $\mathbf{r}^* \mathbf{r}^* \mathbf{o}$,
- (4) $\mathbf{r}^* \mathbf{ro}^* \propto \mathbf{o}^*$.

Term (4) is of particular interest: It is proportional to the phase conjugate object wave. While the object wave is considered as superposition of diverging waves emerging from point sources at the object surface, this image wave is converging with all rays directed from the plate to the surface where it is focused and forming an image.

Terms (0),(1) and (2) are called zero-order terms and the corresponding waves have the same directions as the propagation direction of the reconstruction wave. Term (3) represents a modulated object light wave, which appears as a disturbed virtual image. When using \mathbf{r} as reconstruction wave, $\mathbf{c} = \mathbf{r}$, the virtual image appears undisturbed, while the real image is a modulated object signal and does not appear as the conjugate object image.

2.1.7 Diffraction efficiency

Another issue of practical relevance is the comparison between absorption holograms and phase holograms. Absorption holograms have some practical advantages over phase holograms: Firstly, they require less intensity for the recording procedure. The lower recording intensity makes the procedure safer and lowers the required laser energy. Considering the photo chemistry involved, phase holograms end with a bleaching step, while absorption holograms undergo fixation in the final step. Photo chemistry is easily available commercially for fixation but not for bleaching. Nevertheless, phase holograms are the preferred

choice for this particular holographic application, due to their superior *diffraction efficiency*, which is explained below.

A bright reconstructed image is achieved by a high diffraction efficiency. The diffraction efficiency is defined as the ratio of the power diffracted into a first order wave to the power of the incident wave.

As mentioned above, the set-up in this study works with an off-axis recording geometry. The angle γ between the reference beam and the object beam (by a shift of the reference source along the x axis) corresponds to a certain fringe spacing (see Eq. 2.1). A skew plane reference beam $\mathbf{r} = r \exp(2\pi i \xi x)$, $\xi = \sin \gamma / \lambda$, and a normally impinging unmodulated plane object wave of the real amplitude o then form an interference pattern

$$I = \mathbf{o}^2 + \mathbf{r}^2 + 2\mathbf{o}\mathbf{r} \cos(2\pi\xi x). \quad (2.11)$$

Temporally uniform exposure has been assumed and intensity is considered instead of power. For an absorption hologram it follows from Eq. 2.8 and Eq. 2.11 that

$$T(x, y) = \text{const} + mI = \text{const} + m_1 + m_2 \cos(2\pi\xi x). \quad (2.12)$$

The constant term is the transmittance of the unexposed plate. Setting $\text{const} = 1$ leads to a transmission varying between 0 and 1 for $m_1 = m_2 = 1/2$.

$$T(x, y) = \frac{1}{2} - \frac{1}{2} \cos(2\pi\xi x) = \frac{1}{2} - \frac{1}{4} \exp(2\pi i \xi x) - \frac{1}{4} \exp(-2\pi i \xi x). \quad (2.13)$$

As the result, each first order has a maximum intensity of $\frac{1}{16}$ or 6.25 % of the incident wave intensity.

The same consideration can be applied to phase holograms.

A linear relation between exposure and phase shift $\varphi(x)$ is presumed, so that phase holograms can be treated in analogy to the above consideration:

$$\varphi(x) = m'_1 + m'_2 \cos(2\pi\xi x). \quad (2.14)$$

Making use of Eq. 2.9 yields

$$\tau = \exp(i\varphi(x)) \propto \exp(im'_2 \cos(2\pi\xi x)). \quad (2.15)$$

Developing this into a Fourier series and evaluation of the resulting terms results in a maximum diffraction efficiency of 33.9 %. Even though this superior diffraction efficiency has to be put in relation to the stronger image noise appearing for phase holograms due to a slight opacity in the emulsion after chemical processing, their high diffraction efficiency justifies their use for projection imaging.

2.2 Laser source requirements

The hologram is a diffraction pattern which consists of fringes that are formed by two interfering waves. Sufficient coherence of the light waves is an essential condition for the formation of a high contrast interference pattern.

Due to the strict stability requirements, short laser pulses have to be employed for human portrait holography [Bon02]. In this case, clearly, only partial coherence can be assumed. The degree of coherence of the waves can be related to the fringe visibility of the interference pattern on a screen. The fringe visibility is related to the intensity of the reconstructed image. Setting a limit in the tolerable decrease of image intensity due to imperfect coherence leads to a coherence condition for the light source. This procedure is outlined in the following paragraphs. Coherence requirements for the light source for real image reconstruction are addressed at the end of this section.

2.2.1 Complex degree of coherence

To specify the coherence conditions for hologram recording and real image reconstruction, the complex degree of coherence $\gamma_{12}(\tau)$ is introduced according to [CBL71](p.30)(Here, τ denotes a time interval.):

Two light waves are now represented by their complex electric fields \mathbf{v}_1 and \mathbf{v}_2 of the form Eq. 2.3 and monochromatic light is no longer assumed. The interference pattern intensity distribution 2.5 becomes

$$I = I_1 + I_2 + \langle \mathbf{v}_1 \mathbf{v}_2^* + \mathbf{v}_1^* \mathbf{v}_2 \rangle = I_1 + I_2 + 2Re[\langle \mathbf{v}_1 \mathbf{v}_2^* \rangle]. \quad (2.16)$$

Time average brackets $\langle \rangle$ have been added. The last term will be referred to as interference term.

The point of interference on the hologram plane is denoted Q . Two spatially separated apertures in front of the plane at P_1 and P_2 with corresponding electric fields \mathbf{v}_{P_1} and \mathbf{v}_{P_2} are considered. Following [BW02] the *complex degree of coherence* $\gamma_{12}(\tau)$ is defined as

$$\gamma_{12}(\tau) \equiv \frac{\langle \mathbf{v}_{P_1}(t + \tau) \mathbf{v}_{P_2}^*(t) \rangle}{[\langle \mathbf{v}_{P_1}(t) \mathbf{v}_{P_1}^*(t) \rangle \langle \mathbf{v}_{P_2}(t) \mathbf{v}_{P_2}^*(t) \rangle]^{1/2}}, \quad (2.17)$$

representing a normalized correlation of the fields at P_1 and P_2 .

2.2.2 Fringe visibility

A measurable quantity related to the degree of coherence is the fringe visibility V . It is defined as the contrast of the intensity distribution that is observed in the hologram plane

(This is a general contrast definition that will also be referred to in the context of focus detection in chapter 4):

$$V = \frac{I_{max} - I_{min}}{I_{max} + I_{min}}. \quad (2.18)$$

The mutual degree of coherence γ_{12} can be related to the fringe visibility by

$$V = \frac{2|\gamma_{12}|}{(I_1/I_2)^{1/2} + (I_2/I_1)^{1/2}}. \quad (2.19)$$

Assuming equal beam intensities, the fringe visibility value is equal to the degree of coherence. It is shown in [CBL71](p. 161) that the intensity of the reconstructed image is proportional to V^2 . Hence, requiring that the intensity loss due to imperfect coherence does not exceed 50 % of the image intensity with perfect coherence leads to the minimum tolerable degree of coherence $|\gamma_{12}| = 1/\sqrt{2}$.

2.2.3 Spatial and temporal coherence

Both, spatial and temporal aspects of coherence are included in Eq. 2.17. It is common to separate spatial and temporal coherence.

Spatial coherence $\mu_s(x, y)$ is covered by letting $\tau \rightarrow 0$. The meaning can be visualized in a set-up corresponding to *Young's* interference experiment ([LKW99](p. 40)).

Consideration of the optical path lengths for this set-up leads to a condition which relates the light source size L to the tolerable lateral distance d of two scattering points (or apertures) at distance R from the source that still cause sufficient fringe contrast on a screen that records the interference pattern. The larger the source size, the smaller the tolerable lateral distance of the scatterers becomes. Laser light that stems from any single transverse mode corresponds to a pointlike light source, thus provides spatial coherence over the full illuminated space.

τ is a transit time difference which defines an optical path difference $\Delta l = c\tau$ which is the temporal coherence length. Temporal coherence limits the size of the scene that can be recorded with the hologram set-up: Any transit time difference between reference and object light has to be less than the temporal coherence length of the laser. The limit of the temporal coherence length of a laser is determined by the spectral purity of the laser radiation. A laser oscillating at two longitudinal modes has a temporal coherence that is periodic in τ . This is mentioned here, because these *two-wavelength holograms* yield a contoured image, which has been used for surface measurement in other applications [HH65].

To achieve a coherence length of several meters with a pulsed laser, single frequency operation has to be assured. Chapter 3 will describe the laser design of the holography

set-up which is using careful mode selection and an oscillator amplifier set-up to meet these criteria.

2.2.4 Laser requirements for hologram read-out

The coherence requirements for the hologram read-out are lower than for the recording. The hologram size and the coherence of the reconstruction wave influence the resolution of the reconstructed image. In the holographic facial measurement application, the hologram is recorded with a single frequency pulsed laser system. The read-out of the hologram is performed in a second self-contained unit. The system has to be a commercialized product in the near future, and a read-out laser with lower coherence is more cost effective and therefore worth consideration. Moreover, laser speckle disturb the image reconstruction and are reduced as coherence degrades.

Industrial lasers provide operation at the spatial TEM₀₀ mode but have a comparatively small temporal coherence length (<1 cm). An estimation of the influence on the image resolution is made regarding path lengths as depicted in Fig. 2.4. The off-axis angle is $\gamma = 56^\circ$ in our application. The hologram extent is $h = 30\text{cm}$. The image point distance is assumed to be $z_i = 60\text{cm}$. The optical path difference over the extent of the hologram is

$$\Delta l = h \sin \gamma + (h^2 + z_i^2)^{1/2} - z_i \approx 32\text{cm}. \quad (2.20)$$

For temporal coherence exceeding this value, the resolution of the hologram is still diffraction limited. A lower temporal coherence corresponds to a lowered image resolution, determined by the corresponding aperture h that is still covered according to Eq. 2.20. A laser with a coherence length of 1 cm corresponds to $h \approx 12\text{mm}$. This yields a lateral image resolution of $x_{min} \approx 30\mu\text{m}$. With the assumed small aperture the axial resolution becomes $z_{min} \approx 2.6\text{mm}$. This is a comparatively low axial resolution, but it does not define the ultimate reachable resolution of the object surface detected in the real image if a suitable focus criterion, like axial point symmetry, is evaluated (see chapter 4 for details). Furthermore, the reduced laser speckle in the reconstruction with a low coherence source and the lower costs of such a system provide some advantages. For surface measurement of macroscopic objects, therefore, a low coherence laser may be a preferable alternative.

2.3 Imaging equations and aberrations

Three-dimensional measurements are carried out on the real image of the hologram. The real image is considered as a one to one copy of the object wave as conjugate image.

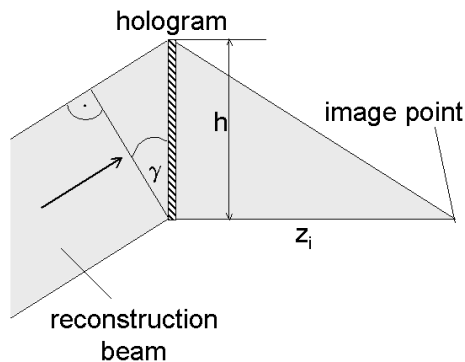


Figure 2.4: Optical paths in the image reconstruction arrangement.

Therefore, restraints in the resolution by aberrations are to be avoided because they limit the accuracy of the resulting measurement.

Furthermore, high image contrast is needed to detect the surface in the three-dimensional image volume, and for an aberration free image, image resolution is maximized and focused regions in the real image appear with significantly higher contrast than blurred image regions. Under these conditions, even small surface features such as - for facial measurement - the pores of the skin can be detected in the real image and allow for a three-dimensional reconstruction of the surface based on the surface texture, as shown in chapter 4.

To define a physical limit for the optical resolution of an aberration free reconstruction of the hologram, the analogy of an ideal lens is commonly used. The resolution is then limited by the imaging aperture given by the extent of the hologram or the radius of the illuminating laser beam during image recording/reconstruction.

For circular apertures the diffraction pattern consists of a concentric ring system. The central bright spot of this diffraction pattern is known as Airy disc ([LKW99], p.161). The resolution of an imaging system is defined as diameter A of the Airy disc. The radius of the circular aperture of the imaging system is denoted a and the wavelength of the light is referred to as λ . The numerical aperture $NA = n \sin \rho$ can be used to characterize the resolution. The angle ρ denotes the angular semi-aperture and n the refractive index.

According to [BW02](p.466) it follows for the lateral resolution that

$$|x_{min}| = 0.61\lambda/NA. \quad (2.21)$$

This yields a theoretical minimum distance of two object points that can still be resolved in the image. Assuming the refractive index $n=1$, an illumination radius $a=15$ cm, the wavelength $\lambda=526$ nm and a focal length $f=60$ cm, the numerical aperture of the holo-

graphic imaging system is $NA=0.25$, and $|x_{min}| \approx 1.3 \mu\text{m}$. An expression for the axial resolution is given by ([BW02], p. 491)

$$z_{min} \approx \pm 0.5\lambda(f/a)^2 = \pm 0.5\lambda/(NA)^2, \quad (2.22)$$

which results in $|z_{min}| \approx \pm 4.2 \mu\text{m}$ for the previously given parameters.

This assumes the following: optical replay of the object wave field with an exact reproduction of the phase of the reference wave (or the phase conjugate reference wave) as reconstruction wave, the absence of second-order variations in the emulsion thickness [AY71], [RA72] and the use of the same effective wavelengths during recording and reconstruction [FH98]. Any deviation from these assumptions leads to image aberrations. These aberrations are described by the analogy of aberrations of lenses, known as Seidel aberrations. The chosen arrangement for the mathematical description of the holographic images is given in Fig. 2.5.

The reference and reconstruction beam source, as well as object points and image points are given relative to the hologram plate, which is located in the (xy) plane, with the center in the origin of the coordinate system. A point source r_q is positioned in front of the hologram. The distance to the center of the hologram is referred to as R_q .

The subscript q is replaced by o for object points, i for image points, r for the reference beam and c for the reconstruction beam.

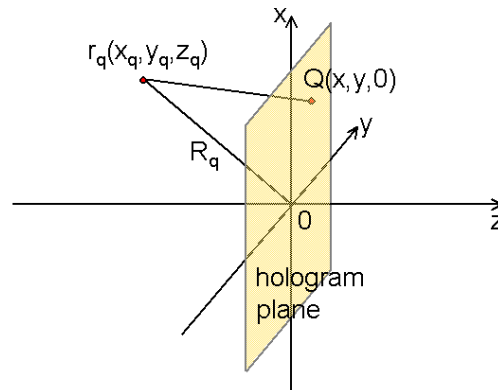


Figure 2.5: Arrangement for the description of phase front matching. r_q : point source. Q : point in the hologram plane

Wavefront matching The image wave \mathbf{i} emerges from the hologram as it is illuminated with the reconstruction wave \mathbf{c} according to Eq. 2.10. For the real image \mathbf{i}_R and the virtual

image \mathbf{i}_V , the relations

$$\mathbf{i}_V \propto \mathbf{cor}^* \quad (2.23)$$

and

$$\mathbf{i}_R \propto \mathbf{co}^* \mathbf{r} \quad (2.24)$$

apply.

For the study of aberrations, the concept of wavefront matching is introduced according to [Mei65]. The hologram of a point source with the electromagnetic field

$$\mathbf{E}_o = (A_o/r_o) \exp\{i(\frac{2\pi}{\lambda_o})r_o\} \quad (2.25)$$

is recorded. The reference wave \mathbf{r} and the read-out wave \mathbf{c} are regarded as emerging from point sources as well. The illumination of the hologram with the reconstruction wave leads to the image waves

$$\mathbf{E}_V = A_V \exp\{i(\frac{2\pi}{\lambda_c})r_c\} \exp\{i(\frac{2\pi}{\lambda_r})d\} \quad (2.26)$$

and

$$\mathbf{E}_R = A_R \exp\{i(\frac{2\pi}{\lambda_c})r_c\} \exp\{-i(\frac{2\pi}{\lambda_r})d\}, \quad (2.27)$$

with $d = r_o - r_r$. Intensity variations are neglected and in the following, only phase information of the waves is considered.

For an aberration free image, these image waves must be of the form

$$\mathbf{E}_i = A_i \exp\{i(\frac{2\pi}{\lambda_c})r_i\}, \quad (2.28)$$

which means the image waves are assumed to be spherical waves, either diverging (virtual image) or converging (real image), yielding a diffraction limited sharp image point.

Any deviation from optimal imaging can be expressed as phase differences from this *reference sphere* that surrounds the Gaussian image point.

Since all sources are assumed as point-like and intensity variation is neglected, the phases can be compared separately:

$$\Phi_V = \varphi_c + \varphi_o - \varphi_r \quad (2.29)$$

and

$$\Phi_R = \varphi_c - \varphi_o + \varphi_r. \quad (2.30)$$

Perfect aberration free image Expressions for these phases are obtained by considering path differences of the waves in the hologram plane

$$\varphi_o(x, y) = (2\pi/\lambda_o)d = (2\pi/\lambda_o)(r_oQ - r_oO) \quad (2.31)$$

$$= (2\pi/\lambda_o)[(x - x_o)^2 + (y - y_o)^2 + z_o^2]^{1/2} - (x_o^2 + y_o^2 + z_o^2)^{1/2} \quad (2.32)$$

for φ_o , and the other phases in the same manner. The points r_q , Q and O are given as shown in Fig. 2.5.

The square root terms are then expanded in a binomial series around z_q and the phase term of the actual wavefront in Eq. 2.30 is compared to that of a Gaussian reference sphere, which is found by considering only first order terms of the phase distribution over the hologram

$$\Phi = \frac{2\pi}{\lambda_c} \left[\frac{1}{2z_G} (x^2 + y^2 - 2xx_G - 2yy_G) \right]. \quad (2.33)$$

Again, here the coordinates (x, y) correspond to a point on the hologram plate. The coordinates of the *Gaussian image point* are (x_G, y_G, z_G) . Forcing Φ_R to be of the same form as Eq. 2.33 yields the holographic imaging equations for perfect first order imaging:

$$z_R = \frac{m^2 z_c z_o z_r}{m^2 z_o z_r - \mu z_c z_r + \mu z_c z_o} \quad (2.34)$$

and

$$x_R = \frac{x_c z_o z_r - \mu m x_o z_c z_r + \mu m x_r z_c z_o}{m^2 z_o z_r - \mu z_c z_r + \mu z_c z_o}, \quad (2.35)$$

where $\mu = \lambda_r/\lambda_c$, and m is an optional magnification of the interference pattern on the hologram. y_R is found by replacing the x-coordinates in Eq. 2.35 with the y-coordinates of the related waves and vice versa. The axial image distance z_R has to be a positive value to yield a real image by a convergent wave. For the case treated here, the reconstruction geometry requires $z_c = -z_r$ to account for the convergence of the reference wave and $z_o < 0$ [Mei65]). Assuming $\mu = m = 1$ this corresponds to a negative coordinate value, and hence to a converging image point at $z_R = -z_o$.

Aberrations The phase difference between the Gaussian reference sphere and the actual wavefront defines the aberrations of the image, which are essentially the same as for lens aberrations (see Appendix A for details), including spherical aberration, coma, astigmatism, field curvature and distortion.

Not only careful alignment of the reconstruction arrangement for precise generation of the reconstruction beam is found to be decisive for minimization of aberrations. Also the skewness x_c/z_c is a crucial parameter. The influence of the angle has also been studied in [BKV88], leading to the conclusion that, for image recording with plane waves, an angular

mismatch of the recording and reconstruction >1 mrad leads to notable image aberrations. The relation of misalignment and astigmatism has been illustrated in the experiment by [G.L52]: A linear zone plate is taken as an artificial hologram of a scattering line with *vertical* orientation. It is exposed to a parallel beam of light, forming a bright line image in its focal plane at distance f . If the hologram plane is rotated about an angle θ around the *vertical* axis and is no longer perpendicular to the incident light beam, the line focus is shifted to the position $f \cos^2 \theta$. If the hologram is rotated around the *horizontal* axis, the line focus is unaffected by the rotation. In conclusion, rotating the hologram even with more general patterns, hence changing the skewness of the beam, introduces astigmatism and can also be employed to compensate for unwanted astigmatism.

2.3.1 Wavelength shift and scaling

The only way to obtain a completely aberration free image in the presence of a wavelength shift is to compensate for it by magnifying the interference pattern on the hologram by the factor m so that $\mu = m$ [Mei65].

The wavelength shift between the recording and the read-out step in our application $\mu = \lambda_r/\lambda_c=(532/527)=1.01$, and the hologram is not magnified, so $m = 1$. The resulting magnification of the holographic real image is estimated as follows: According to [Mei65], the lateral magnification $M_{lat,R}$ is approximated by

$$M_{lat,R} = \frac{m}{1 - m^2 z_o / \mu z_c - z_o / z_r} \quad (2.36)$$

for the paraxial case derived from the imaging equations 2.34 and 2.35.

The longitudinal magnification $M_{long,R}$ differs from the lateral magnification and can be expressed by

$$|M_{long,R}| = \frac{1}{\mu} M_{lat,R}^2. \quad (2.37)$$

In the setup presented here, the parameters $\mu = 1.01$, $m = 1$, $z_o = 0.6m$, $z_r = z_c = 12m$ are taken as standard. Fig. 2.6 shows the amount of lateral and longitudinal scaling by the wavelength shift. It is less than 1 %. Isotropic scaling can only be achieved for a fixed image position of z_i . The reconstruction parameter z_r has to be changed for this purpose. It has been found experimentally, that image aberrations introduced by a scaling below 5 % already disturb the reconstruction. As the scaling is not isotropic, it is preferable to adjust the involved wavelengths and the optical set-up for aberration minimization.

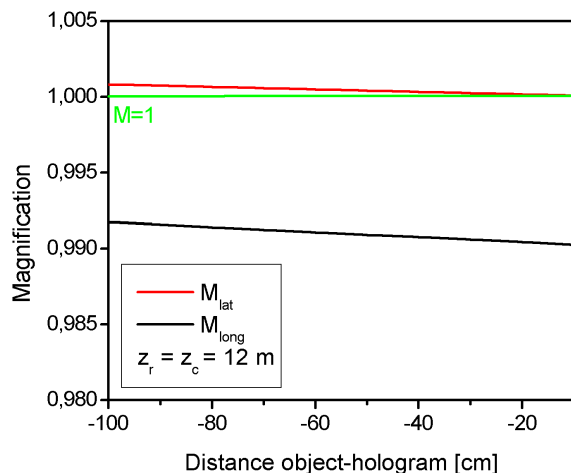


Figure 2.6: The lateral magnification $M_{lat,R}$ and the longitudinal magnification $M_{long,R}$ of the reconstructed real image are calculated and depicted against the distance of the object to the hologram plane (see Fig. 2.5). The reference beam and the reconstruction beam are assumed at equal distance to the hologram (12 m).

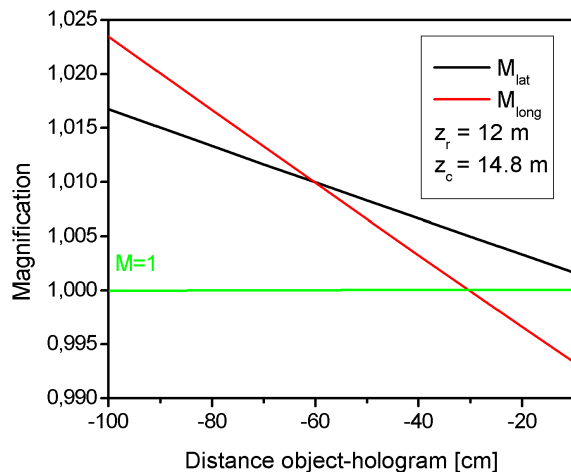


Figure 2.7: The reconstruction beam distance is adjusted to achieve isotropic scaling at the object distance of 60 cm.

2.4 Summary

Up to this point, the previous sections have given a summary of the theory of holographic imaging: While volume holograms are used as display holograms, which can be read out with spectrally broad light sources, the holograms recorded for facial imaging can be considered as plane holograms. Off-axis geometry is used for the separation of the diffraction orders of the holographic image. Based on the intensity distribution in the hologram plane,

it is shown that the real image reconstruction of the object wave occurs, if the hologram is read out with the phase conjugate reference wave. High diffraction efficiency of the hologram is crucial for a high image contrast in the holographic reconstruction, which justifies the use of phase holograms, even though amplitude holograms have some practical advantages. The superior resolution of an analogue recording material makes it feasible for the recording of large scenes in off-axis geometry. While portrait holography requires single frequency pulsed lasers, the hologram read-out may be accomplished by a continuous-wave laser of low temporal coherence. This lowers the image resolution, but also reduces speckle noise in the optical reconstruction. To quantify image aberrations, the concept of wavefront matching is presented. It yields the insight that holographic aberrations can be described in the same manner as lens aberrations. The phase front of the reconstruction beam has to be adjusted to the recording geometry for an aberration free reconstruction. Furthermore the skewness of the hologram plate is a decisive parameter to compensate for hologram aberrations. A wavelength shift between the reference and the recording beam leads to aberrations and a small amount of unisotropic scaling of the real image.

Based on the above concepts, a two step system is realized for holographic facial measurement. A pulsed laser system is utilized to record portrait holograms, and a second optical set-up, containing a scanner unit, is used for optical read-out and digitization of the real holographic image.

Experimental issues are addressed in the following chapter. Digital image processing for the extraction of surface information from the holographic image is then presented in chapter 4.

Chapter 3

Experimental implementation of holographic facial measurement

A hologram stores phase and amplitude information of a light wave scattered by an object - the object wave. The reconstruction of the object wave phase front from a hologram yields a three-dimensional image of the object wave. Efforts to extract the depth information of an object from the hologram to use it for shape measurement include various experimental techniques for image contouring [HH65], [HH66], [MR75], [Abr76b], [Abr76a], [HO84], as well as concepts to use the depth of focus information in the real holographic image for metrology applications [Ste68], [ART73], [TW63], [Gat86]. But only in combination with modern digital image processing, a shape-from-focus technique has been realized successfully for shape measurement of living human faces [Bon02]. Recent developments are reported on the implementation of surface detection for small and microscopic objects from numerical real image reconstructions of digital holograms [CKWvB04], [CMD99], [MWLJ04]. Due to the limited size and resolution of digital sensors, a high resolution large-scene application as the presented facial measurement system is based on analogue recordings with subsequent optical read-out and digitization (see section 2.1.3).

The real image is a body of light that can be visualized by inserting a scattering screen. Such projection imaging is used to digitize the real image. The resulting digital data is treated numerically to extract a surface model. The numerical procedure is presented separately in the following chapter, while in the current chapter the following experimental steps are presented:

- *Hologram recording* The holographic camera is introduced in section 3.1. It is optimized for living human face measurement (although adjustable for the recording of objects of different sizes and materials), with regard to the wavelength, the laser intensity and the arrangement of the recording beams. Furthermore, as explained in the preceding chapter, living human face measurement requires a pulsed laser sys-

tem of high spatial and temporal coherence. The laser system and the recording procedure will be presented.

- *Eye-safety* For medical facial imaging in a hospital environment, eye-safety of the recording system is a decisive requirement. The recognizability of patients increases for recordings with open eyes. The handling of the system is of course easier as protecting eye patches can be omitted. In former work an intensity modulated object illumination beam was needed to enhance the contrast on the facial surface. Using such illumination of the face the recordings were not eye-safe [Gie03]. It is now possible to use portrait holograms with homogeneous object illumination. Thus diffusor plates can be used in the object illumination beam which is the key for eye-safe recordings. Section 3.2 refers to this issue.
- *Mirror images* For an extended field of view, several mirror arrangements can be added to the holographic camera. Mirror images are used to record a frontal view of a lying object and to image side views of a sitting person. This has already been mentioned in [Gie03], but now for the first time it is possible to gain computer models of side views of a sitting person which is relevant for the task of medical facial imaging. Furthermore a set-up for recordings of panoramic images is introduced. The subject of mirror images is described in section 3.3.
- *Chemical processing* Optical recording parameters and chemical processing of the hologram have to be optimized for a high fringe visibility of the interference pattern on the hologram to achieve a good diffraction efficiency and sufficient image contrast in the real image (see section 2.2.2 and 2.1.7). The photographic material and processing parameters are given in section 3.4. A new development concerns hologram processing. It is automated using an x-ray film development machine.
- *Hologram read-out* The hologram information is read out optically. The phase conjugate reference wave illuminates the hologram, and a one-to-one copy of the object wave is replayed in the original relative position to the hologram plate. The alignment of the hologram determines the resolution of the replayed image. In contrast to former work, the presented set-up allows to compensate for image aberrations which is crucial for projection imaging of skin pores. The tilt of the incident read-out beam, in the vertical axis as well as in the horizontal axis, is the decisive parameter for high resolution in the replayed image (see section 2.3). An adjustable hologram holder is found to be an adequate tool to account for the high positioning accuracy of large aperture holographic imaging. A flexible scan axis is introduced to access a large viewing angle and mirror images for projection imaging in the real image.

- *Digital projection imaging* The real image of a face comprises an image volume of approximately $(30 \times 30 \times 30)$ cm³. This image volume is quantized in a digitization step. In this step, image noise has to be minimized. Otherwise the contrast in the real image formed by skin pores of the facial surface can not be distinguished from noise contributions. In earlier work [Gie03], [Bon02], [The03] a digitization arrangement using a diffusing screen was used. This screen introduces disturbing image features due to the roughness and the scattering characteristics of the diffusor. A CMOS line scanner is now used in this work to record projections of the real image. The scanner is moved on a PC controlled translation stage to capture the image volume. Noise and image contributions can be separated to a comparatively large extent in this arrangement. The digitization unit is discussed in section 3.6.
- *Reference beam reconstruction* Finally, first experimental results are presented and discussed, that make use of a reversed imaging scheme. It uses the reconstruction of the reference beam caused by the illumination of the hologram with an elementary part of the object beam for surface detection. This section is not based on the experimental issues given above, but is rather a complementary aspect, and therefore added to this chapter in section 3.7.

3.1 Holographic camera

The holographic camera is sold and manufactured by GEOLA (www.geola.com). The model in use is labeled GP-2J. The holographic camera essentially comprises a pulsed laser with parameters that are optimized for portrait recordings. Therefore, a green wavelength (526.5 nm) is chosen with high reflectivity on skin for a small penetration depth. The pulse duration of 35 ns determines the exposure time, which is short enough to record living human faces and moving objects without movement artifacts, and at the same time, the pulsed laser operation greatly reduces the stability requirements on the recording set-up and environment, even allowing for mobile holography (see section 3.1.2). The pulse energy of the illuminating laser is sufficient to record an image volume of several cubic meters, and to image and reconstruct objects of comparatively low reflectivity, as for instance, skulls and mummies (see chapter 5).

Figure 3.1 shows a photo of the holographic camera on the right, and a schematic view of the reference beam path in the left part of the figure. The camera housing comprises the pulsed laser system. To construct the off-axis holography geometry the laser beam is split in three parts inside the camera housing (see below for details). A smaller fraction (10-25 %) of the laser beam serves as reference beam. Two beams are to illuminate the object from two sides. The object illumination beam is widened by concave lenses inside the laser

housing and by diffusor plates at the laser ports. The diffusor plates play a central role concerning eye-safety of the recordings (see section 3.2). The diffuse illumination beam still fulfills the demands for coherence in the hologram plane, because the light wave that illuminates the diffusor plate is coherent across the spot on the diffusor and the path length differences from the laser source to the hologram via the diffusor plates are covered by the temporal coherence of the laser. The stability requirements account for the diffusor as well as for the object, and are uncritical for ultra-short exposure times [Gie03].

Recording procedure To record a hologram, a hologram plate of the standard size (30×40) cm² is put in the holder in front of the camera housing. A person may sit in front of the camera facing the hologram plate. The photo in Fig. 3.1 shows the front of the camera and the chair. The positioning of the person in front of the camera is uncritical. There are no lenses between the face of the person and the hologram plate, so no image sharpness has to be adjusted. The laser pulse energy and the coherence length determine the accessible volume in front of the camera and include several cubic meters. Pressing a button on the electronic rack of the camera activates a repeating acoustic signal announcing the laser action. A second push on the button initiates the laser pulse. The hologram is ready for chemical processing, and the recorded person can leave. The recording procedure takes place under red light conditions. This is changed by introducing a shutter in the latest generation of holographic cameras (see section 3.1.2).

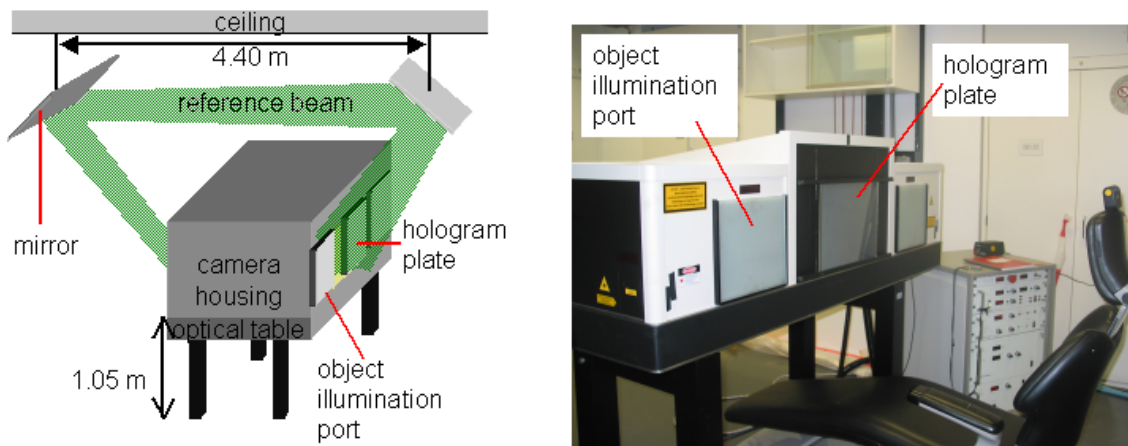


Figure 3.1: The holographic camera is sketched in the left image: The divergent reference beam is sent over two mirrors mounted on the ceiling. The angle of incidence to the hologram plate is chosen as the Brewster angle to minimize reflections from the glass substrate of the hologram plate. The right image shows a photo of the holographic camera.

3.1.1 Single-frequency pulsed laser system

As described in [Bon02], the stability demands for portrait holography can only be met by using a pulsed laser. The recording of the face including mirror images requires a recording volume in the range of a cubic meter. This determines the necessary temporal coherence of the laser. On the other hand, the pulse energy has to be adapted to the sensitivity of the photo material. The material used here is a high resolution silver halide emulsion which has to be exposed at $35 \mu\text{J}/\text{cm}^2$. Assuming a hologram size of $(30 \times 40)\text{cm}^2$ this corresponds to a pulse energy of 42 mJ impinging on the plate. The light used for object illumination is commonly chosen approximately ten times higher than the reference wave to account for absorption and scattering losses. Taking into account losses of the pulse energy at the diffusor plates and other optical components a pulse energy of at approximately 1 Joule should be provided for the recording. To achieve this energy but also maintain a proper mode selection for single frequency operation, the laser system is designed in a master-amplifier set-up. It comprises a laser oscillator as master with subsequent amplification and second harmonic generation. The master oscillator works with a flash lamp pumped Nd:YLF crystal and uses a saturable absorber as passive Q-switch in a ring oscillator (see Fig. 3.2). Two etalons narrow the bandwidth of the radiation. A dove prism is used to reach a uniform transversal intensity distribution, and a Faraday rotator combined with a $\lambda/2$ wave plate causes unidirectional oscillation. Temporal and spatial coherence, polarization and pulse duration are set by this master oscillator set-up.

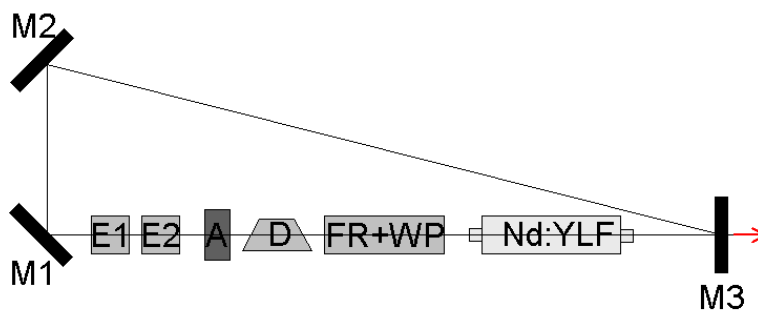


Figure 3.2: The master oscillator is a ring oscillator designed for careful mode selection to provide the coherence length that is needed to record macroscopic objects in the holography set-up. M1, M2, M3: mirrors; E1, E2: etalons; A: passive Q-switch (saturable absorber); FR: Faraday rotator, WP: $\lambda/2$ wave plate; D: Dove prism; Nd:YLF: laser crystal pump chamber.

The pulse is amplified in a Nd:Glass rod which is pumped by a high voltage flash lamp (see Fig.3.3). The laser pulse passes the rod twice. After the first pass the wave front is disturbed by effects of diffraction and aberration. A phase conjugating mirror is positioned behind the rod and reflects the laser pulse back. The phase front is inverted by

the reflection process (stimulated Brillouin scattering) and the disturbances are to a great extent reversed during the second pass through the rod. Finally the laser pulse is sent through a KDP crystal for second harmonic generation.

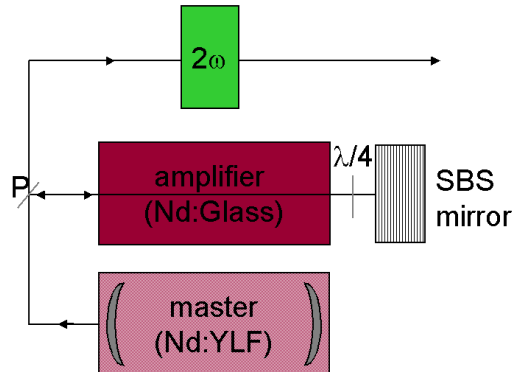


Figure 3.3: To achieve high energy output at single frequency operation of the laser, the pulse generation is separated in two parts: First, the required coherence properties of the pulse are set in the master oscillator. In second step, the pulse is amplified in a synchronized second stage. To reverse wave front distortions, a phase conjugating mirror based on stimulated Brillouin scattering inverts the wave front between the first and the second amplifier pass. P: Polarizer; $\lambda/4$: Quarter wave plate; 2ω : KDP crystal for second harmonic generation.

The laser pulse energy is adjusted by setting the amplifier flash lamp voltage and has a maximum energy of 2 Joule at 526.5 nm wavelength and 35 ns pulse duration (FWHM) [Bon02]. The coherence length is specified as $>3\text{m}$. The laser pulse is split into three beams, as shown in Fig. 3.4, to provide a reference beam and two object illumination beams. The object illumination beams are expanded by concave lenses and pass diffusor plates at the laser port.

3.1.2 Mobile holography

A new mobile system has been designed in cooperation with the company Geola Technologies Ltd. The main characteristics of this camera are that the whole system is set up within 20 minutes and fits into the load area of a car. Moreover, it works at any ambient light condition.

In contrast, the immobile laboratory set-up works at red room light. A shutter is mounted at the mobile camera to make daylight recordings. The high resolution of the recording material is connected with a low sensitivity of the holographic film. Illumination with room light of several seconds does not disturb the recording. It is even used as latensification to enhance the image on the hologram plate in some cases. Consequently, the shutter does not have to be as fast as the laser pulse.

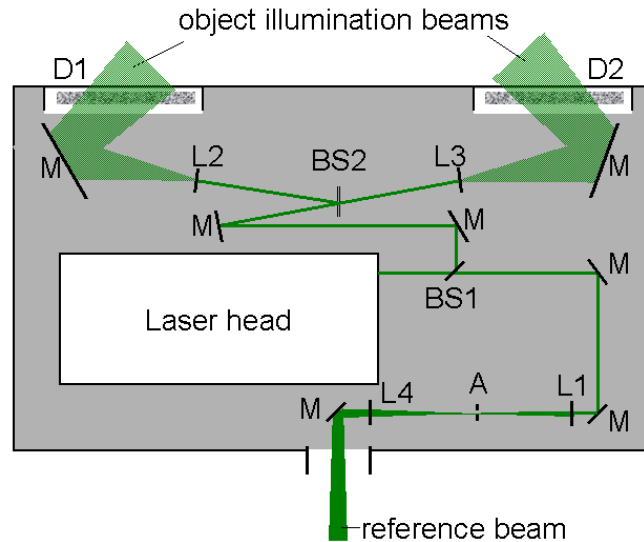


Figure 3.4: The laser pulse is split into three beams by the beam splitters BS1 and BS2. One beam serves as reference wave, the other two are used to illuminate the object. The reference wave is focused by the lens L1 and spatially filtered by the aperture A. The lens L4 is a spherical concave lens. The laser beam is divergent as it leaves the camera housing. The object illumination beams are expanded by concave lenses (L2 and L3) and sent through diffusor plates (D1 and D2).

Furthermore, the laser within the mobile camera operates at the wavelength 532nm instead of 526.5nm as the immobile system. The wavelength of the mobile system then matches precisely the read-out wavelength used in the optical reconstruction unit (see section 3.5).

A mobile camera system is now located at University Hospital Basel (see section 5.1).

3.2 Eye-safe recording of portrait holograms

When exposing the face to laser radiation, certain exposure limits for the skin and the eyes have to be met to avoid radiation damage. The exposure limits for eye-safe recordings are stricter than the exposure limits for skin, so in the following, the discussion is restricted to eye-safety. Basic issues on eye-safe recordings of portrait holograms using pulsed lasers are presented, for instance, in [Ans70]. The cornea of the eye is exposed to pulsed laser radiation, which is focused on the retina. This increases the energy density by more than five orders of magnitude, provided aberration free focusing of the eye. The final energy density in the focus on the retina depends on the wavelength, the eye geometry (in particular the aperture size given by the pupil diameter) and the energy density of the source that is imaged on the retina.

Laser light scattered by a diffusor is treated like an extended light source. The source

size corresponds to the spot size of the laser on the diffusor plate. To provide eye-safe recordings, the eye geometry and the focusing properties are given under worst case conditions, and the spot size of the laser source on the diffusor plate is enlarged by lenses to reduce the intensity of the focused image on the retina.

The source size for a given distance of the viewer is then expressed as angular extent of the source denoted α . If α is smaller than $\alpha_{min} = 1.5$ mrad, the exposure limit of the cornea for laser radiation between 400 and 550 nm and a pulse duration from 10^{-9} to 10^{-7} seconds is given by [dFuE], [oNIRP00]

$$EL = 5\text{mJ}/\text{m}^2. \quad (3.1)$$

If α exceeds the angle $\alpha_{min} = 1.5$ mrad, the exposure limit increases. If the source size is further increased and α exceeds $\alpha_{max} = 100$ mrad, EL is modified by a correction factor C_E , that varies in the different safety guidelines:

$$EL = C_E * 5\text{mJ}/\text{m}^2, \quad (3.2)$$

according to [dFuE], C_E is given as

$$C_E = \begin{cases} 1 & \text{if } \alpha \leq \alpha_{min} \\ \alpha/\alpha_{min} & \text{if } \alpha_{min} \leq \alpha \leq \alpha_{max} \\ \alpha_{max}/\alpha_{min} & \text{if } \alpha > \alpha_{max} \end{cases}$$

whereas in [oNIRP00] C_E becomes

$$C_E = \begin{cases} 1 & \text{if } \alpha \leq \alpha_{min} \\ \alpha/\alpha_{min} & \text{if } \alpha_{min} \leq \alpha \leq \alpha_{max} \\ \alpha^2/(\alpha_{min} * \alpha_{max}) & \text{if } \alpha > \alpha_{max} \end{cases}$$

The angular extent α of the source is measured from the viewer's eye. Fig. 3.5 shows the recording geometry that determines the size of the viewing angle for the holographic camera: The recorded person is positioned in front of the holographic plate at a distance of at least 60 cm, corresponding to a distance from the diffusor plates of 80 cm. A varying spot size on the diffusor plates (D1 and D2) by changing the positions of the lenses L1 and L2 changes the angular extent of the spot size from the viewer's position and allows to adjust the exposure to the given limits.

For the given dimensions, the exposure limit according to 3.2 is related to the diameter of the spot on the diffusor plate as shown in Fig. 3.6. For an angular extent of the source smaller than α_{min} , the exposure limit at the cornea is $500 \text{ nJ}/\text{cm}^2$. The reference beam which is not sent through diffusor plates is not eye-safe and has to be arranged carefully

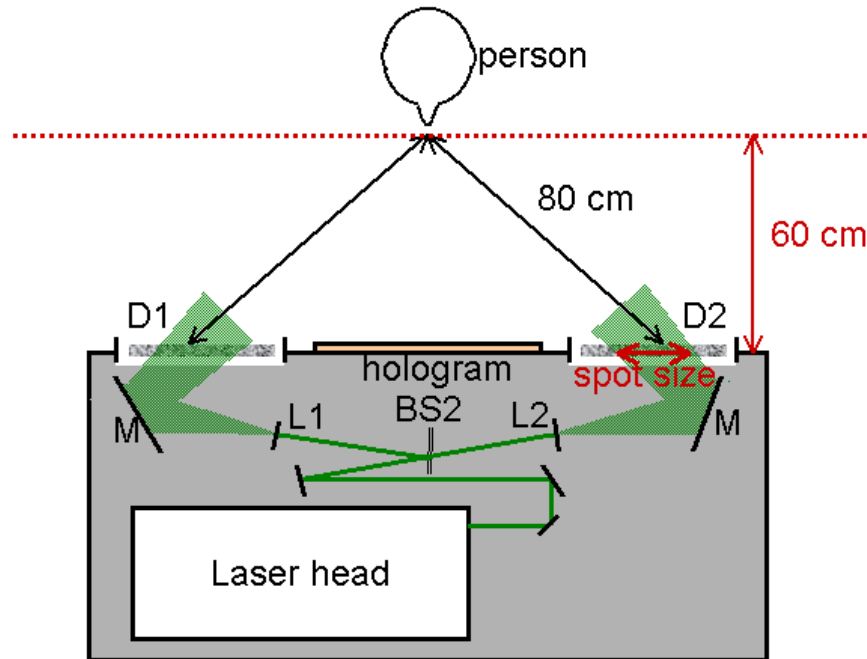


Figure 3.5: To make eye-safe recordings, the source size of the object illumination beam is enlarged: This is done by expanding the illumination beam by lenses (L1 and L2) inside the camera housing (gray field). The widened laser beams are sent through diffuser plates. The spot size on the diffuser plates and the distance of a person facing the plates defines the angular extent α of the source. By enlarging the source size, the energy density of the image of the source on the retina is lowered.

not to hit the recorded face directly or from reflections. The exposure limit rises up to $33 \mu\text{J}/\text{cm}^2$ at a spot diameter of $\approx 8 \text{ cm}$. For a larger spot size, the exposure limit remains constant [dFuE] or increases quadratically with α [oNIRP00].

These values for the exposure limit hold for the presumption of *perfect diffuser plates* at the object illumination port, so the area which is illuminated by the laser beam can be considered as source size. Perfectly diffusing materials destroy any correlation between the directions of the incident and the reflected or transmitted beams. To fulfill this condition, diffuser plates are used that are sand blasted from two sides.

3.3 Mirror images

The holographic camera is optimized for portrait holography. This implies that the set-up is designed to record the frontal view of a sitting person who faces the hologram plate. In some applications additional views recorded by mirrors help to provide the complete surface information that is needed. Three arrangements are presented in the following for the recording of lying objects, side views and panoramic images.

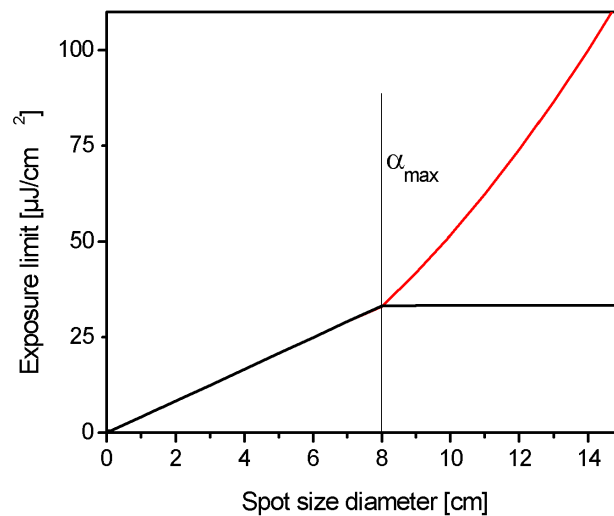


Figure 3.6: The increase of the exposure limit with growing spot size on the diffusor plates is shown for a viewing distance of 80 cm for the guidelines [oNIRP00] (red curve) and [dFuE] (black curve).

3.3.1 Lying objects

One application that the holographic imaging system is used for is the imaging of archaeological objects, like mummies (or bog bodies), for instance. Some of these objects can only be recorded in a lying position. The camera is then equipped with an additional mirror at a 45 degree angle above the lying object to yield a frontal view. This technique can of course also be used to image a lying person. The additional mirror is arranged above the object or person. This is depicted in Fig. 3.7. The size of the mirror varies. The mirror can be held by an assisting person due to the short recording time that prevents movement artifacts or, to image larger objects, a mirror is mounted in a fixed position.

The additional mirror causes the object illumination light to reach the object side which is turned away from the camera. This arrangement has been used to image various archaeological objects, at first the bog body of Husbäke [Nat02], [Sci02], [FBG+03].

3.3.2 Side views

Shading appears if a curved object surface is recorded. This is illustrated in Fig. 3.8, part (a). Depending on the shape of the recorded object, the object surface might in some parts be well illuminated by one of the laser ports but only a fraction of the scattered object light reaches the hologram plate. This lowers the resolution and the contrast for these image parts as it has the influence of a lowered imaging aperture (see section 2.1). Additionally, lower scan resolution in the real image appears: The imaging procedure includes digital

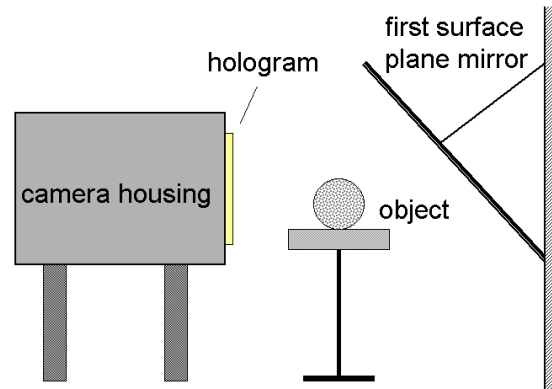


Figure 3.7: Recording geometry for lying objects: A mirror is mounted above the object to image a frontal view.

recording of projections of the real image. This will be explained in section 3.6. The angle between these projections and the recorded surface determines the effective scan resolution. This situation is depicted in Fig. 3.8 reduced to the (xz) -plane. A lateral pixel resolution Δx used for the scan of a surface with a skewness $\Delta x/\Delta z$ (assumed as linear over the pixel extent) corresponds to an effective resolution of approximately $\Delta x_{eff} \approx \sqrt{\Delta x^2 + \Delta z^2}$. This lowered resolution can be compensated by a higher scan resolution, but in some cases, it is more useful and easier to record the side view of a face in a mirror image.

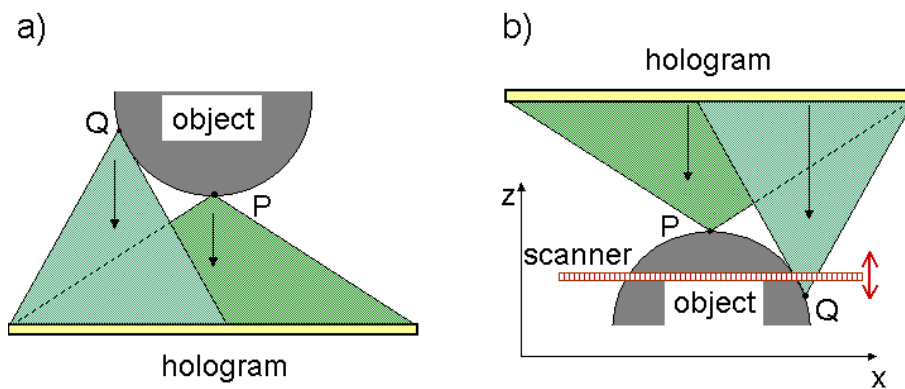


Figure 3.8: (a) The recording of a frontal view of an object with a curved convex shape is shaded if the normal of the recorded surface does not point on the hologram. (b) Digital projection imaging leads to a lowered scan resolution for surface parts that are oriented skew to the detector array. (The object illumination beam is not shown.)

Some objects or faces might also have a form that has undercuts if only a frontal view is recorded. Then, a recording with mirror views is necessary to image all relevant parts of the surface. The mirror image arrangement has the advantage that the different views

of the face are recorded simultaneously in the same hologram, and movement artifacts as known from subsequent recordings are prevented.

To provide full information of a face from one ear to the other, side views of the face are recorded using two mirrors arranged as shown in Fig. 3.9. A photo taken from the virtual image of the resulting hologram is shown in Fig. 3.10. The reconstruction of these images is accomplished by adjusting the scan axis for each object view. The images are captured and processed separately (see below). Commercial surface registration software can be employed to match the views and create a composite surface model.

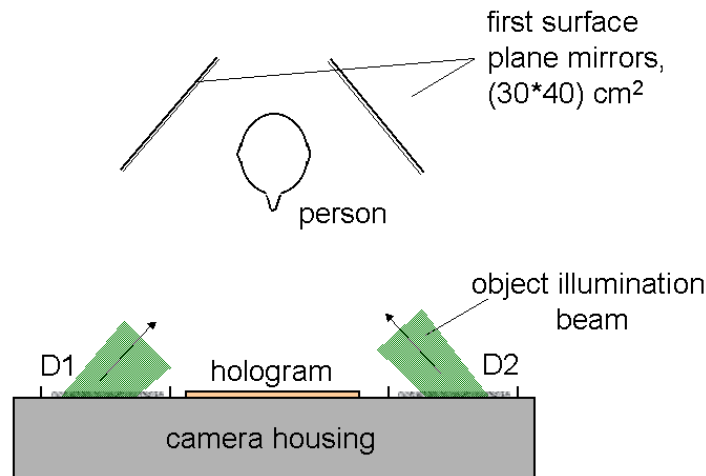


Figure 3.9: Two mirrors are arranged beside the recorded person to image the side views of the face.

3.3.3 Panoramic imaging

The mirror arrangement can be extended to provide a full 360° image of an object in a single hologram. To this aim, the backside of the object has to be illuminated by a third mirror (see Fig. 3.11). Two mirrors to both sides of the object are positioned to image the surface.

3.4 Hologram processing

As mentioned in section 2.1, the superior resolution of analogue recording materials compared to digital sensors makes them suitable for the recording of macroscopic objects at μm resolution over a large angular extent using off-axis geometry. The hologram material used with the holographic camera is called VRP-M and consists of fine grains of silver

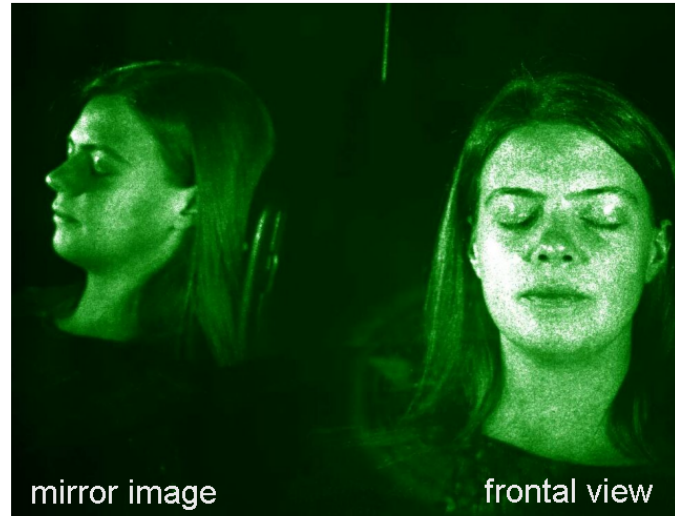


Figure 3.10: Photo of the virtual image of a hologram, showing a frontal view and a side view of the recorded facial surface.

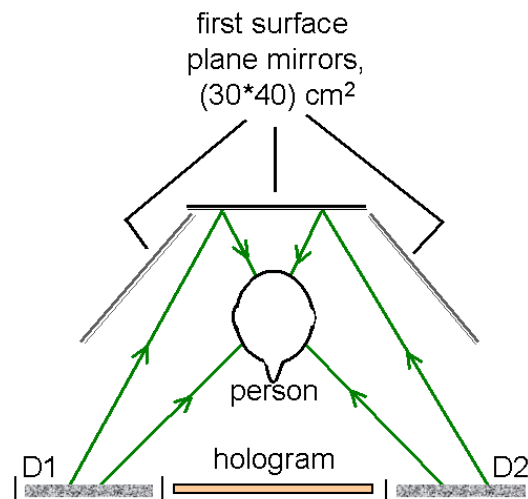


Figure 3.11: Mirror set-up for a panoramic recording: The images of the side mirrors are used to record the surface. The third mirror serves for the illumination of the back side of the object.

halide compounds dispersed in gelatine. According to the specifications given by the saling company (Slavich, www.slavich.com) the grain size distribution of the material is centered around 40 nm. The optical density changes approximately linearly with the illuminating energy density between 20 and 40 $\mu\text{J}/\text{cm}^2$ for pulsed illumination. These values determine the pulse energy and the reference beam ratio of the laser for hologram recordings of high diffraction efficiency. The reference beam energy density is used to reach the lower edge of the characteristic curve of the photographic material, while the object beam modulates the

signal by interference in the linear dynamical range. A latensification step is recommended and the hologram is illuminated with diffuse light after the recording for 2-10 seconds. This step stabilizes and enhances the image on the hologram, but at the same time, the haze of the film material is enhanced and appears as noise. Therefore, the latensification step is avoided to minimize image noise in the reconstructions.

The hologram recorded on VRP-M fine grain emulsion is processed chemically by two basic steps: First, the hologram is developed, then follows either bleaching (phase holograms) or fixation (absorption holograms). The chemical processing steps have been described for phase holograms in former work [Bon02] and follow the recommendations of the provider which are based on scientific work in this field [Bje95]: SM-6 is used for developing, and PBU-Amidol for the bleaching step.

3.4.1 Automated system

The chemical procedure described so far is performed by bathing the exposed hologram plate in plastic basins. The baths for the different processing steps are changed manually. A more convenient solution has been developed by using an x-ray film development machine. For automated development, it is advantageous to use photo chemistry of long storage life time for a small amount of maintenance. Photo chemistry for hologram fixation is commercially available and can be stored in a reservoir for several months. For this reason, automated hologram development is implemented for absorption holograms. While phase holograms and absorption holograms are recorded using similar laser parameters, they differ in their processing during and after the development of the hologram: The necessary optical density that is reached by developing the film is lower for absorption holograms, otherwise their diffraction efficiency decreases. A slower, modified developer was used to find the right processing parameters for amplitude holograms. The fixation is accomplished by using commercial photo chemistry (Superfix Plus by Tetenal). The processing steps and results are summarized in [Lad04] and [LFT⁺04]. In the x-ray film development machine the hologram is transported through the processing baths by rolls inside the machine which requires that the hologram is recorded on flexible material, hence a film substrate is used for the holograms instead of a glass plate. The film substrate is fixed plane to a glass plate with a suction groove which is connected to a vacuum pump. This system is developed to provide automated processing in a hospital environment (see chapter 5). The results shown in this work are gained from holograms that were processed manually.

3.5 Optical hologram read-out

A continuous wave laser (Coherent Verdi V2) is used as light source in the reconstruction unit. The laser operates at the central wavelength of 532 nm with a spectral width <5 MHz. The laser power is adjustable up to 2 Watt. As pointed out in section 2.1, the reconstruction of the real image is accomplished by illumination of the hologram with the phase conjugate reference wave. In the recording set-up, a divergent wave illuminates the hologram as reference wave. To generate the phase conjugate convergent wave large enough in diameter to light the hologram in its full extent ((30×40) cm² is the standard size), the laser beam is first expanded and then focused with a spherical mirror. The set-up is sketched in Fig. 3.12. The beam expansion is achieved by the telescope T and a concave lens (DL). By passing these elements, the beam is expanded to a diameter of approximately 50 cm as it impinges on the spherical mirror (SM). The beam is then sent over a periscope. Using this periscope, the beam impinges on the hologram in a geometry that corresponds to a 180 degree rotation of the recording set-up. Objects in the real image appear upside down.

A scanner is mounted on a translation stage, and the image volume is captured by moving the translation stage axially through the real image. The translation stage is not fixed to the optical table, but put on a profile with a swivel point at the hologram, so the translation direction of the stage can be adapted to match the axis of the reconstructed image. This set-up was chosen this way to include side views recorded by mirrors in the reconstruction unit (see section 3.3).

Aberrations due to astigmatism of the spherical mirror have to be compensated for. To this aim, the hologram holder is adjustable in the height of the hologram and the lateral position. The hologram can be rotated around the vertical and the horizontal axis as shown in Fig. 3.13 to optimize the hologram tilt in two axes for minimization of aberrations (see section 2.3).

3.5.1 Alignment

An accurate reconstruction of the real image can be aligned by the recording of rulers. First, a ruler is placed in front of the holographic camera skew to the hologram plate. The real image of the ruler is reconstructed optically. The lens DL in Fig. 3.12 is moved and the hologram skewness is adjusted to minimize aberrations. To observe the scaling of the real image as the lens is moved, the recorded ruler is used as projection plane of the real image, and a stretch or a shrink of the reconstructed image is visualized by a comparison of the marks on the original and the replayed ruler. Digital photographs of these projections are shown in Fig. 3.14, in part (a) with a lens position for accurate

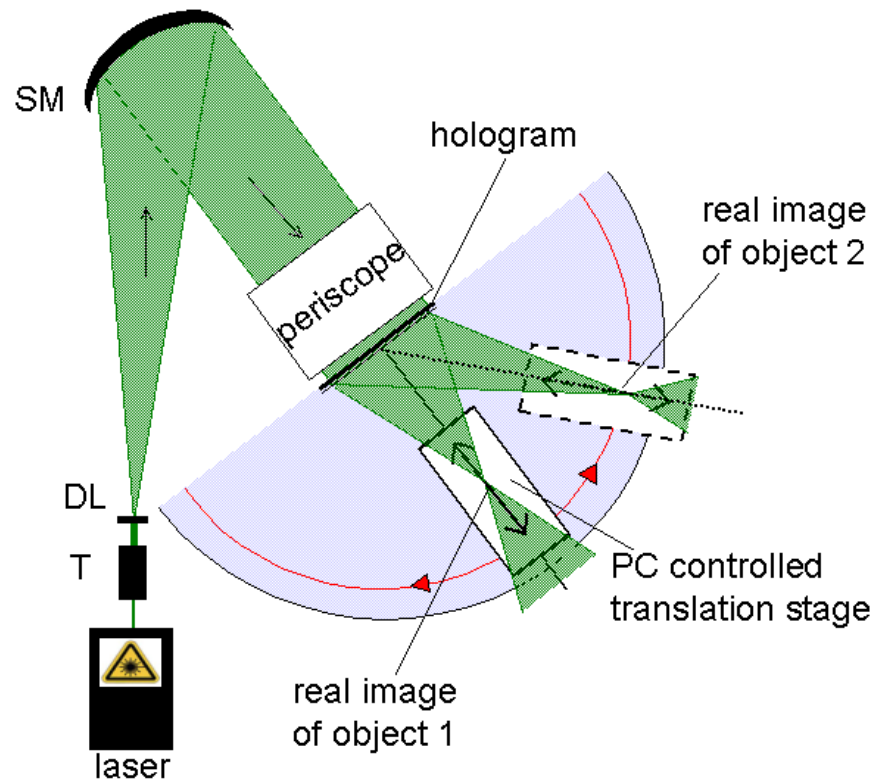


Figure 3.12: The hologram read-out is accomplished by illuminating the hologram with a convergent wave, generated by a telescope (T), a concave lens (DL) and a spherical mirror (SM). The real image appears upside down. Objects that are arranged horizontally are scanned separately. The scan direction is adapted to the respective axis by moving the scan arm as shown by the red arrows.

scaling of the reconstruction, and in (b) with a lens position yielding an enlarged image of the ruler. Nevertheless, it is not possible to scale the image arbitrarily without introducing severe image aberrations and even a slight misalignment reduces the image contrast for in-focus regions.

Minimum aberrations of the real image have been found for a 1-3 % magnification of the real image. If small aberrations can be tolerated, an accurate scaling can be achieved as shown in Fig. 3.14. Possible sources of the deviation are the wavelength shift of the lasers used for recording (526.5 nm) and reconstruction (532 nm) of the holograms and the optical components in the reconstruction unit. The latest generation of holographic cameras works with a Nd:YAG laser crystal and radiates laser light at 532 nm, so the influence of the wavelength shift will be removed. Further improvement of the optical components in the read-out unit can be expected by applying ray tracing methods for optimal wavefront reconstruction.

To show the effect of aberrations a Siemens star printed on paper is recorded on a hologram and reconstructed optically. Projections of the real image are scanned with a

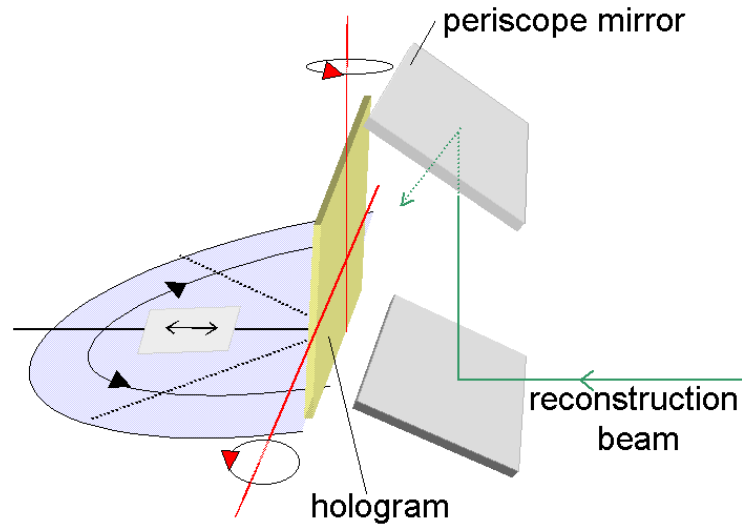


Figure 3.13: The hologram is illuminated from above by a periscope. The tilt of the hologram is adapted using a hologram holder that can be rotated in the vertical and the horizontal axis.

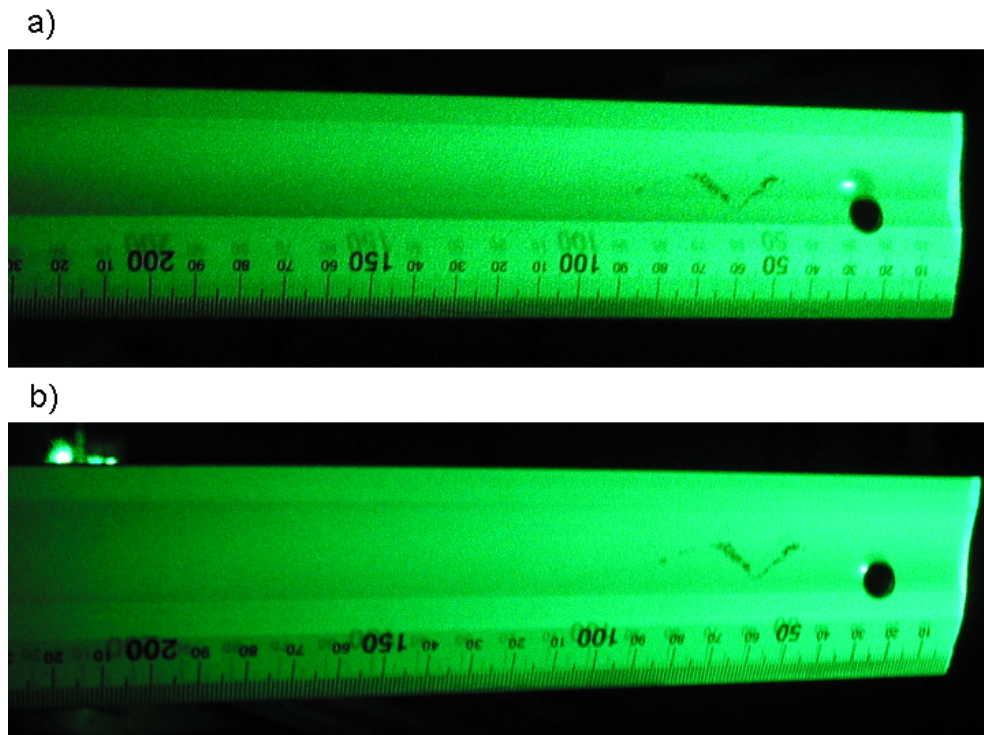


Figure 3.14: The real image of a ruler is projected on the original object (a) with accurate scaling, (b) with enlarged scaling by changing the divergence of the reconstruction beam. The scale on the ruler indicates millimeters.

flatbed scanner as described in section 3.6.

Fig. 3.15 shows examples of scanned projections: In the upper row, the skewness of the

reference beam is slightly misaligned, resulting in cylindrical aberration. Two line foci are observed at different focal planes, one line focus image is shown in part (a) of the figure. A perpendicular line focus appears at a distance of 6.3 mm (not shown) from the first line focus. Hence, the plane object is not reconstructed as such, but appears disrupted in the real image. Between these line foci, the image 3.15(b) is found as image of most even image contrast. Obviously, the central part of the Siemens star image is not resolved optically. For aligned skewness of the hologram, the images (c) and (d) are recorded instead: The image sharpness equally increases for all image parts as the focal plane is approached, and, as is illustrated in part (d), the image resolution is increased.

To evaluate the resulting image resolution of the scanned real image of the printed Siemens star, the real image scan is compared with a 600 dpi (*dots per inch*) document scan of the Siemens star. The average absolute value of the deviation of the average intensity of image points on circular sections around the center of the Siemens star is evaluated. This is shown in Fig. 3.16, for the real image scan as black curve and for the document scan as red curve. Additionally, an artificially blurred image is evaluated as well, and the result is shown as green curve. Obviously, an increase of the intensity deviation from the average sets in at a different radius for a blurred image than for a sharp image. The Siemens star has 72 segments, so an absolute resolution of $l = \pi d/72$ (d denotes the diameter) is related to the measured diameter.

For the document scan, a radius of 10 pixels is found as the point where the increase starts which corresponds to a resolution of $37 \mu\text{m}$. The respective radius for the scanned real image is slightly larger (13 pixels), which corresponds to a resolution of $48 \mu\text{m}$. The increase of the contrast measure for the blurred image sets in at a radius of 35 pixels, corresponding to a resolution of $129 \mu\text{m}$. The slightly lowered resolution of the scanned real image in comparison with the document scan may be explained by a positioning inaccuracy of the scanner in the real image for the scan.

3.6 Digital recording of image projections

The real holographic image is sliced into 2d projections by scanning the image along the z axis with a commercial flatbed document scanner. The real image provides a one-to-one copy of the object wave, with a lateral size of $\approx (20 \times 30)\text{cm}^2$ for a facial recording. In former experiments, a diffusing screen was utilized to visualize the real holographic image. The projections of the light field on the diffusor plate were imaged to a CCD (*Charge Coupled Device*) chip with a camera objective.

The scattering characteristic of the diffusor plate leads to a decrease of the image brightness with distance from the image center. This is demonstrated in Fig. 3.17. Part

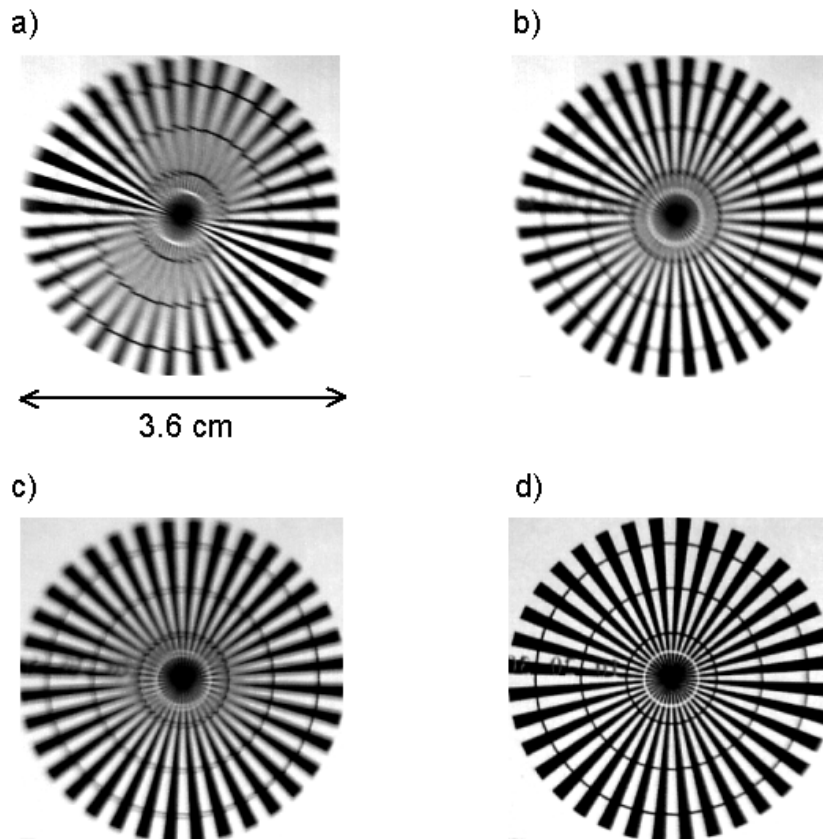


Figure 3.15: The holographic real image of a Siemens star is reconstructed and projections are scanned (see section 3.6) at two distances from the hologram. Part (a) shows a cylindrical aberration due to hologram misalignment. A line focus appears. The best image contrast for the whole image that can be achieved is shown in part (b). The lower row shows an out-of focus image (c) and an in focus image (d) with adjusted skewness of the hologram.

(a) shows an images recorded with a volume diffusor plate and (b) with a surface diffusor plate. To achieve an even light distribution, the volume diffusor plate is favorable, but image contrast and resolution are degraded for recordings with volume diffusor plates. On the other hand, high resolution and image contrast due to a fine surface structure (b) leads to a strong decrease of the image brightness in the outer image regions. Both aspects degrade the signal to noise ratio in the image detection. One possibility is optimization of the scattering surface, but scanning the light field directly without an intermediate diffusor plate has two advantages:

1. A direct scan without the camera objective makes the system work without scaling optics and consequently, a calibration step is not necessary.
2. The scattering surface of a diffusing screen is always a source of noise. Speckle noise and intensity fluctuations due the surface roughness of the screen are of similar size and structure as the skin structure of the face and therefore difficult to separate from

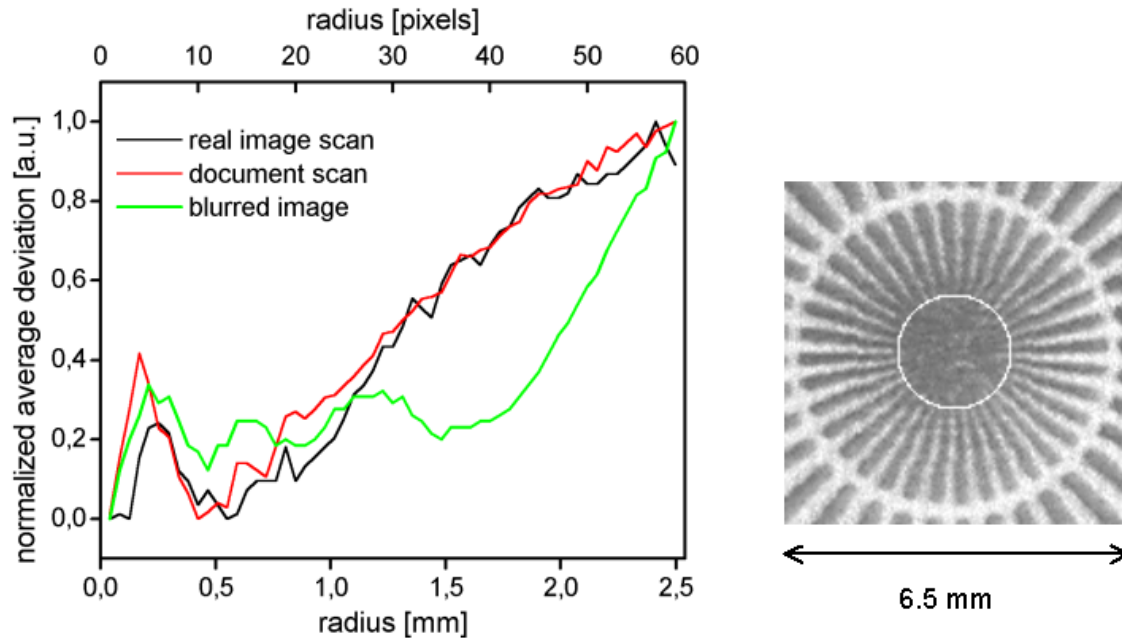


Figure 3.16: Deviation of the image values from the average on circular sections as function of the pixel radius of the circular sections through the scanned Siemens star image. The right image shows the central part of the reconstructed Siemens star image, and an exemplary circular section is inserted (white line).

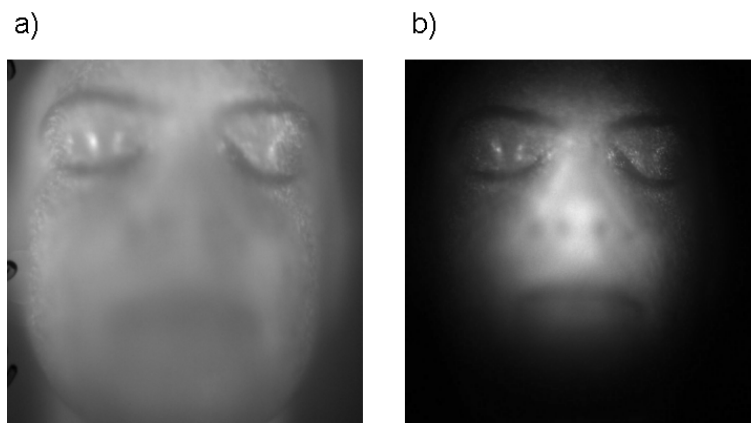


Figure 3.17: Part(a): Projection of the real image on a volume diffuser plate; (b) Projection of the real image on a surface diffuser plate. Both images have been recorded with a CCD camera. The image brightness has been adapted for a better visibility of the differing scattering properties of the diffusers.

the actual image signal.

A CMOS document scanner (CanoScan LiDE 50) is used to scan the real image. A GRIN (gradient index) lens array is part of the scanner to improve the fill factor of the CMOS structure. (CMOS stands for *Complementary Metal Oxide Semiconductor*, refer-

ring to the fabrication process, and not, as the term CCD, to the read-out procedure (see [Hup00], for instance.)

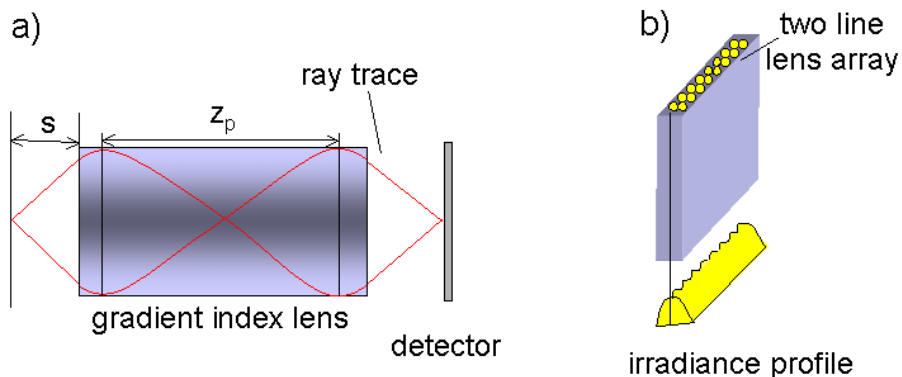


Figure 3.18: Part (a) shows a ray trace for a light source that is imaged by a focusing gradient index lens. The lens has a continuously decreasing refractive index with growing distance from the core. Continuous bending of the light inside the lens leads to a periodic field distribution along the propagation direction. The pitch length z_p of this distribution characterizes the steepness of the index change. Part (b) shows the periodic irradiance profile caused by a two line lens array (adapted from [Lam82]).

The influence of the lens array on raw data is considered. Stripe artifacts are observed when out-of-focus light impinges on the scanner surface. The lens array consists of a number of GRIN lenses (see Fig.3.18(a)), each forming an imaging aperture.

Overlapping these apertures causes an uneven irradiance profile, which is depicted in Fig.3.18(b) [Lam82], [MT80]. For a fixed object distance s the lens array irradiance profile can be corrected, the irradiance profile from other object distances differs and leads to periodic artifact in the scanned image.

Artifacts are demonstrated in Fig. 3.19: Scans of the real image of a cylindrical metal rod of 1.5 cm radius are shown. The images in the upper row are taken with the object in focus, the images in the lower row are taken at a different z -position behind the image focus. The left images are unfiltered data. To enhance the structure of the artifacts and also the object surface, a high pass filter is applied to the images, and the results are shown in the right column. (For details of the filter application, see section 4.2). In summary, concerning scanner artifacts, the following is observed:

1. Obviously, scan artifacts disappear for focused regions, and vary with the distance between the image focus and the scanner surface. The artifacts do not affect focal regions. The quality of the texture information is unaffected by these artifacts as it is taken from in-focus images.

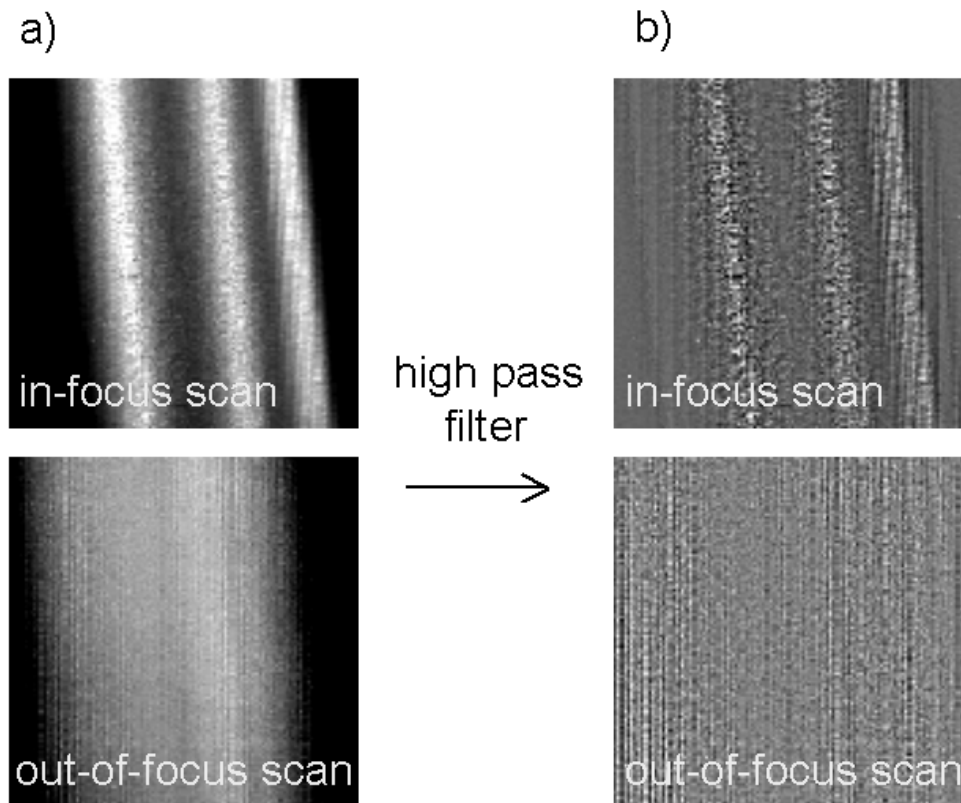


Figure 3.19: The upper left image shows a scan through the real image of a metal rod of 1.5 cm diameter. The front of the rod is in focus. For the recording of the lower image, the scanner was moved out of the focal plane. Applying a high pass filter to these images reveals a stripe structure for the out-of-focus light, but an undisturbed image part that is in focus.

2. The size and structure of the artifacts clearly differ from the surface structure that has to be detected for surface identification: The scan artifacts have a comparably low spatial frequency along the vertical axis. Vertical high pass filtering eliminates these stripes without reducing useful image information.

Translation stage The scanner is moved on a computer controlled linear positioning stage (PI M-531.DD, max. resolution $10 \mu\text{m}$) through the image volume. The captured images are transferred to a computer and stored on hard disk; these images are referred to as raw data. A typical data set consists of 256 images resp. slices. Each image records an area of $(20 \times 30) \text{ cm}^2$. These slices are then treated numerically to extract contours by identifying focused image points, which will be treated in chapter 4.

The scanned image volume coordinates are not fixed with regard to the hologram: The z -axis is determined by the position of the profile that the scanner is fixed to. The (x,y) plane is the scan area (see Fig. 3.20).

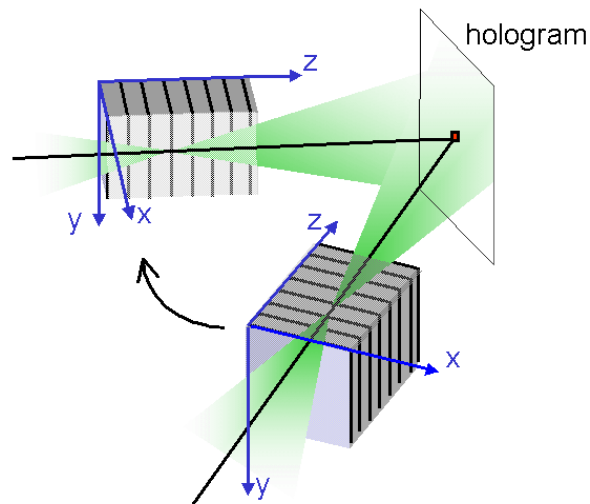


Figure 3.20: Raw data used for numerical data processing comprises a scanned image volume with coordinates as shown in this figure: The z coordinate is determined by the profile position, the (x,y) plane corresponds to the scanner area.

Up to this point, optical read-out of the hologram by real-image reconstruction and the digitization unit of the image volume have been described. The next step for surface measurement is digital image processing for focus detection in the real image. Three-dimensional location of foci in the real image allows to reconstruct the shape of the recorded object. This will be treated in chapter 4.

Before this, a complementary imaging scheme is discussed, which is not based on the reconstruction of the real image, but relies on the reconstruction of the reference beam, as the object beam (partially) impinges onto the hologram plate.

3.7 Surface identification by reference beam detection

The imaging concept introduced in the above sections is based on optical image reconstruction by illumination of the hologram with the phase conjugate reference beam. The resulting real image is digitally recorded by means of a detector array scanning the image volume of the object. The above method is the most obvious and convincing one, however certain difficulties are inherent in this process. Firstly, a large detector is needed with sufficient image resolution, covering an area of (20×30) cm² for facial recordings. This is not trivial with regard to desirable high image quality. Consequently it seems worth consideration how an alternative read-out process can be implemented that relies on reference beam reconstruction instead.

Reference beam reconstructions are used in optical information processing and pattern recognition [GKB⁺00], [LGC⁺04]. The basic holographic concept in this context is the recording of a number of thick holograms in a holographic medium with changing reference beam angles. Bragg diffraction leads to a selective read-out of the multiplexed volume holograms. The role of reference and object beam are reversed. The hologram is illuminated with one of the object beams. The measured reference beam intensities are determined by the correlation of the respective original object beam and the current object signal impinging onto the hologram. For a simple interpretation of the reconstructed reference beam intensity a 4f set-up ([GKB⁺00], [Lug64]) yields a reference beam intensity which is proportional to the correlation of the original object beam stored in the hologram and a second object beam, present at some later time emerging from the same image plane.

An imaging scheme using optical correlation has also been proposed for surface detection [SB03]: A volume hologram of two planar beams is recorded. One of them is impinging under a certain angle and is used as reference beam. The amount of diffracted light of a beam impinging on this hologram is depth selective: The maximum diffraction is achieved if the divergence of the impinging beam matches the divergence of the recording beam. Moving and imaging an object in front of the hologram and observation of the intensity of the diffracted light can thus be used for surface detection. Of course this includes a scanning step, which has to be avoided for surface surveying of living human faces. Thus, another option to use the reference signal for focus detection is discussed: The object is recorded on a hologram and removed afterwards. A focusing lens is positioned in front of the hologram instead. If the point source coincides with a surface point of the original object, a part of the diffracted light is a reconstruction of the original reference beam. This signal part is examined with regard to the feasibility to serve as feedback for focus detection, even though the object wave stems from a diffusely scattering surface.

3.7.1 Experimental set-up

Recording geometry A hologram is recorded with a frequency doubled Nd:YAG cw laser (Coherent Verdi V2). The spectral linewidth $\Delta\nu$ of the laser is specified as $\Delta\nu < 5$ MHz, corresponding to a longitudinal coherence length of $\Delta l = c \Delta\nu > 60$ m. Accordingly, no compensation for optical path length differences is arranged. The same holographic material and processing are chosen as for the application described in the above sections. The exposure time is one second. The laser power is adjusted to meet the hologram material requirements (www.geola.com). The recording geometry is shown in Fig. 3.21 (a). An object is placed in front of the hologram plate at a distance of approximately 15 cm. The object is illuminated by a fraction of the widened laser beam. The reference beam diameter is expanded by a telescope to a beam diameter of 1.5 cm. The beam impinges on

the hologram at an angle of 45 degrees to form an off-axis transmission phase hologram. The reference beam diameter determines the aperture of the hologram. A wedge is used to divide the laser into a reference and an object illumination beam, and a polarizer serves to adjust the intensities of the reference and object beam. The hologram plate holder is constructed to provide precise repositioning of the hologram after wet-chemical processing.

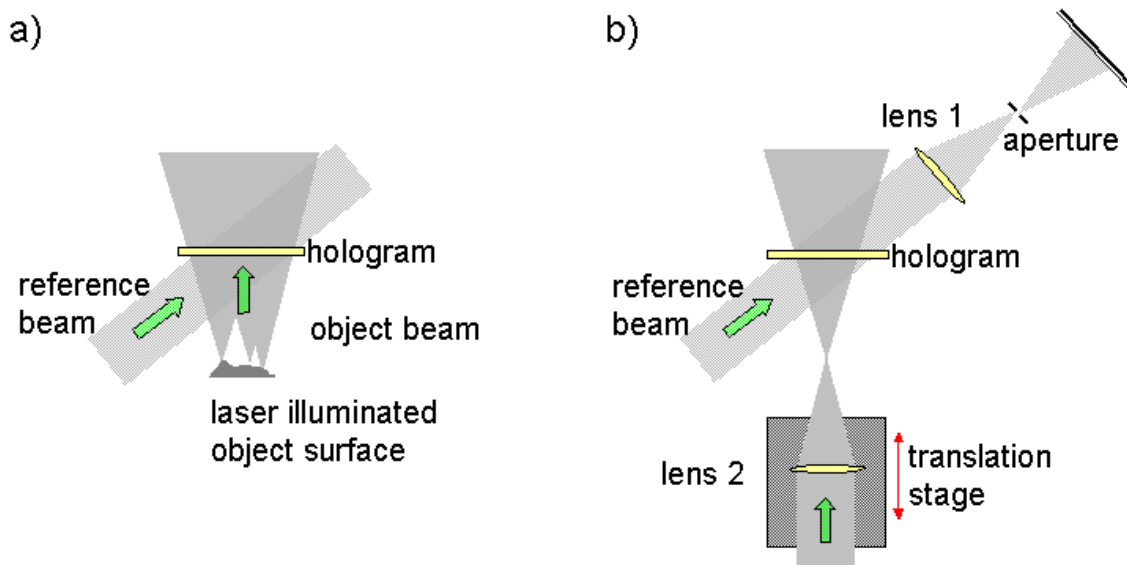


Figure 3.21: (a)Recording geometry of the hologram: The object wave is generated by laser illumination of a diffusely scattering object. The plane reference wave is superimposed on the hologram in off-axis geometry. (b) The object is replaced by a convex lens on a translation stage. The reference beam and the virtual image of the reference beam are spatially filtered behind the hologram, expanded and projected onto a diffusing screen attached to a CMOS scanner.

Read-out geometry The processed hologram is put back in the original position and the object is removed. The original reference beam is still available. A lens is used to focus a fraction of the laser beam in front of the hologram near the position of the surface of the original object. This is depicted in Fig. 3.21 (b). The focused laser spot simulates a part of the object wave and serves as reconstruction beam which is diffracted by the hologram. In this geometry, an exact copy of the object beam reconstructs an undistorted virtual image of the reference wave. To study the portion of the diffracted reconstruction

beam that coincides with the original reference beam, both are spatially filtered behind the hologram and imaged to a CMOS scanner.

Test set-up To test the set-up a hologram is recorded with a laser beam focused in front of the hologram serving as object beam, so the recording geometry corresponds to Fig. 3.21 (b). The focusing lens is mounted on an axial translation stage. After wet-chemical development, the hologram is put in the original position, and both object and reference wave are used as reconstruction beams. The original object beam is diffracted by the hologram to the virtual image of the reference beam. The virtual image of the reference beam and the original reference beam interfere on a screen behind the hologram as shown in Fig. 3.21(b). Interference is also observed for the object beam which transmits the hologram and the divergent virtual image wave of the object generated by the original reference beam. In the following, the discussion is restricted to the reference beam signal. The image wave diffracted from the object beam changes, if a mismatch of the divergence angle is introduced. As mentioned in section 2.3, the divergence of the image wave changes as well, leading to a scaling of the image wave. This is visualized in the change of the interference fringes formed by the original and the reconstructed wave which is shown in Fig. 3.22. The images were scanned with a CMOS scanner (the same as used in section 3.6). The axial distance of the lens from the original position is given underneath each image. Obviously, the further the lens is moved out of the original position, the smaller becomes the fringe spacing of the interference pattern indicating the growing deviation of the virtual image from the original wave front. This meets the expected interferometric result. The question then arises as to which extent this result can be transferred to the case of a diffusely scattering surface as object beam source.

3.7.2 Diffuse object

A diffusely scattering plane surface is used as object. To give the object a surface contrast, the illumination beam is modulated by a transparency with a random amplitude pattern that is projected onto the surface. If the illuminated object remains in the original position in front of the hologram, interference occurs with the original reference beam in agreement with the preceding test. The object is removed and a lens is simulating a scattering point on the object surface. This wave is referred to as reconstruction wave in the following (see Fig. 3.21(a) for the recording geometry, and (b) for the read-out set-up). As the hologram is illuminated with the reconstruction beam, a portion of the beam is diffracted along the direction of the reference wave. This has been treated in section 2.1, explicitly only for the reconstructed image wave in Eq. 2.10 for the real image, but analogue considerations are valid for the virtual image as well. The light diffracted in the direction of the reference beam

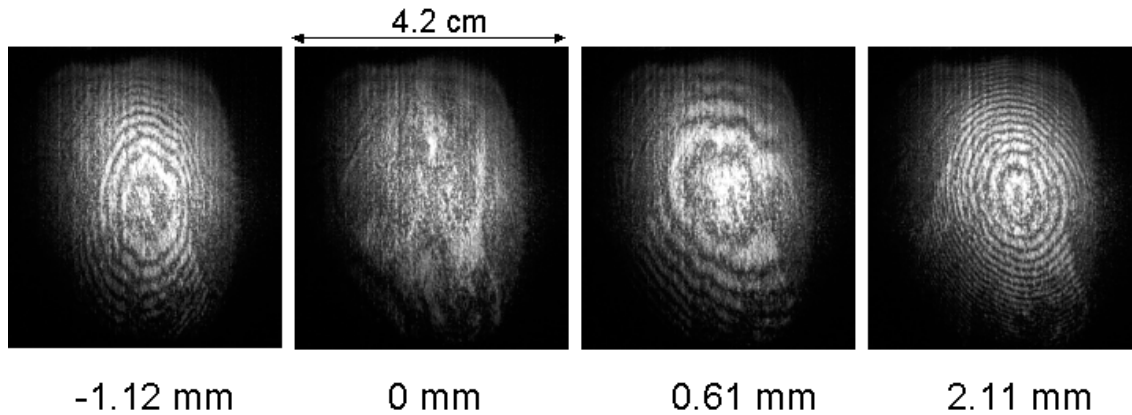


Figure 3.22: The interference pattern of the reconstructed and the original reference wave is recorded for different positions of the reconstructing wave focus (lens 2 in Fig. 3.21 (b)). The distance given under each image is the deviation from the original lens position. With increasing distance the fringe spacing in the interference pattern reveals the growing mismatch between the original and the reconstructed wavefront.

is accompanied by residual light from neighboring image points: If the focus of the lens matches a light scattering surface point of the original object, this light beam reconstructs the reference wave. But at the same time, the reconstruction wave acts as misaligned reconstruction beam for adjacent object points, which gives rise to the reconstruction of a spatially shifted virtual image of the reference beam. The resulting signal of the original reference beam and the reconstructed wave are shown in Fig. 3.23 in the focal plane of lens 1 in Fig. 3.21 (b).

Only the diffracted light that spatially coincides with the reference beam is correlated to light from a position of the original object surface. It is therefore necessary to filter this portion of the diffracted light to gain a signal that contains lateral and axial information of the object position. To this aim the reference beam and the diffracted light of the partial object beam are focused behind the hologram and an aperture selects the relevant signal part. Moving the reconstructing lens axially shifts the focal plane of the reconstructed signal.

The divergent beam behind the aperture is collimated and projected on a diffusing screen attached to the CMOS scanner. The resulting scans are shown in Fig. 3.24: The upper left image (a) is recorded if only the original reference beam illuminates the hologram. Part (b) of the figure shows the signal generated by the reconstruction wave. The lower row displays the intensity distribution of both beams superimposed on the detector. Part (c) shows the raw data recorded by the scanner. The interference pattern is then processed numerically: The difference signal of the sum of the images (a) and (b) and the interference pattern (c) is depicted in part (d). Obviously, the interference pattern does not contain

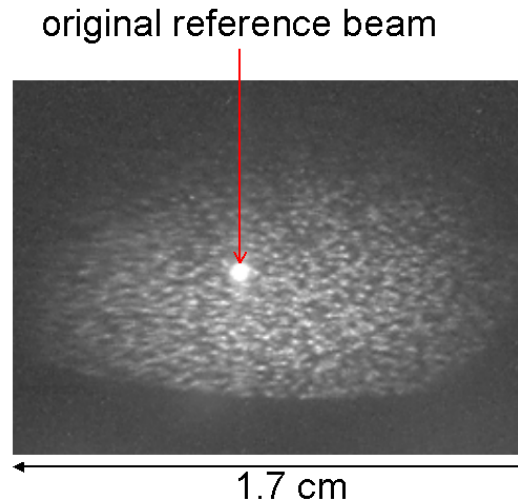


Figure 3.23: The original reference beam is focused and appears as bright spot (red arrow). The reconstruction beam is diffracted by the hologram. The extended diffusely scattering object wave source is only partially represented by the reconstruction beam. This leads to the reconstruction of spatially shifted signal beams, which are separated by an aperture.

a fringe or stripe pattern but represents a speckle interference pattern. The rough microstructure of the diffusely scattering surface is unresolved by the imaging system. This leads to a random phase modulation of the diffracted reconstruction wave, hence the image wave. Although this has a disruptive effect on direct interferometric focus detection in the way it is illustrated in Fig. 3.22, information on wavefront deformation can be extracted from speckle images, for instance by phase-shifting speckle interferometry, a well-established method for metrology of small surface changes [JP89], [NVSLCR04]. Therefore, in the next paragraph, the information content of phase shifting signals of the speckle interference pattern in the current holographic context is discussed.

3.7.3 Phase shifting signals

The random phase modulation of the speckle modulated image wave does not reveal information about the phase structure of the undisturbed image wave. Still, the interference pattern with the original reference wave may be used to visualize a phase change caused by a deformation of one of the coherently superimposed beams on the detector surface. Such wavefront deformation is expected for a changing reconstruction geometry, hence, a changing position of the reconstruction beam focus. Phase shifting techniques for the generation of secondary interference fringes to study a microscopic surface deformation are known as *Electronic* or *Digital Speckle Pattern Interferometry* (ESPI or DSPI), which are discussed in [Har96], for instance. The influence of wavefront deformation on the inter-

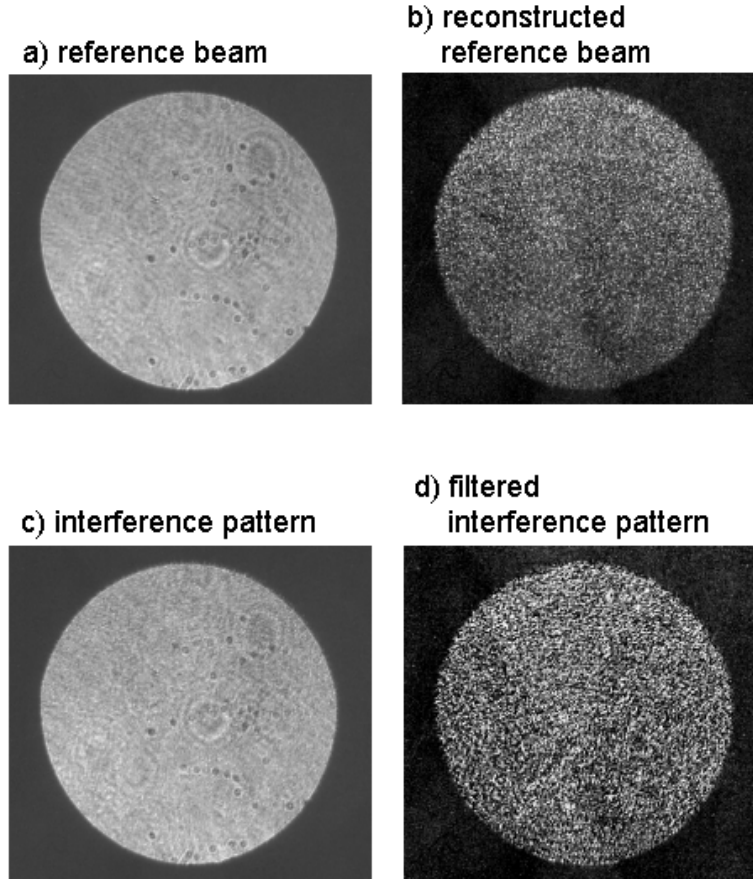


Figure 3.24: The original reference beam (a) and the reconstructed reference beam (b) are superimposed on the detector and form the intensity distribution (c). The difference between the summed intensities of the single beams and the superimposed intensity (c) is shown in part (d).

ference pattern is introduced by comparing two intensity distributions on the electronic detector (assumed in the (xy) -plane of the cartesian coordinate system) for two states before and after deformation (see Eq. 2.5):

$$I_1(x, y) = s^2(x, y) + r^2(x, y) + 2s(x, y)r(x, y) \cos(\phi_s(x, y) - \phi_r(x, y)) \quad (3.3)$$

$$= s^2(x, y) + r^2(x, y) + 2s(x, y)r(x, y) \cos(\phi_1). \quad (3.4)$$

Here, r and s are the real amplitudes and ϕ_r and ϕ_s the phases of the reference wave and the speckle modulated wave field. In this context, the latter is the diffracted image wave which undergoes deformation depending on the reconstruction geometry. (As usual, the spatial variables (x, y) are not always written out for a clearer notation.) If only a phase change occurs, and the second interference pattern is recorded, this can be written as

$$I_2(x, y) = s^2 + r^2 + 2sr \cos(\phi_1 + \Delta\phi). \quad (3.5)$$

Due to the random phase variation of s the intensity in each of the two interferograms I_1 and I_2 varies across the detector area. But still the change $\Delta\phi$ of the phase between two waves caused by the deformation of s is independent of the initial intensities. It is visualized by subtracting the two intensity patterns, or to avoid negative values, by calculating the absolute value of the difference of the intensities I_1 and I_2 . If the optical path length between reference and object wave at point (x, y) on the detector changes by an integer multiple of the wavelength, the subtraction signal is dark. A bright value corresponds to a phase change of an odd integer multiple of π . Hence, a contour of the wavefront deformation is generated by the secondary interference pattern.

Phase shifting images are shown in Fig. 3.25. To record the intensity distributions I_1 and I_2 , lens 2 in Fig. 3.21 is moved to an initial position, first, with the focus of the lens near the surface of the original object. Then the lens is moved 2 mm out of this position. Part (b) of Fig. 3.25 shows the resulting difference image. A second phase shifting signal is recorded 5 cm out of the first position closer to the hologram surface. Again, a lens shift of 2 mm yields the difference signal, which is shown in part (c) of the figure. Finally, the lens is moved away from the hologram 8 cm behind first lens position. From this starting point, the third set of images with a 2 mm lens shift is recorded. The difference image for this position is shown in Fig. 3.25 (a).

These difference images consist of concentric rings revealing a mainly spherical deformation of the reconstructed reference wavefront. Furthermore, the deformation increases as the lens approaches the hologram. Consideration of path length differences yields that this corresponds to an increased distance of the focus of the reconstructed reference image behind the lens 1 in Fig. 3.21 (b) to the scanner plane. Obviously, the change of the reconstructed image leads to a phase shift signal which is sensitive to the position of the reconstructed virtual image. In contrast, if the original reference beam is moved along the beam axis, a difference image results in a stripe pattern instead of concentric fringes. This indicates a tilt of the reference beam due to the a slight deviation of the moving direction from the beam axis. Such an image is shown in Fig. 3.26.

In conclusion, the reference beam may be reconstructed as virtual image from an unknown diffuse object beam. The disturbing signal part from adjacent object regions is separated by spatial filtering. A random phase modulation of the reconstructed beam caused by the micro-structure of the scattering object surface has to be taken into account. The speckle structure of the reconstructed reference wave perturbs the formation of an interference pattern of the original and the reconstructed reference wave that directly relates to the focus position. A measurement of the deformation of the reconstruction wavefront can be accomplished by calculating difference images from speckle interference patterns. The resulting secondary interference fringes relate to the wavefront deformation

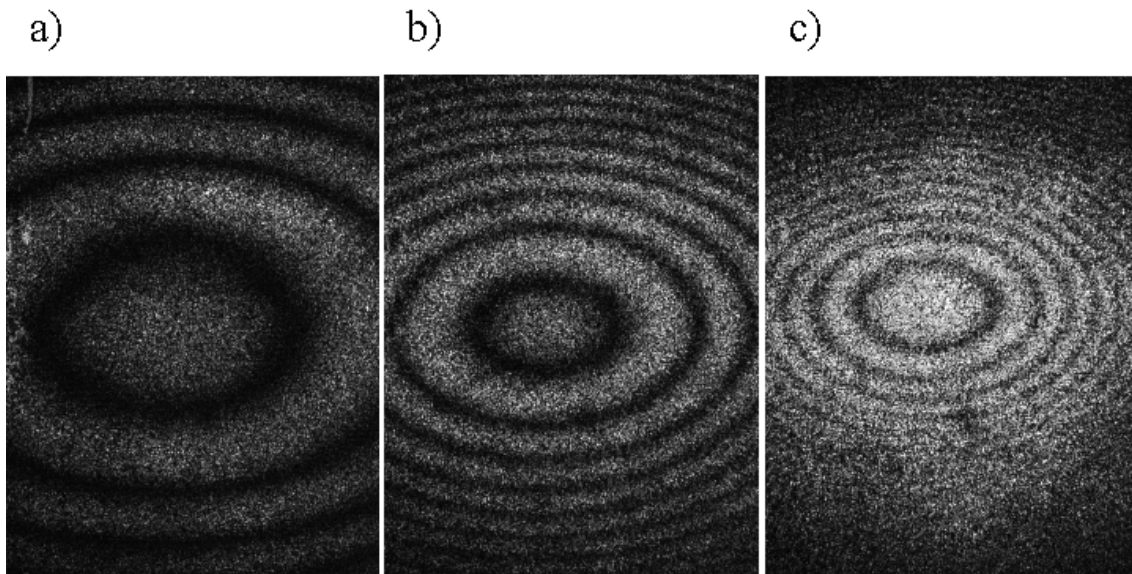


Figure 3.25: Secondary fringe patterns are generated by wavefront deformation of the reconstructed reference wave. The fringe spacing depends on the initial distance of lens 2 (see Fig. 3.21) to the hologram plate, which decreases from the left to the right image (see text for details).

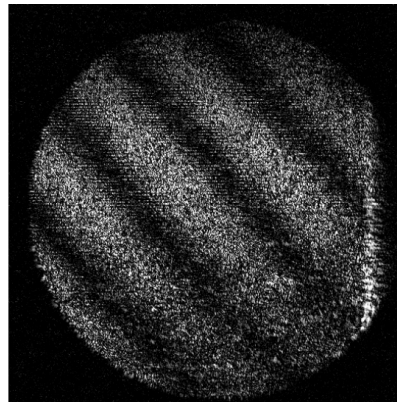


Figure 3.26: Secondary fringe pattern generated by changing the reference wave beam path. The stripe pattern reveals a tilt of the reference beam between the two recordings.

caused by a change in the reconstruction geometry.

To remove the speckle structure that impedes interferometric focus detection for a diffusely scattering object, the reconstruction wave must resolve the surface structure of the object. To this aim, aberration free focusing is crucial. For future work, replacing the lens that forms the reconstruction beam by a focusing mirror is most promising to provide a speckle free signal for interferometric focus detection.

3.8 Summary

This chapter has focused on experimental issues for holographic facial measurement. A holographic camera has been described that comprises a pulsed laser system working at the wavelength 526.5 nm. It provides laser pulses of 35 ns pulse duration at a maximum pulse energy of 2 Joules. The pulsed lensless recording technique makes the recording procedure simple and robust against environmental influences and even allows for mobile holography. Recordings can be made eye-safe by expanding the laser beams and inserting diffusor plates at the object illumination laser ports.

Additional mirrors can be added to the set-up that show the object from various views in a single hologram. The reconstruction geometry is chosen to allow for projection imaging of large image volumes (containing mirror views, for instance) by adding a flexible scan axis. Hence, side views of a sitting person cannot only be recorded as shown already in [Gie03], but they may also be reconstructed and digitized resulting in a computer model (see chapter 4 for a presentation of the results). Using mirror views and the extended hologram reconstruction set-up, panoramic imaging of an object from a single pulse hologram is possible.

In contrast to earlier work [Gie03], [Bon02], the presented optical read-out arrangement of the hologram allows to compensate for aberrations of the holographic image. This alignment of the hologram is the basic precondition for high resolution imaging and the appearance of skin pores in the real image. Detection of these skin pores is used for surface detection (see chapter 4), so the enhanced image quality in the real image is crucial for the extraction of textured computer models from eye-safe recordings without projection of a stripe or speckle pattern.

Image accuracy over an extent of more than 20 cm has been tested by recording and reconstructing rulers, showing that the image reconstruction can be aligned to match the original object, if small aberrations of the real image can be accepted. Minimization of aberrations by using the real image of a Siemens star has been demonstrated. Digitization of the real image is improved by avoiding an intermediate imaging step on a diffusing screen. A direct scan of the real image improves the noise characteristics of the digital data and does not require calibration. Specific artifacts appearing with the scan technique have been discussed, and it is shown that these artifacts do not affect focal regions, and thereby the quality of the resulting models.

A decisive advantage of the presented holographic imaging system compared to photogrammetric systems, laser scanners or fringe projection systems is that the whole imaging procedure works without lenses and is therefore calibration free. Furthermore, due to the short recording time, the procedure is very robust against instabilities of the object or the environment which are a problem for laser scanners and fringe projection systems. Refer-

ring to the new mobile system, the light conditions for the recording are uncritical. The system is very fast and easy to operate, so recordings are most comfortable for the operator and the patient as well.

Apart from the improved procedure for large scene hologram digitization, a second complementary imaging concept is investigated. It is based on the reconstruction of the reference beam by illuminating the hologram with a partial object beam, which is scanned through the object volume. It is shown that this imaging scheme is generally suitable for interferometric focus detection, but suffers from speckle noise for diffusely scattering object surfaces that are not fully resolved by the reconstruction beam. This has to be addressed in future work. Phase shifting has been applied to show wavefront deformation of the reconstructed beam for changing reconstruction geometries.

This last aspect can be considered separately from the imaging scheme that is actually used for medical facial imaging. This scheme relies on real image reconstruction. After the digitization unit of the real image has been subject of the current chapter, the following chapter shows how the object surface can be retrieved from the scanned real image by digital image processing.

Chapter 4

Shape-from-focus in the real image

Digital image recording and processing are employed to digitize and evaluate the real image. As result of the scan of the real image which is described in the experimental section 3.6, the three-dimensional image volume of the holographic real image is available as discrete digital image set. The data consists of an image sequence of equidistant projections of the holographic real image. This is visualized for two scan sequences in Fig. 4.1 by showing three projections of each sequence. As the scanner moves through the real image of the object, sharply imaged contours of the object appear depending on the scanner's position: Close to the hologram surface the projection shows the tip of the nose in focus. As the scanner is moved away from the hologram, the contour moves across the recorded face. The upper row shows projections of a surface recorded with contrast enhancement by speckle illumination, while the row below displays a facial surface which is illuminated with diffusor plates in the object illumination beam. In this case, the recording is eye-safe, but the image contrast that has to be detected in the real image is lowered.

To retrieve the object surface from these projections, sharply imaged contours are identified in each image of the recorded sequence and related to the respective scanner position, yielding a three-dimensional depth map of the surface. The task of surface measurement from an image sequence of the real image is equivalent to focus detection in a series of images with moving focal planes and a limited depth of field. This focus detection procedure is known from sectional light microscopy. Techniques that use this principle are known as *shape-from-focus*, *depth-from-focus* or *extended focus*. In this field the problem arises that with increasing enlargement of the observed object the range where one gets sharply imaged contours becomes smaller which impedes imaging of three-dimensional objects. To solve this problem, the object is moved along the optical axis and a series of images is recorded digitally. Auto-focusing methods are then applied to these images and sharp contours are extracted and merged to give an image of the object. A classical focus measure

is the gray scale variance of the pixel values calculated in a specified pixel neighborhood for each lateral position. Maximization of the variance value along the scan axis yields the focus position. A faster algorithm is provided by [NN94], named SLM (sum modified Laplace operator) or alternatively, a method using Tenengrad operators has been proposed (a review on these techniques can be found in [SCN93], for instance). Still, the basic principle of these procedures is the evaluation of lateral image contrast in a local pixel window for focus detection. Such strategies are summarized as contrast maximization methods. Inverse data filtering by image deconvolution is another approach to this task. The feasibility of image deconvolution for the holographic sectional images has been studied in previous work [Gie03] concluding that despite a very long processing time, contrast maximization still outperforms this method.

In the following sections, focus features and the imaging geometry in the holographic data volume are studied to decide in how far contrast maximization can be adopted from extended focus techniques. The merits and the problems arising from this approach are discussed and a refined in-focus criterion is developed based on these considerations. It is based on axial focus features instead of a lateral pixel window evaluation and still shows sufficient robustness against image noise. The problem of local windows for contrast maximization has been discussed in [AFM98] and an alternative method is proposed there. But this method requires the input of the exact imaging geometry. In contrast, the method proposed in the following chapter is mathematically simple and works blindly, which makes it insensitive to image aberrations, shading and changes in the set-up. After presenting the general focus geometry and the mathematical notation in the following section 4.1 and deblurring techniques in section 4.2, contrast maximization is treated in section 4.3, followed by a description of refinement of the focus detection procedure based on axial focus features in section 4.4. Finally, the results of the procedure, precisely textured facial models, are presented in section 4.5. The image processing presented in the next sections is written as plug-ins for the Java-based image processing environment ImageJ [Ras], [AMR04].

Fourier transforms and filtering are performed using ImageJ plug-ins by Nick Linnenbrügger (plug-in FFTJ) and Joachim Walter (plug-in FFT Filter), the plug-in TransformJ [MNV01] is used for geometrical transformations on the image volume.

4.1 Focus features and geometry

The general axial focus geometry is depicted in Fig. 4.2 using the simplifications of geometrical optics. Image points not lying on the scan axis are called off-axis points. For those points the *pixel correspondence line* (pcl) is introduced [AFM98]: The lateral pixel position which corresponds to an image feature changes for varying axial scan positions.

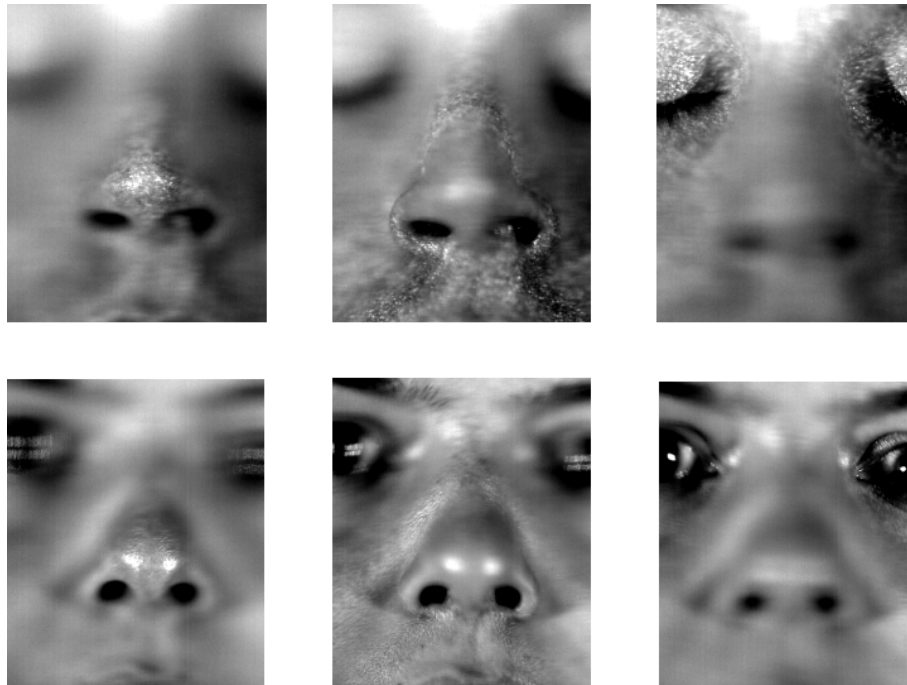


Figure 4.1: Projection images of the real image of facial surfaces. The upper row shows a surface recorded with contrast enhancing speckle pattern projection, the lower row shows a surface recorded eye-safe with homogeneous laser illumination.

The line connecting these pixels is called the pixel correspondence line. It was successfully introduced for our system by [The03], [TBG+05]. In this approach it was defined as straight line between the image point and the hologram center, assuming shading and aberrations as negligible. Suitable focus measures have to be developed that are typically maximized along the scan axis or the pcl.

In the following discussion, the terms *lateral* and *axial images* will be used, which is explained by Fig. 4.3. Part (a) shows images that display the intensity in a plane perpendicular to the scan axis and are referred to as lateral images. The in-focus regions in the middle image appear sharp and gradually blur with increasing distance of the reconstructed object surface and the plane of the image projection. Part (b) shows an axial cut through the image volume, gained by a 90 degree rotation of the original data around a lateral axis. Both axial and lateral images are examined to derive suitable focus characteristics that can be detected numerically.

The main feature that is used in lateral images is image contrast, which has a maximum in focused regions (contrast maximization methods). A general characteristic of these methods is that they are based on the analysis of a local pixel neighborhood. Because of image overlap, this strategy is susceptible to a transfer of the intensity distribution on the object surface to the detected shape (see below for details). Therefore it is useful to consider axial focus features as well to refine the results. To prevent falsely detected focus

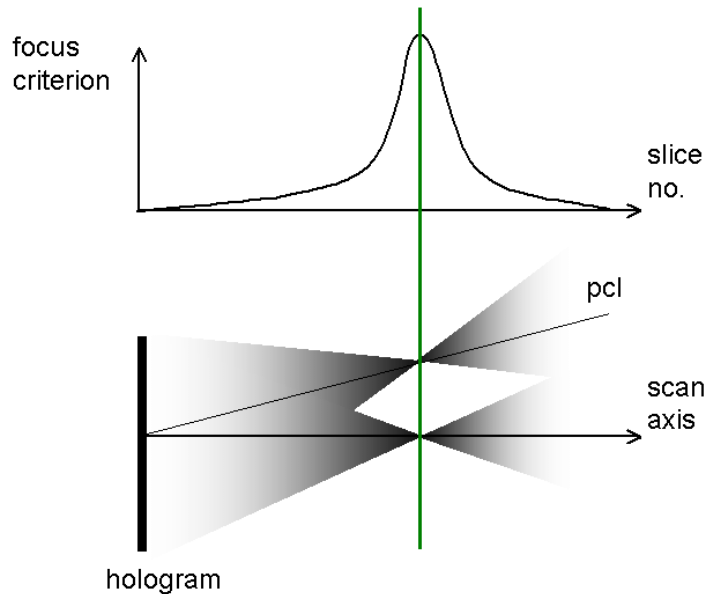


Figure 4.2: Axial cut through the real image in a simple model: Focus features are used for numerical focus detection. For this, a focus criterion is calculated with a maximum along the scan axis or the pcl that is related to a surface point.

points, the influence of blurred image parts and sharp caustic edges near the focus has to be minimized. Four focus features are decisive for a good result:

- Focused image regions differ from blurred image parts by their spatial frequency formation. Blurred image parts can be filtered out by applying a high pass filter either in the spatial or in the frequency domain. This subject is treated in section 4.2.
- In lateral images, focused regions display a high image contrast. Contrast maximization methods are a standard solution for shape-from-focus problems. A contrast measure, such as the variance of the intensity values, is calculated in a local pixel neighborhood and the maximum is detected along the scan axis. Such a procedure and the results for holographic data are presented and discussed in section 4.3.
- Considering axial images, a focus is characterized as dip or peak of the intensity along the scan axis. An algorithm is presented that detects these focus features taking into account effects from off-axis light propagation and shading. The method is compared with focus detection by contrast maximization.
- Another axial focus feature is point symmetry of the intensity in the focus with regard to the pixel correspondence line. This characteristic is used as selection criterion to

differ between valid surface points and falsely detected focus points due to caustic edges. This and the preceding item are investigated in section 4.4.

Before these procedures are presented in detail, notations necessary for a mathematical description are defined.

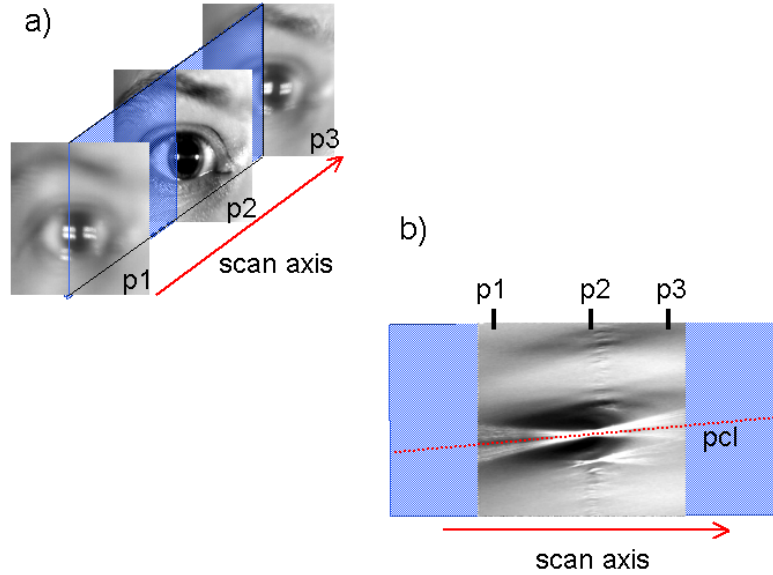


Figure 4.3: Part (a) shows three images of an image sequence. The middle image displays focused regions. The image features gradually deblur with increasing distance from the focus. Looking at the image series "from the side" by rotating the image volume 90 degrees around the vertical axis reveals additional focus features. The pixel correspondence line is shown as red line.

4.1.1 Image representation and pre-processing

The 3D image volume of the holographic real image is sliced into a set of equidistant 2D projections. The intensity of these projections is digitized by sampling the continuous images in a set of 2D gray-level digital images. These images are represented as 2D discrete matrices

$$A^z = a^z(x, y), a^z(x, y) \in G, G = \{0, 1, \dots, 255\}, \quad (4.1)$$

of the dimension $X \times Y$. Throughout the next sections, the index x is the line index of an image, and y is the column index, counted from the upper left corner of the image. X is the image width, and Y the image height. The index z assumes integer values $0 \leq z < Z$. Z is the total number of scanned images.

Depth and texture map Focus detection results in a depth map which assigns a value of the focus position $z_{max}(x, y)$ to every lateral position (x, y) . If $Z \leq 256$, $z_{max}(x, y)$ can

be visualized as 8 bit gray scale image. The pixel brightness refers to the slice number z of the detected focus position. Black pixels in the depth map correspond to slice number zero, and white pixels belong to a focus position in slice number 255. The scan direction can vary and lead away from the hologram or move towards it. The intensity $a^{z_{max}}(x, y)$ in the real image that is associated with the depth map $z_{max}(x, y)$ is called texture map.

Normalization With increasing distance from the hologram, the total image brightness $S^z = \sum_{x=1}^X \sum_{y=1}^Y a^z(x, y)$ decreases. This is compensated numerically. The images are normalized to fulfill the condition $S^z = S_0$:

$$b^z(x, y) = \frac{S_0}{S_z} a^z(x, y). \quad (4.2)$$

The choice of S_0 might vary depending on the intensity dynamics of the image sequence. The default value is set to $(50 \times X \times Y)$. The normalization step is applied to all data without being further mentioned.

Shift The image sequence captured with the set-up shown in Fig. 3.12 allows to adjust the scan axis for a scan along the central pcl horizontally. The central pcl might still deviate from the scan direction vertically which is compensated numerically by shifting each slice of the scan for the required amount of pixels. This amount is determined manually by identifying a feature and the corresponding lateral position in two separate images of the scan sequence and assuming a linear shift through the sequence to calculate the amount of pixel shift for each image for a registered image stack.

4.2 Image deblurring

Fig. 4.4 shows an axial cut through the real image. Raw data is shown in part (a). The surface which has to be detected in this data can be retrieved by finding foci from skin pores. This intensity modulation consists of spatial frequencies considerably higher than that of defocused image parts that surround the contour. Irrespective of the method used for focus detection blurred image parts are a source of falsely detected surface points. Therefore one usually regards high pass filtering as adequate mean to deblur such raw image data to prepare the image sequence for the actual focus detection. The result of spatial filtering is shown in part (b) of the figure. Here, a filter procedure according to Eq. 4.10 was applied (see below) and the surface appears as bright contour. Besides blurred image parts, high frequency noise can disturb the detection. Therefore both high pass filters and low pass filters are used.

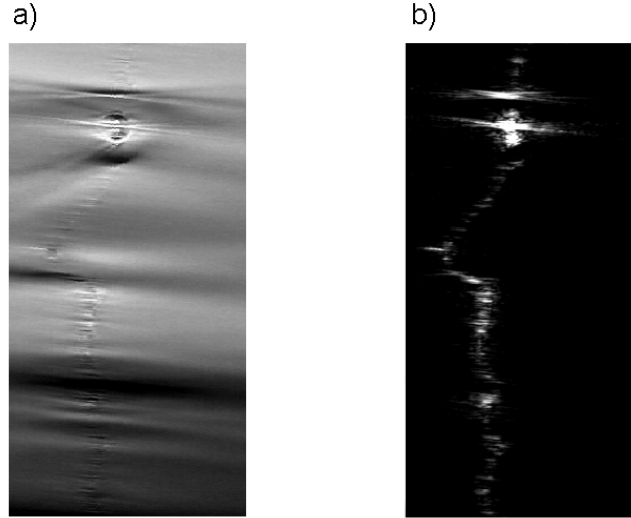


Figure 4.4: A facial profile is depicted as it appears in the real image in an axial cut. Part (a) shows raw scanner data. The intensity modulation due to skin pores has to be detected numerically for surface detection. Spatial frequencies corresponding to these skin pores are selected by spatial filtering according to Eq. 4.10. This yields image (b) with the facial profile appearing as bright contour.

4.2.1 Fourier-based filtering

Fourier-based filtering relies on the extraction of spatial frequencies that belong to sharply imaged points (see [dFCJ01], for instance). The continuous 2D Fourier transform of an image $a(x, y)$ is defined as

$$\mathcal{A}(u, v) = \int_{-\infty}^{\infty} \int_{-\infty}^{\infty} a(x, y) \exp\{-2\pi i(ux + vy)\} dx dy. \quad (4.3)$$

The inverse Fourier transform of $\mathcal{A}(u, v)$ is

$$a(x, y) = \int_{-\infty}^{\infty} \int_{-\infty}^{\infty} \mathcal{A}(u, v) \exp\{2\pi i(ux + vy)\} du dv. \quad (4.4)$$

Fourier pairs are denoted as

$$a(x, y) \longleftrightarrow \mathcal{A}(u, v). \quad (4.5)$$

For an image $a^z(x, y)$ the discrete Fourier transform (DFT) is defined as

$$\mathcal{A}^z(u, v) = \frac{1}{XY} \sum_{x=0}^X \sum_{y=0}^Y a^z(x, y) \exp\left\{-2\pi i\left(\frac{ux}{X} + \frac{vy}{Y}\right)\right\}. \quad (4.6)$$

The inverse DFT of $\mathcal{A}^z(u, v)$ is

$$a^z(x, y) = \sum_{u=0}^X \sum_{v=0}^Y \mathcal{A}^z(u, v) \exp\left\{2\pi i \left(\frac{ux}{X} + \frac{vy}{Y}\right)\right\}. \quad (4.7)$$

The 2D DFT may be computed by a 1D DFT of the image rows followed by a 1D DFT of the image columns (separability). High image frequencies relate to small image structures. A low pass filter corresponds to spatial smoothing and is used to remove image noise. High pass filtering is adequate to remove blurred and thus defocused structures. The frequency band that is kept for further image processing has to be adapted to the size of the surface structure that is displayed in focused regions. The effect of Fourier filters is illustrated in Fig. 4.5. Part (a) shows raw data. The (logarithmic) power spectrum of the Fourier transformed image is shown in part (d). Low frequency components are displayed in the center of the Fourier transformed image by convention. After applying a low pass filter, image (b) appears smoothed. The corresponding low frequencies are damped (part (e)). Parts (c) and (f) show the influence of a high pass filter.

Stripes appear as scan artifacts caused by the lens array in front of the CMOS detector (see section 3.6). These vertical stripes appear on the horizontal axis of the 2D Fourier transformed image and can be eliminated as well.

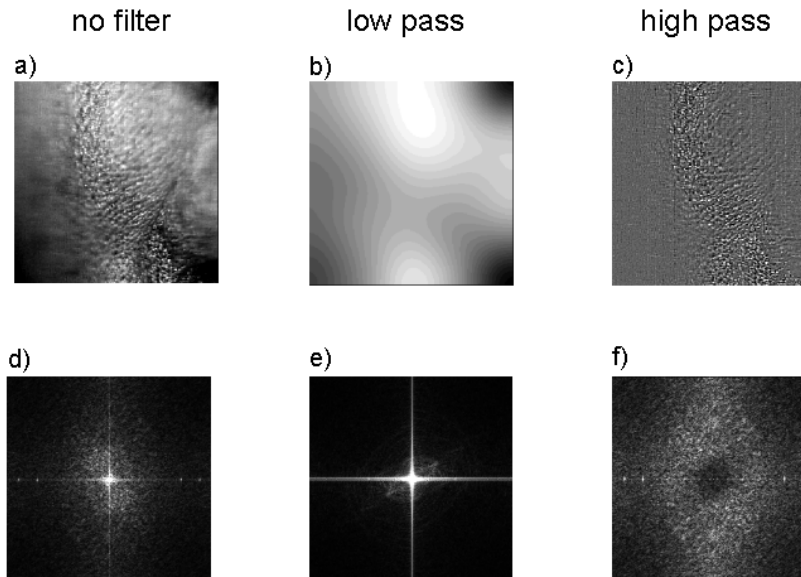


Figure 4.5: Illustration of the correlation between image features in the spatial domain (first row) and the frequency domain (second row): (a) and (d) raw data; (b) and (e) low-pass filtered data; (c) and (f) high-pass filtered data.

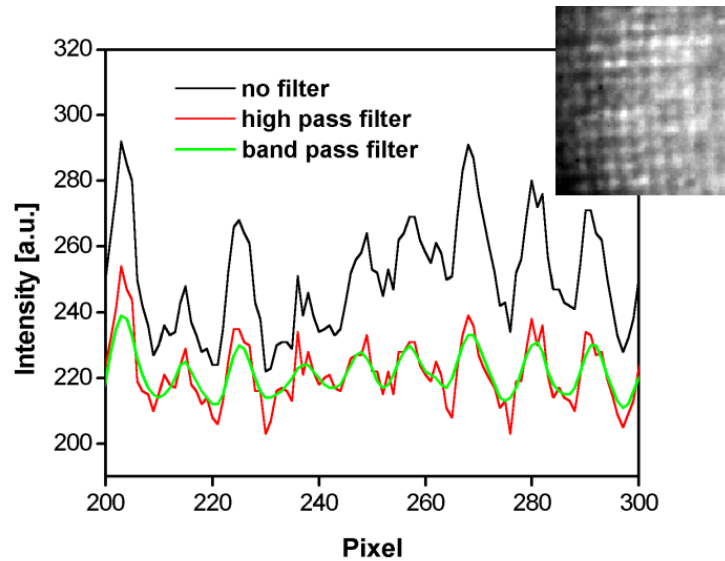


Figure 4.6: The influence of band pass filtering on the image intensity: A periodical grating pattern is projected (see inset). The intensity along a line section is shown (black curve), high pass filtering results in the red curve, band pass filtering yields the green curve.

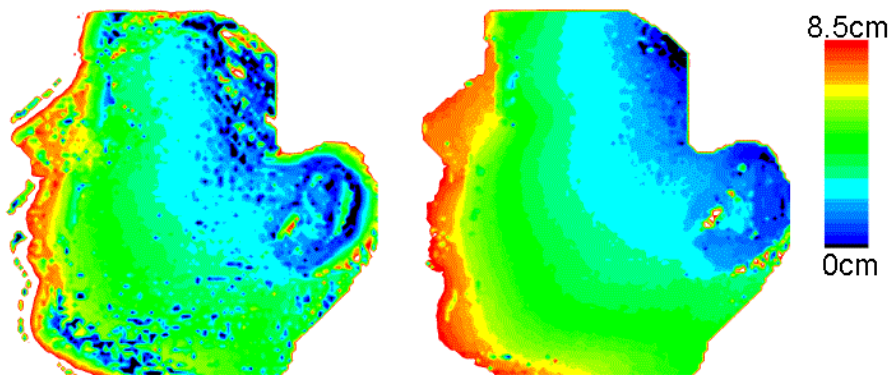


Figure 4.7: A side view of a face is recorded on a hologram, and a periodic grating is projected for contrast enhancement. The surface is found by contrast maximization (see below). Two depth maps are shown, the left is gained from raw data, the right is calculated after band pass filtering.

The efficiency of Fourier band pass filtering can be enhanced by projecting a periodic structure onto the object surface. An example is given in Fig. 4.6: A grating pattern is projected on the facial surface (see [Bon02] for stripe projection techniques). The pattern is shown in the inset of the figure. A section through the image displays the periodic intensity distribution and is shown as black curve. Application of a Fourier high pass filter results in the red curve, and subsequent low pass filtering yields the green curve. Fig. 4.7 shows the positive effect of this band pass filtering on the depth map that is gained from the filtered data. These depth maps are calculated by contrast maximization, which is

explained in section 4.3. The left part of the figure shows the depth map retrieved from raw data: The surface presents a side view of a face and is expected to be closed and smooth. Obviously, noise disturbs the surface detection. This effect is greatly reduced by band pass filtering of the raw data. The resulting depth map is displayed in the right part of the figure.

4.2.2 Spatial filtering

In the spatial domain, low pass filtering corresponds to a convolution of the image with a filtering window. The spatial approach results in a faster processing of data than the application of frequency domain filters. This is due to the large image size ($> (1000 \times 1000)$ pixels) and the comparatively small windows ($< (10 \times 10)$ pixels) used in standard applications of facial measurement.

Average filtering is achieved if each pixel of the image is replaced by an average value of the gray levels in a pixel neighborhood.

The new image $b^z(x, y)$ is calculated from

$$b^z(x, y) = \sum_m \sum_n h(m, n) a^z(x - m, y - n). \quad (4.8)$$

For a (3×3) -neighborhood $h(m, n)$ would be

$$\begin{pmatrix} 1/9 & 1/9 & 1/9 \\ 1/9 & 1/9 & 1/9 \\ 1/9 & 1/9 & 1/9 \end{pmatrix} \quad (4.9)$$

for $(-1) \leq m \leq 1$ and $(-1) \leq n \leq 1$.

Of course there is a number of other possible smoothing functions, like Gaussian smoothing and Median smoothing. An exhaustive discussion can be found for example in [dFCJ01].

For high pass filtering, a subsequent algebraic operation is carried out:

$$c^z(x, y) = |a^z(x, y) - b^z(x, y)|. \quad (4.10)$$

By taking the absolute value of the difference, dark image points are transferred to bright image points, which is sometimes useful. If this effect is unwanted, the difference is calculated and a constant is added to avoid negative values. An example for the effect of this procedure is illustrated in Fig. 4.8: A lateral image of a facial surface is shown (part (a)). The image part contains focused skin pores as well as blurred light from neighboring focal planes. Part (b) shows the same data after applying Eq. 4.10 with a (9×9) pixel neighborhood.

Deconvolution This method has been applied by our team in previous work [Gie03]. Image blur is considered as unwanted filtering or convolution (denoted by \circ) of the image $e^z(x, y)$ with a filter function $h^z(x, y)$ resulting in the image $a^z(x, y)$.

$$a^z(x, y) = e^z(x, y) \circ h^z(x, y). \quad (4.11)$$

To recover $e^z(x, y)$, the convolution theorem is applied (the arrows denote Fourier pairs):

Convolution theorem [dFCJ01]:

Let $a^z(x, y) \longleftrightarrow \mathcal{A}^z(u, v)$ and $h^z(x, y) \longleftrightarrow \mathcal{H}^z(u, v)$.

Then $(a^z \circ h^z)(x, y) \longleftrightarrow \mathcal{A}^z(u, v)\mathcal{H}^z(u, v)$

and $a^z(x, y)h^z(x, y) \longleftrightarrow (\mathcal{A}^z \circ \mathcal{H}^z)(u, v)$.

Thus, $e^z(x, y)$ is the inverse Fourier transform of $\mathcal{A}^z(u, v)/\mathcal{H}^z(u, v)$ for non-zero values of $\mathcal{H}^z(u, v)$.

If the point spread function (PSF) of the imaging system is known, it defines the filter function. Otherwise blind deconvolution has to be used. Image noise is one of the main problems in deconvolution techniques. For an efficient procedure sophisticated techniques have been developed. Despite very long computation times due to the large amount of data the deblurring results using deconvolution techniques were of minor quality [Gie03].

4.3 Contrast maximization

Based on the above image processing tools, contrast maximization can be defined in the following way. First, spatial high pass filtering is used according to

$$c^z(x, y) = |a^z(x, y) - b^z(x, y)|, \quad (4.12)$$

with b an averaged image as defined in 4.8.

Then in a second step summation is performed,

$$d^z(x, y) = \sum_m \sum_n h(m, n)c^z(x - m, y - n), \quad (4.13)$$

where h denotes an averaging operator containing $(m \times n)$ equal or weighted entries.

The procedure is visualized in Fig. 4.8. Part (a) shows raw data, (b) shows the image treated with a high pass filter according to Eq. 4.12, and (c) shows the influence of summation over a pixel neighborhood.

Instead of Eq. 4.12 other high pass filter algorithms can be used. The *Sum Modified Laplacian* (SML) technique as given in [NN94] uses second order derivatives as high pass filter before summation is performed. Instead of the absolute value of the difference to the local image average, pixel variance is an alternative well established measure [Gie03], [Die02].

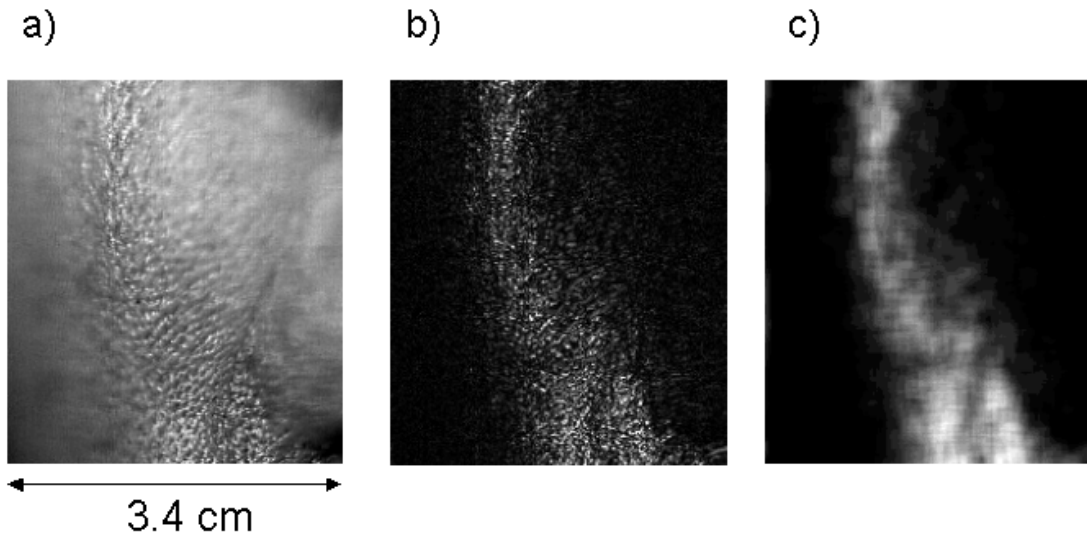


Figure 4.8: (a) Original image, (b) high pass filtered image, (c) high pass filtered image with subsequent pixel summation in a local pixel neighborhood

The summation step yields a great stability against image noise, which becomes better with a growing pixel neighborhood. It is therefore an essential tool for standard data evaluation. It provides a good first guess of the surface which can be the basis for further refinement if needed. As can be seen from Fig. 4.8 (c), the summation step smears out the intensity of the structure. The price of the resulting robustness is clustering in the detected contour. Smearing out the intensity distribution leads to an influence of bright points on adjacent pixels. The intensity distribution on the surface is then transformed in a depth modulation on the numerically detected surface. This is enhanced by sharp caustic edges that induce a high image contrast in the neighboring pixels of a bright image point. This contrast shines out the "real" surface point and leads to a wrong z position for the corresponding lateral point in the depth map. The clustering effect is demonstrated in Fig. 4.9, which shows the detected contour inserted into the original image. So far, only a lateral image feature has been evaluated. The following section demonstrates how the detected surface can be refined by including axial focus features into the search strategy.

4.4 Focus detection based on axial features

The aim of the procedure presented here is to avoid clustering due to the use of a local pixel neighborhood as well as to reduce the influence of sharp caustic edges on adjacent image regions. Axial instead of lateral focus features are investigated, and foci are detected without evaluation of a local pixel neighborhood.

A focus appears as a local extremum (maximum or minimum) in the real image. As-

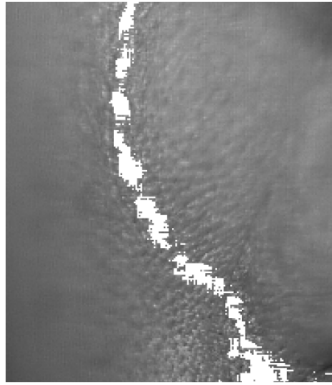


Figure 4.9: Surface contour detected by contrast maximization.

suming a maximum search in the (yz) -plane along the z direction as shown in Fig. 4.10(a), obviously some y positions (or generally some lateral positions) do not correspond to a focus point. Instead, inevitably wrong z -positions are found from intensities belonging to neighboring foci. An intensity maximum might stem from a caustic edge, which leads to systematic artifacts in the resulting detected shape.

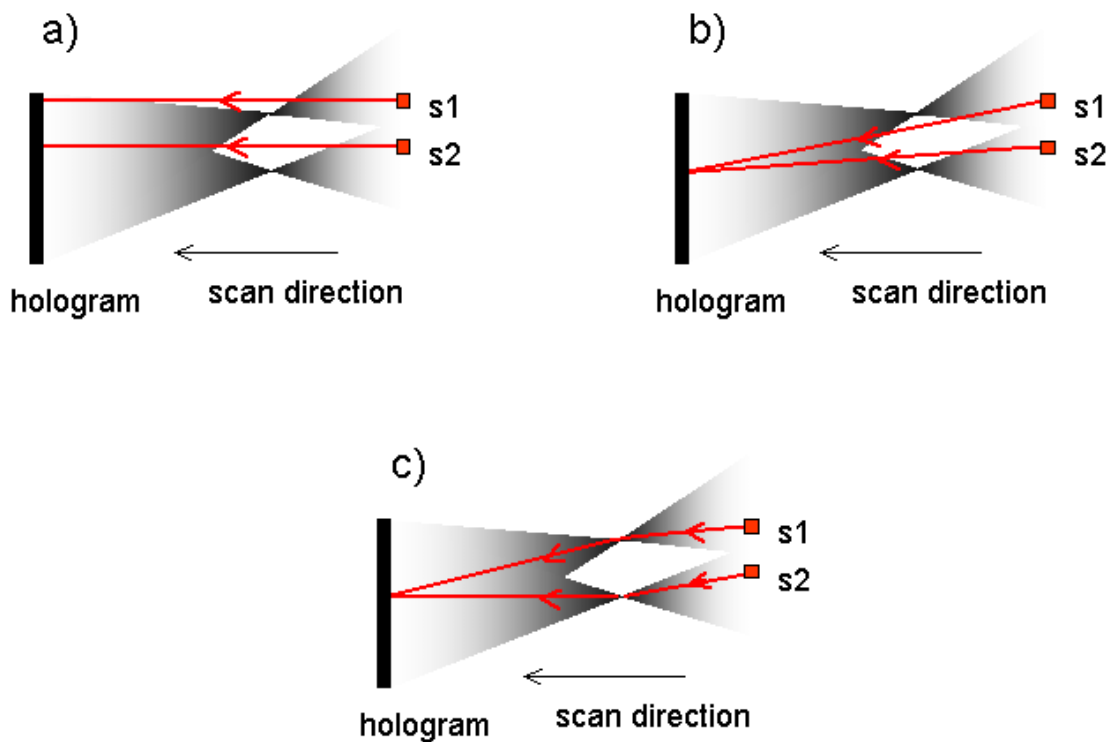


Figure 4.10: Examples for search directions: a) along the scan axis; b) along the pixel correspondence line; c) following increasing intensity

This effect still appears if the pixel correspondence line is followed (see part (b)). Part (c) of the figure depicts the proposed solution: A flexible search direction is introduced. It is determined by the direction of maximum intensity. The following improvements are expected from this approach:

- Selectivity: Not every lateral position is assigned to a surface point: Several lateral starting points of the maximum search can end in the same focus spot by the increase of intensity near the focus. Selection of surface points instead of smearing out bright spots into neighboring regions should avoid clustering in the detected contours.
- Reduced influence of caustic edges: By a flexible maximum search the brightness of caustic edges is compared with the brightness in the corresponding focus spot. Therefore it is not identified as global maximum along the search path.
- Robustness against off-axis effects and shading: The adaptive search direction follows the propagation direction of the image forming wave.

For a single focus point and a single search point, such a search strategy can be put into practice as follows.

The task is to find the intensity maximum in the three-dimensional search space of the parameters $x \in \{0, 1, 2, \dots, X - 1\}$, $y \in \{0, 1, 2, \dots, Y - 1\}$ and $z \in \{0, 1, 2, \dots, Z - 1\}$.

The maximum search starts from a point P_0 . To guide the search point into the maximum, the direction of the search path has to be set. If the first search direction is found, P_0 is replaced by a new search point P_1 . In general, a rule has to be defined how to find search point P_{n+1} from P_n . Once this rule is set, the intensity values along the search path are compared and the maximum is assumed to be the focus point.

The rule for the search direction is illustrated in Fig. 4.11: It is assumed that the search starts in slice $k = 0$. If the search point lies in slice number k , the new search point is set in slice $k + 1$ with the option to be shifted laterally. The direction of the lateral shift is found by the comparison of the intensities: 9 directions are rated by summing up the pixels in these directions in the slices $k + 1$, $k + 2$ and $k + 3$ (only shown for two slices in Fig. 4.11). Summation is performed to give the algorithm a better robustness against noise. The new search point is shifted laterally toward the highest intensity. For each search point, the best summed intensity value and the search direction where the value is found are stored. At the end of the path in slice $k = Z - 1$, the search point P_{max} with the maximum summed intensity along the search path is selected and the focus point is identified taking into account the search direction at P_{max} as shown in Fig. 4.12.

To illustrate the procedure, Fig. 4.13 shows the focus found in a two-dimensional case for a single search point and a bright reflex in the real image: The left column shows the search strategy used for focus detection, the middle column shows a bright reflex in an

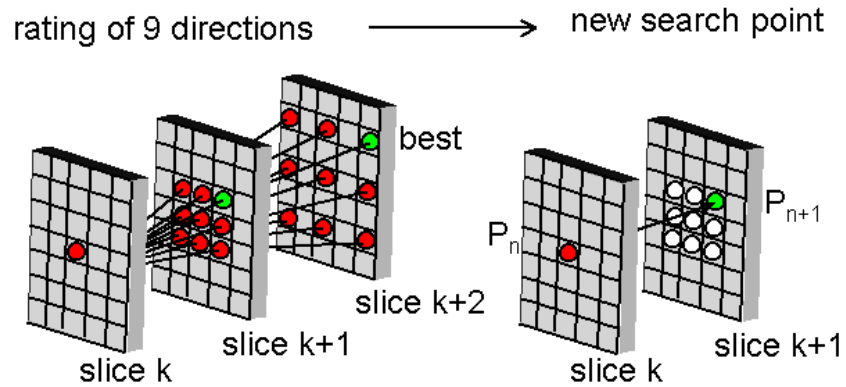


Figure 4.11: For each search point P_n , P_{n+1} is found by stepping towards maximum intensity.

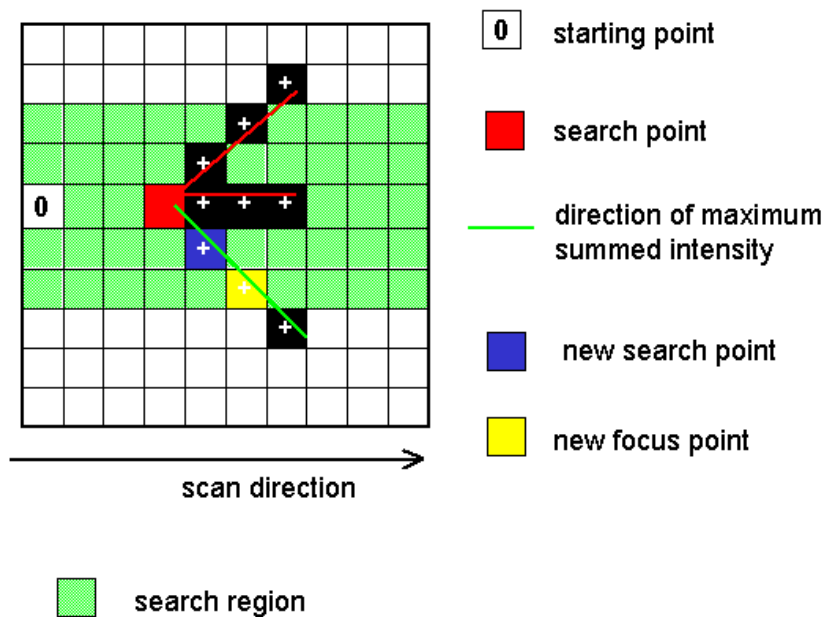


Figure 4.12: The direction of the highest intensity (green line) is detected for a search point (red pixel) by summing up three pixels. The new search point (blue pixel) is found by moving the old search point towards the direction of maximum intensity. The search area is restricted by a limitation of the maximum lateral shift of the search point with regard to the starting pixel (O).

axial image and the search path as red line. The green spot in the images indicates the focus point detected by the respective algorithm.

The right column shows a more realistic case: Not only one focus has to be found, a set of foci forms the surface. Then, not one search point is used, but each lateral position in slice $k = 0$ is chosen as starting point for a focus search. To avoid that these starting points are attracted by a single bright spot, the search space is restricted for each search point by a limit in the permitted lateral deviation from the starting point. This restriction is illustrated in Fig. 4.12 by the green field for permitted search points. Then, as shown in the right column of Fig. 4.13, a set of foci is detected by the algorithm (green points). Falsely detected focus points that appear in a straight maximum search are eliminated to a great extent.

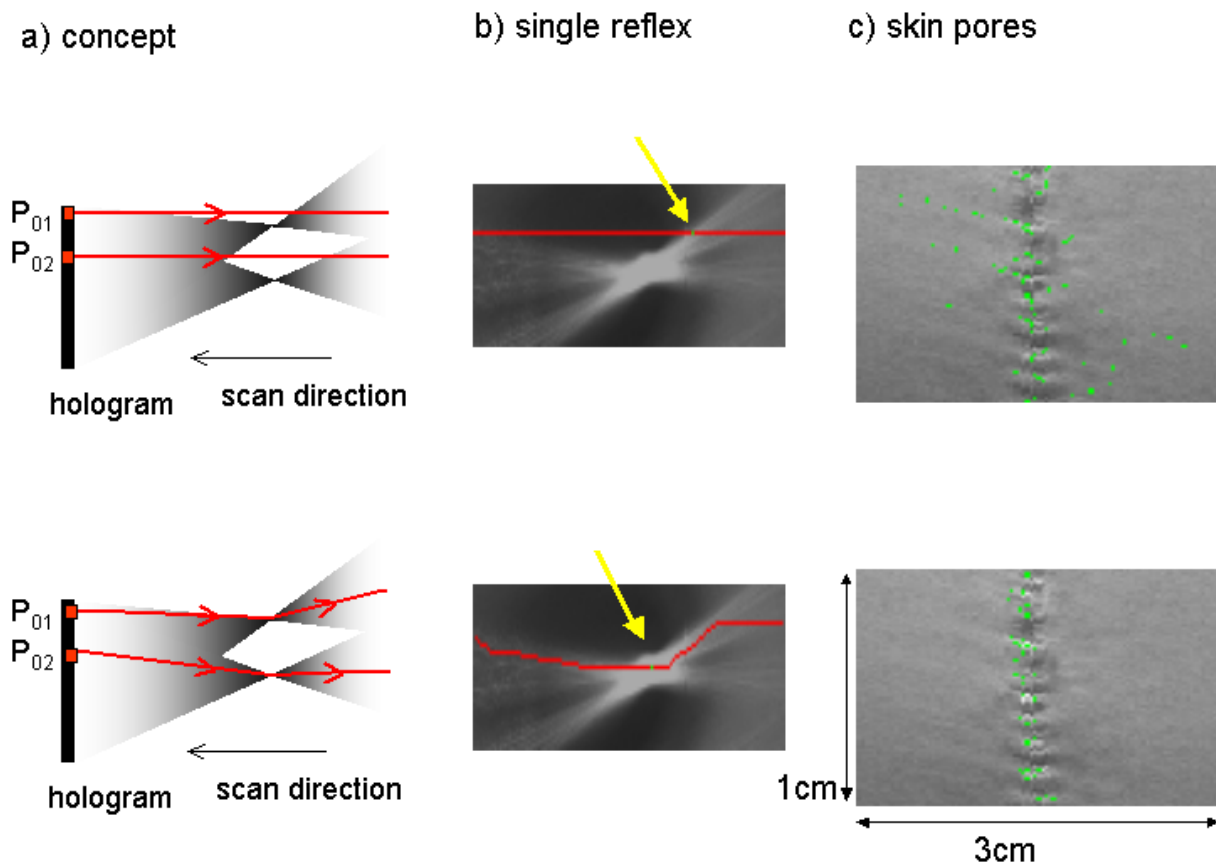


Figure 4.13: The influence of the maximum search strategy on the focus detection result: The left column (a) shows the search concept which is applied. The second row (b) shows the results of the search strategy for a single starting point and a single reflex. The yellow arrow points on the focus point that is found by the algorithm. Column (c) shows the results inserted in an axial image for a facial surface. The detected foci are indicated as green points. The left end pixel of each row is a starting point. The search area is limited to a lateral shift of two pixels from each starting point.

As consequence of selective focus detection, not every lateral coordinate (x, y) corresponds to a focus point $z_{max}(x, y)$ in the depth map. Those points in the depth map are set to zero. To construct a closed surface an interpolation step is necessary. If $z_{max}(x, y) = 0$, z_{max} is replaced by the average non-zero values in a pixel neighborhood as defined in Eq.4.8.

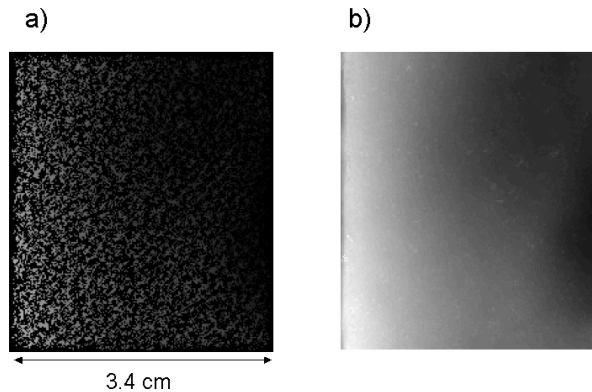


Figure 4.14: (a) Points in the gray scale depth map for which no reliable surface point has been detected are set to zero. (b) The missing points in the gray scale depth map are interpolated and replaced with an average value of surrounding valid points.

Surface points $z_{max}(x, y)$ identified by the focus detection algorithm are usually displayed as gray scale depth map or as color coded depth map. Surface points may be inserted into the original data sequence and appear as contour in each image of the stack. Fig. 4.15 shows a slice through the real image. In part (a) of the figure, the contour is inserted which is found by contrast maximization. Part (b) shows the surface contour from the axial search strategy described above. Obviously the effect of clustering described in section 4.3 leads to a deformation of the contour found by contrast maximization which disappears if the focus search is based on axial features. The absence of clustering also provides an efficient way to eliminate falsely detected image points by adapting a filter to the contour characteristics, which is presented below.

4.4.1 Contours

Falsely detected focus points due to image noise or caustic edges may be separated from the actual contour by counting the number $g(x, y)$ of detected surface points in a local $(m \times n)$ pixel neighborhood of the central pixel (x, y) . The ratio $d(x, y) = g(x, y)/(m \times n)$ is defined and a threshold value d_{thresh} is introduced. For each contour image, a surface point is neglected if $d(x, y) < d_{thresh}$, and replaced by the respective interpolation value. Fig. 4.16(b) shows reduced noise surrounding the contour as result of the procedure.

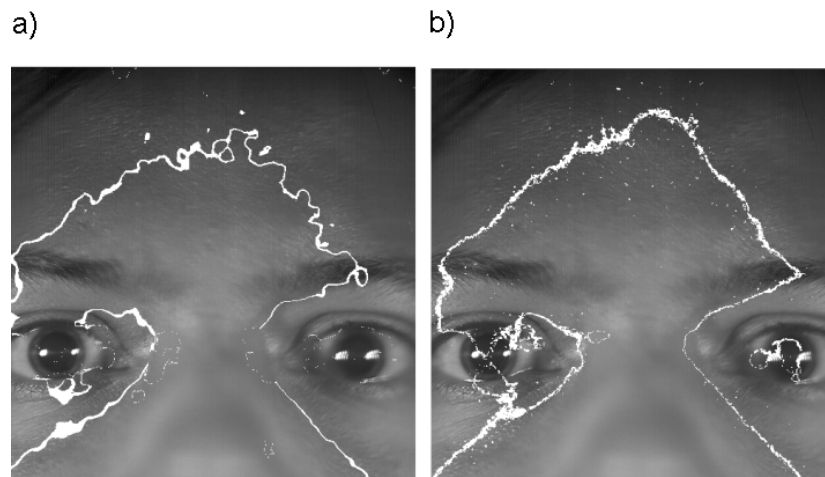


Figure 4.15: The surface contour is inserted in the original scan data. Part (a) shows the contour found by lateral contrast maximization, (b) shows the contour from axial focus detection.

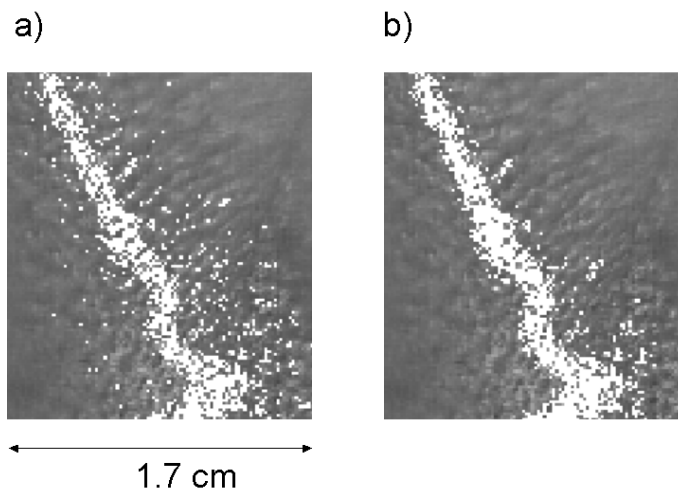


Figure 4.16: The surface contour is inserted in the original scan data. Part (a) shows the contour found by axial focus detection, (b) shows the same data filtered to form a sharp contour.

4.4.2 Symmetry

A second axial criterion is used to suppress artifacts from caustic edges in the focus detection process: Besides of being a local intensity maximum, a focus point is characterized by point symmetry of the intensity values to both sides of the focus point. Furthermore, a falsely detected focus point at a caustic edge displays asymmetry in the intensity values. A simple measure for point symmetry is the difference between the intensity values to both

sides of the alleged focus point along the search direction. This is depicted in Fig. 4.17: For a focus point (yellow field) the difference between the summed intensities to both sides of the point (gray fields) is calculated. If this value is small, the focus point displays high symmetry. A threshold value is chosen to discriminate points of low symmetry. This has the effect of a noise filter as is shown in Fig.4.18.

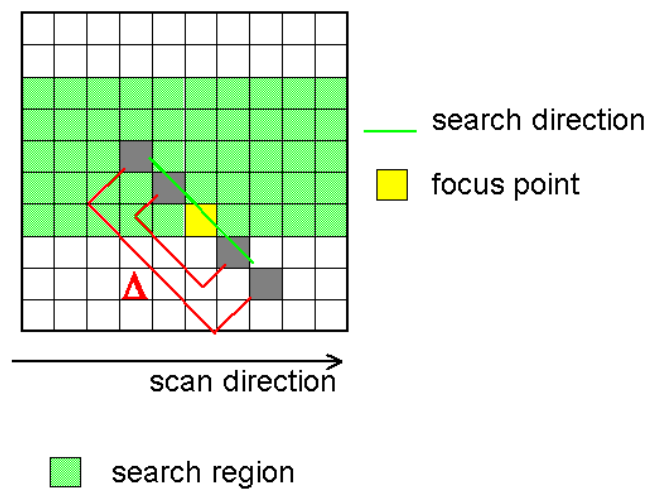


Figure 4.17: The search strategy is refined by calculating a symmetry measure for a possible focus point. High symmetry is detected, if the absolute value of the difference between the pixel values to both sides of the focus point is small.

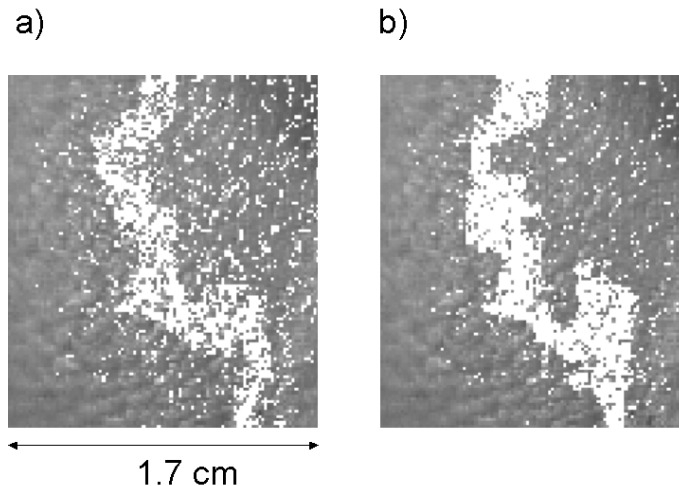


Figure 4.18: The surface contour is inserted in the original scan data. Part (a) shows the contour found axial focus detection, (b) shows the same data filtered by symmetry detection.

4.5 Results and discussion

The main drawback of contrast maximization methods is that they are based on a lateral image contrast calculated for a local pixel neighborhood incorporating a summation step. While, on the one hand, this leads to improved robustness against noise (see below), it also smears out bright image points into adjacent darker image regions. Clustering of contours found by these technique has been demonstrated above. Displaying the resulting surfaces reveals that the local image intensity distribution is transferred to the depth map. To illustrate this effect, the holographic images of two facial surfaces are evaluated. For the recording, the faces are illuminated by laser light that is modulated to either produce a stripe pattern on the face or a speckle pattern. The intensity distributions on the facial surface (gained from the model textures) are shown in Fig. 4.19 (a) and (d). The results from contrast maximization are shown in parts (b) and (e) as color coded depth map, and additionally as screenshots from a VRML model¹. Although the data is high pass filtered as first step for focus detection, the results have a characteristic depth modulation of the surfaces that corresponds to the projected intensity patterns. In comparison, the surfaces determined by axial focus detection appear smooth (see part (c) and (f) of the figure). To evaluate the improved smoothness of the data and to assure that it is not gained at the cost of image resolution, a test object is studied and discussed in section 4.5.2. The following section addresses the behavior of the proposed strategies at the presence of notable image noise.

¹The depth map can be visualized as an interactive 3d model, for instance, by writing an elevation grid using VRML (Virtual Reality Modeling Language)(see [Bon02] and [Gie03]).

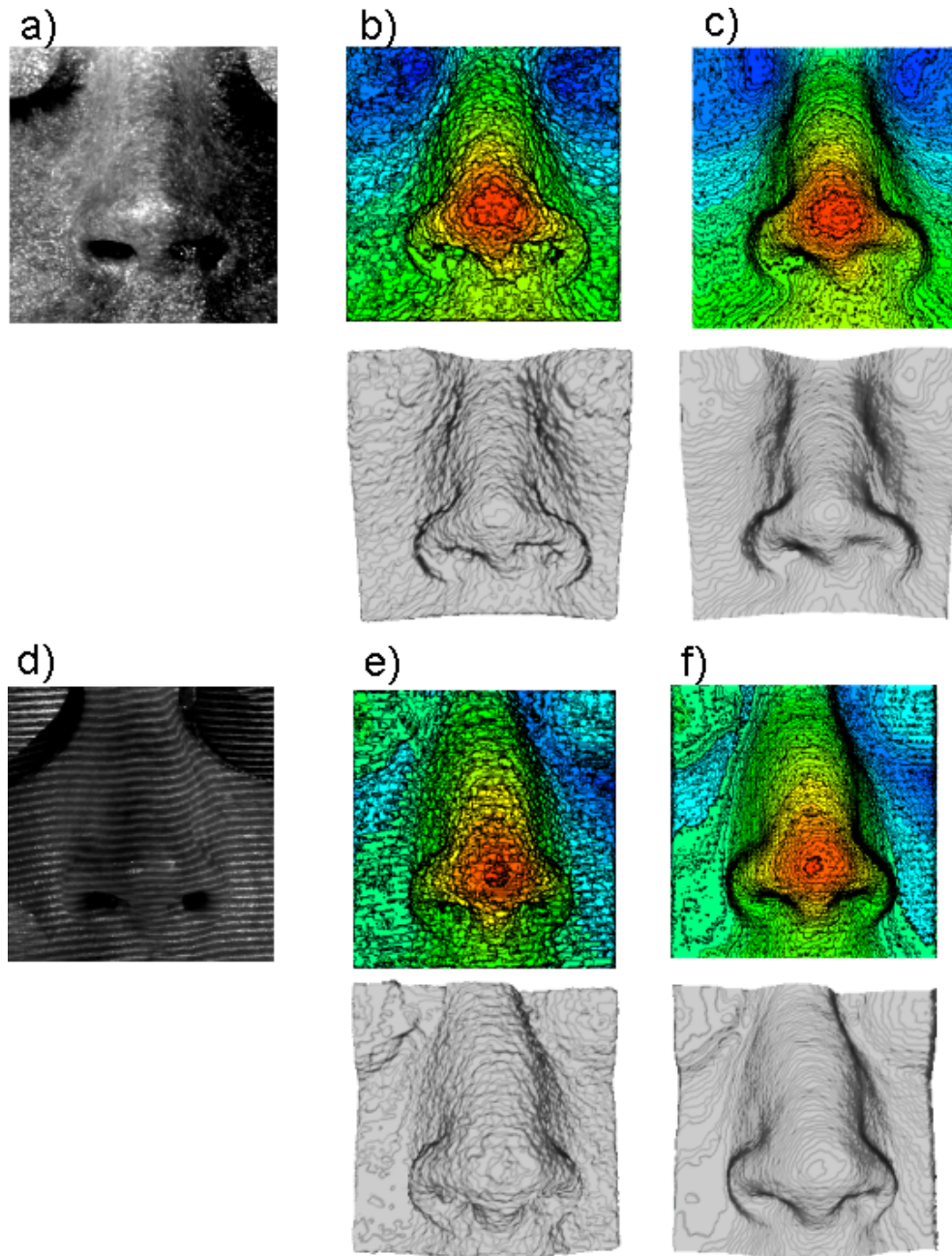


Figure 4.19: Surface recovery of noses from holograms of faces with two different projected intensity modulations: (a) and (d) show the texture maps, (b) and (e) the surface found by contrast maximization, (c) and (f) the result from axial focus localization. The surfaces are shown as color coded depth maps and as screenshots from the resulting 3d computer models.

4.5.1 Data noise

To investigate the differences of axial focus detection and contrast maximization concerning the robustness of the procedures, a noisy image sequence is evaluated. It displays a part of the face comprising an image volume of approximately $(3 \times 3 \times 2)\text{cm}^3$ digitized in a sequence

of 256 images, yielding an 8bit image as depth map. The displayed gray values between 0 and 255 in each lateral position correspond to the image slice that is identified as axial focus position in the scan sequence. The data is high pass filtered in a first step, according to Eq. 4.10. Then, a local average is calculated and maximized for surface localization. For comparison, the high pass filtered data is evaluated by using the axial focus search strategy described in the above section. The results are shown in Fig. 4.20. Part (a) of the figure shows the depth map gained by contrast maximization with a (5×5) pixel neighborhood. As the window size is increased to (25×25) pixels, the depth map reveals a closed surface as expected (see part (b) of the figure). The (5×5) pixel neighborhood obviously is too small to yield a reliable surface signal.

Axial focus detection is applied instead, and the search parameter of the tolerated lateral shift from the starting search point is set to ± 2 pixels. The detected surface is shown in Fig. 4.20(c). Further selection is performed by filtering the image contours and interpolation as described in sections 4.4 and 4.4.1. The result is shown in Fig. 4.20 (d). The histograms of the four images are depicted in Fig. 4.21: The continuous surface found in part (b) of Fig. 4.20 appears as broad peak around the gray value 185 in the histogram. It is shown as dark red curve in the upper set belonging to the right y axis. Clustering of the detected surface values under the influence of the local pixel neighborhood leads to distinct peaks in the histogram. The gray value distribution of Fig 4.20 (d) is shown as light red curve. It displays a comparable gray value spectrum without peak structure. The two noisy reconstructions from the (5×5) neighborhood and from axial focus detection are shown in the two lower curves, the darker curve belongs to part (a) of Fig. 4.20. This curve is characterized by a constant noise level to both sides of the central peak. More surface points in the realistic range of values determined by the red curves are found by the axial focus detection procedure shown in part (c). This result is explained by the axial averaging step in the detection process (see Fig. 4.12).

The option to choose a large window size in contrast maximization is a useful tool to compensate for image noise. In many situations the best result will therefore be obtained by roughly localizing the surface using contrast maximization with a large window size, and refining the surface by axial focus detection in a restricted image volume close to the initial guess.

4.5.2 Smoothness of the reconstructed surfaces

To evaluate the deviation of the detected surface from a smooth object with regard to the detection procedure, a test object with a square edge is studied. The aim is to reconstruct the plane surface as precise as possible for a surface considered as smooth within the scan parameters, whereas the sharp edge should not vary from the original data for more

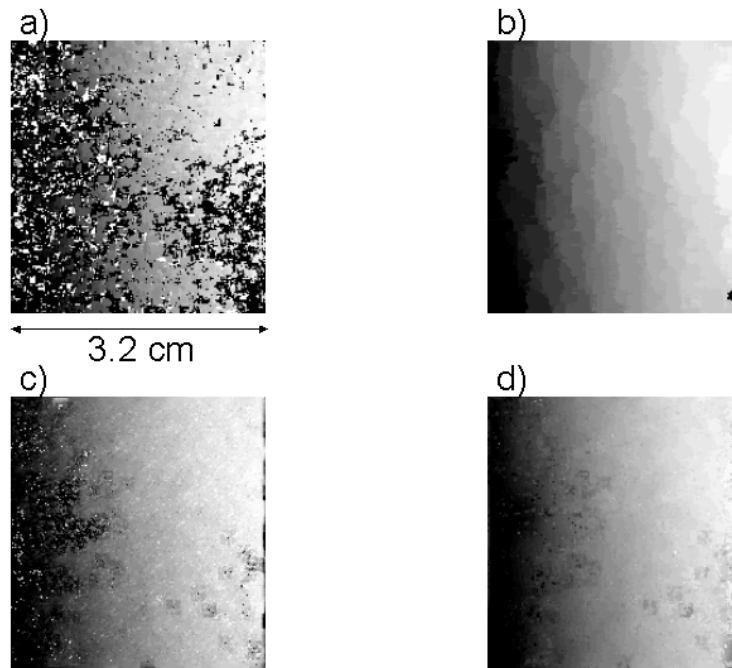


Figure 4.20: Surface depth maps from a noisy image volume found by (a) contrast maximization using a (5×5) pixel neighborhood; (b) contrast maximization using a (25×25) pixel neighborhood; (c) axial focus detection and (d) axial focus detection and contour selection.

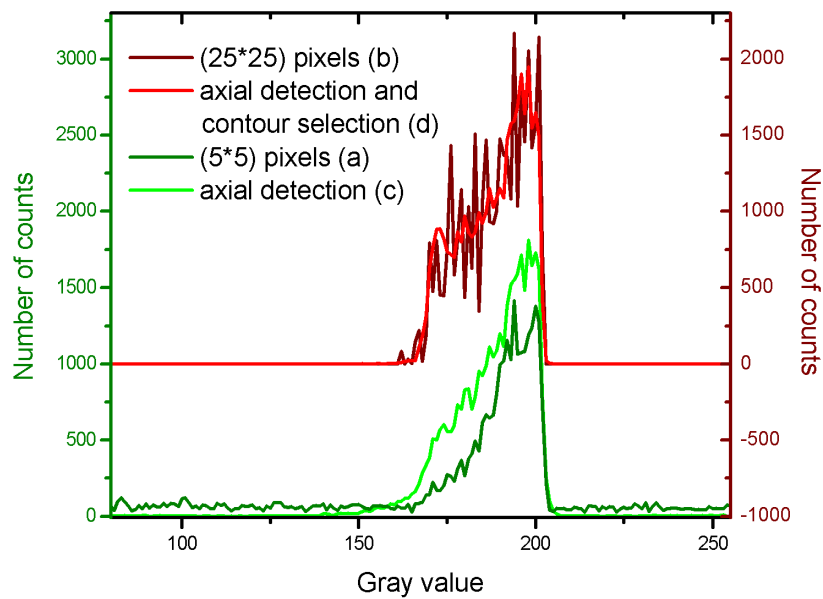


Figure 4.21: Histograms of the depth maps in Fig. 4.20. The upper red curves belong to the right axis. (See text for details.)

than the scanner step size. Because the surface of the object has no intrinsic contrast it is recorded with speckle illumination. The scan resolution of the real image is 300 dpi laterally ($85 \mu\text{m}$) and the axial step size is $203 \mu\text{m}$. The first step for data processing is subsequent vertical and horizontal high pass filtering with a local pixel neighborhood of 20 pixels using the difference measure introduced in Eq.4.10. Contrast maximization is performed by calculating a local average over (11×11) pixels. Based on the surface found by contrast maximization, the surface recovery is refined by axial focus detection with a lateral tolerance of \pm one pixel and subsequent contour selection by median filtering of the resulting contours detected in the image stack. Both results were filtered with a median filter with the smallest possible filter mask radius of one pixel after processing. The resulting height maps are displayed as 3d models in the VRML format. Screenshots are shown in Fig. 4.22 (a) and (b).

The angle formed by the two smooth surfaces is 90 degrees. An ideal object surface is

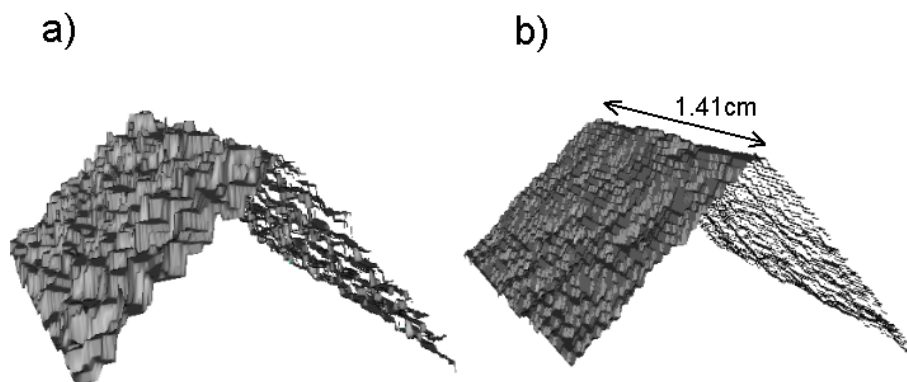


Figure 4.22: A test object of two smooth surfaces forming a sharp 90 degree angle is reconstructed from a hologram. The shape (a) results from contrast maximization, (b) from axial focus detection.

fitted to the reconstructions. The difference between the ideal object surface and the reconstructed surfaces is depicted in gray scale values for both contrast maximization and axial focus detection in Fig. 4.23(a) and (b). The contrast maximization method leads to a stronger deviation. The deviation values of 0-6 slices (0.203 to 1.218 mm of deviation) are depicted as gray values from black (corresponds to 0) to white (6 slices deviation). The average deviation of the values for the contrast maximization method is 1.282 units, corresponding to a mean deviation of $260 \mu\text{m}$ from the expected surface. The mean deviation for the images gained by axial focus detection is 0.572 units, corresponding to a mean deviation of $116 \mu\text{m}$ from the ideal surface area. The maximum deviation is 6 units (1.218 mm) for contrast maximization and 3 units ($0.609 \mu\text{m}$) for refined surface determination.

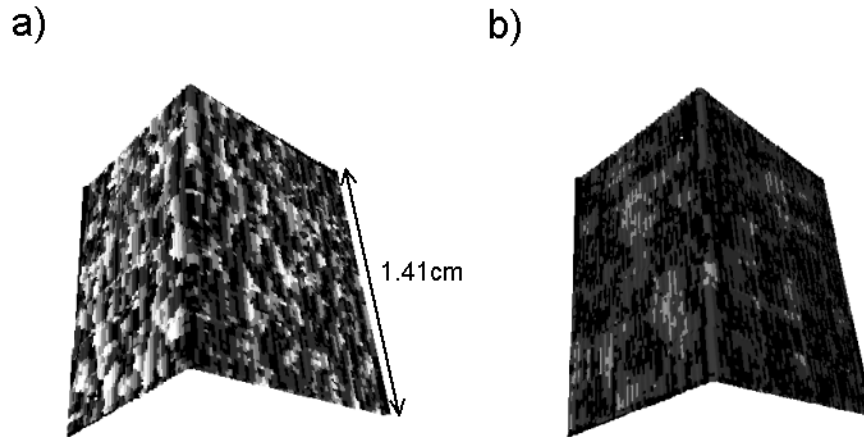


Figure 4.23: The test object is simulated, and the deviations of the reconstructions are depicted as texture maps (a) for contrast maximization, (b) for axial focus detection. The displayed values range from zero (black) to 1.218 mm (white)

To assure that the improved surface smoothness is not caused at the expense of image resolution, the sharp edge of the test object is examined in both reconstructions. To compensate for local variations along the reconstructed surface a profile of the edge is depicted after averaging over 25 cuts through the depth map. The profile is shown for both data sets in Fig. 4.24: The blue line belongs to the profile found by contrast maximization (it is shifted for better visibility of both curves). The red line stems from axial focus detection. Obviously, the sharp edge is contained better in the axial detection profile despite the increased smoothness of the model. To determine the deviation of the sharp edge from the ideal object, a linear fit is added in Fig. 4.25. The distance between the crossing of the two fitted lines and the actual measured edge (taken as minimum of the red curve) is $170 \mu\text{m}$, which is just within the step size of the scanning sequence.

4.5.3 Textured facial models

The main purpose of the presented system is facial measurement. The facial surface is gained by focus detection in the digitized real image of a portrait hologram. The result is a depth map $z(x, y)$. An example is shown in Fig. 4.26(a) as color coded image. The intensity information $a_{max}^z(x, y)$ is a pixel matching texture map that intrinsically belongs to the surface without an intermediate registration step. The texture map is a gray scale image. Capturing the real image by a color sensitive detector only makes sense when using color holography. A single color is added to the gray scale texture manually to give a more realistic impression of the face. Fig. 4.27 shows several views of a textured 3d model retrieved from a portrait hologram.

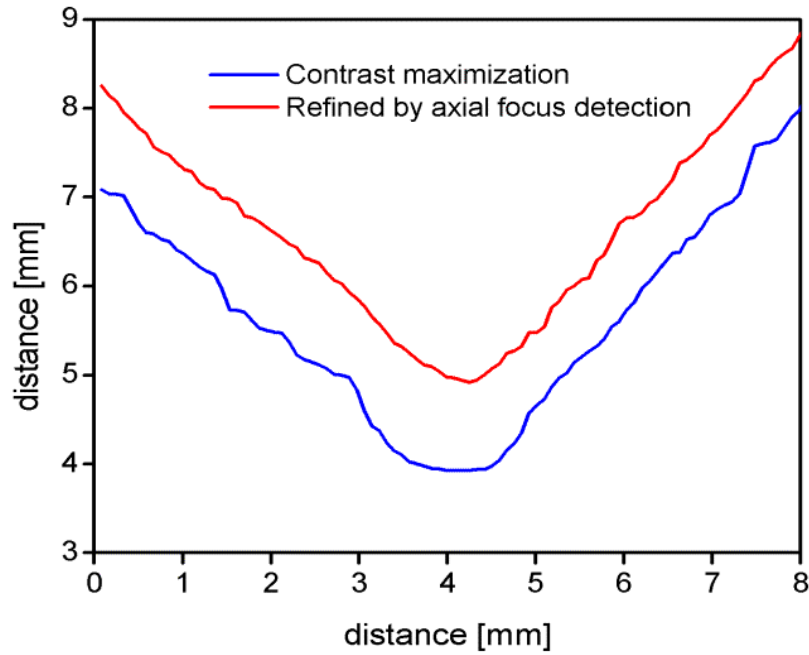


Figure 4.24: Depth profile of a sharp edge from contrast maximization (blue line) and from axial focus detection (red line). (The blue curve is shifted for easier comparison.)

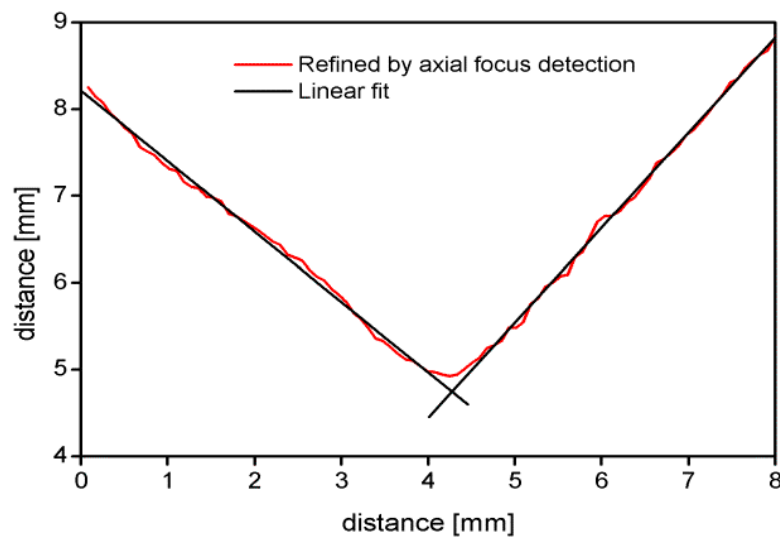


Figure 4.25: Red line: Reconstructed depth profile; Black lines: Linear fits to both sides of the profile.

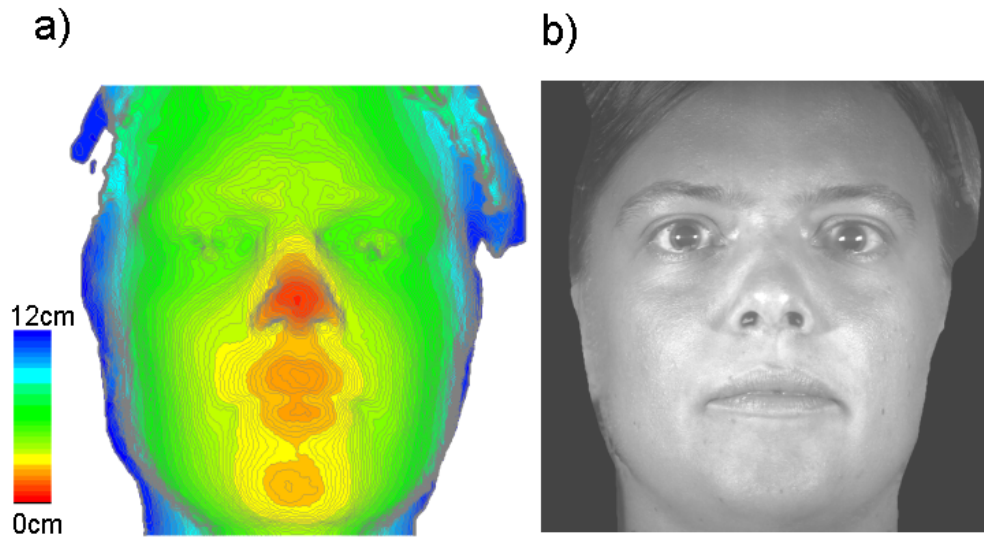


Figure 4.26: The result of surface detection in the real image is a depth map, shown as color coded image in part (a). The intensity information in the real image at the object position yields the texture map (b).

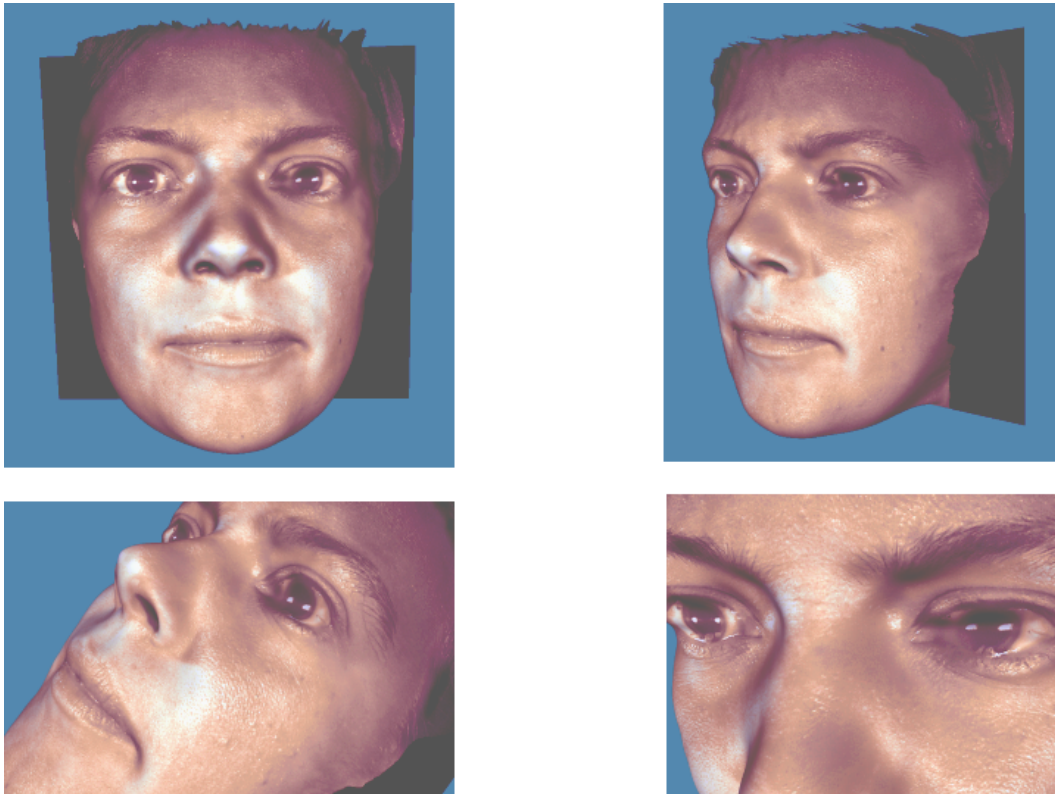


Figure 4.27: Several views of a textured three-dimensional computer model retrieved from a portrait hologram.

4.5.4 Mirror images

In order to extend the visual field of the holographic data, as described in section 3.3, mirrors are added to the set-up. The volume is digitized with several scans, not only due to the limited area covered by the CMOS scanner, but also to adjust the scan axis to coincide with the optical axis of the respective mirror view. The difficulty in the evaluation of mirror images originates from the limited diffraction efficiency of the hologram and the intensity loss at the mirrors. Consequently, the mirror views appear darker than the real image of a solely frontal recording. Besides this, the laser intensity of the object illumination beam decreases to the sides of the face, an intensity loss from the front to the side view appears, and thus the contrast within the side views decreases. The quality of the data of the side views has to be the same as for the frontal view. For that purpose the data of the side views is at first evaluated by contrast maximization with a sufficiently large pixel neighborhood in the summation step to yield a closed surface. In the proximity of this surface the focus search is refined by axial focus detection for a reconstruction of improved evenness and accuracy. The results of this procedure are presented in Fig. 4.28: Three textured computer models are retrieved from a single hologram. Despite the increased requirements of the evaluation procedure this method has a crucial advantage compared to three recordings of the face taken successively: The three views of the front and the sides of the face are taken at the same time, and the three surfaces gained from this recording are unaffected by movement artifacts caused by a change of the facial expression in between the exposures. Due to the overlap of the three facial models, registration of the facial views by 3d standard software not only extends the view of the imaging system, but also, by combination of the data, may improve the resolution of the merged point clouds.

As shown in section 3.3.3, the arrangement of the mirrors can be extended by a third mirror to illuminate the hologram from the side facing away from the holographic camera. Then three views of the hologram (the frontal view and two mirror views) allow to image an angle of 360 degrees of the object. To illustrate this, a polystyrene ball is provided with a tape measure surrounding the object. Three views from a single hologram are evaluated, and the texture information of the evaluation is used in order to identify the individual sections of the tape measure, which shows that indeed a panoramic reconstruction of the model is possible (see Fig. 4.29). It is also conceivable to use this extended mirror set-up to generate an improved intensity distribution for the recording of facial side views.

4.6 Summary

Digital image processing is applied to high resolution projection images of the holographic real image. The aim is to detect bright spots in the real image volume to recover the

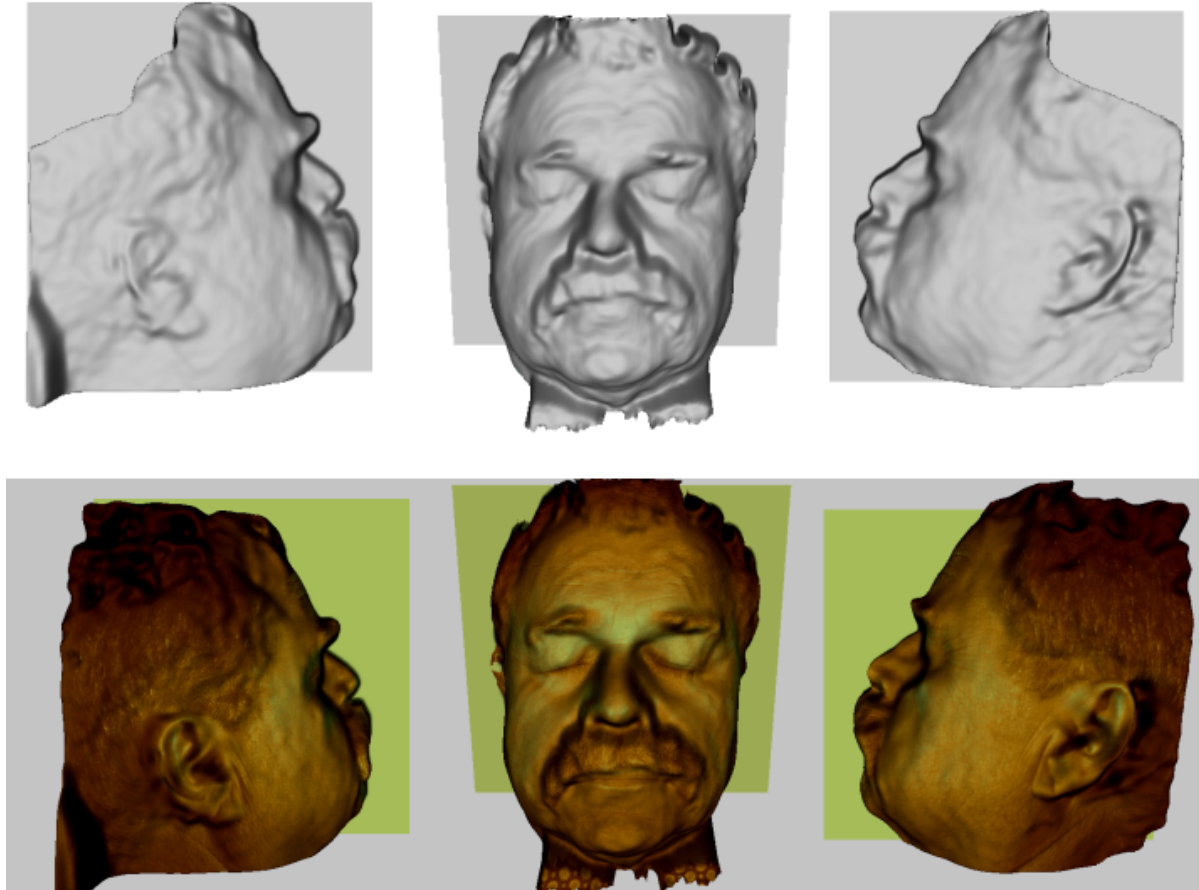


Figure 4.28: A portrait hologram is recorded and evaluated including two mirror views. The upper row shows the recovered shapes as interactive 3d models, the lower row shows the facial surface with additional texture information.

shape of the object recorded in the hologram. The focus geometry is discussed with regard to axial and lateral focus features. Spatial high pass filtering is found to be an efficient way to deblur image sequences as first data processing step, which works faster than deconvolution techniques or Fourier filtering. The standard method for shape-from-focus techniques is contrast maximization, which is tested and analyzed concerning its merit for the holographic application. The positive aspect of contrast maximization is its great robustness against image noise. Still, a systematic error inherent with this detection scheme is illustrated: The intensity distribution on the object surface is transferred to an unwanted depth modulation on the resulting surface model. To eliminate this effect a focus search strategy is developed that relies on axial focus features. The results of both strategies are compared with regard to their robustness against image noise, the smoothness of the reconstructed surfaces and their resolution.

Textured facial models from eye-safe hologram recordings are presented, as well as facial computer models from mirror images. The general option for single shot panoramic

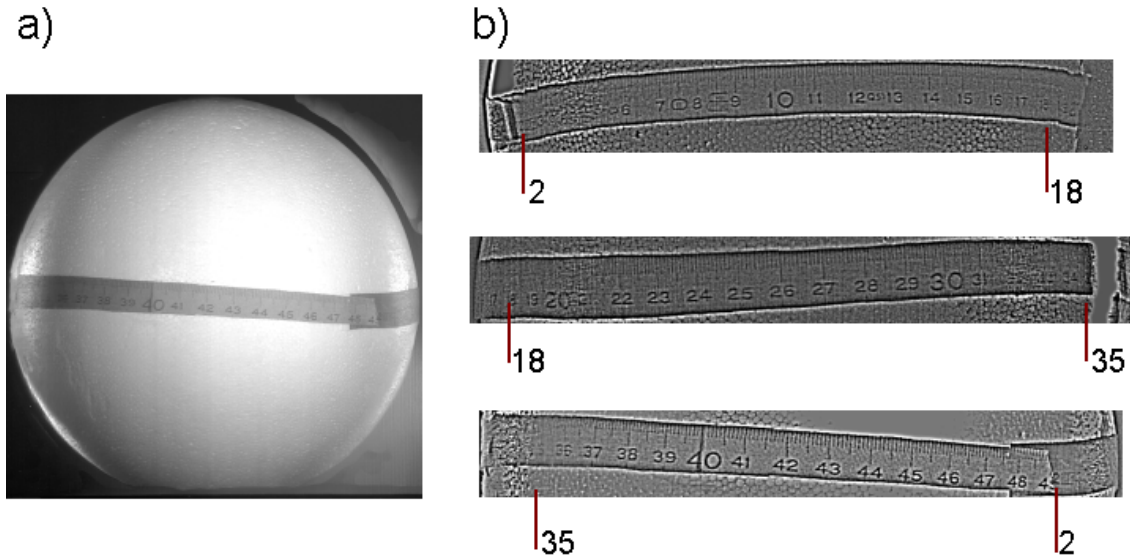


Figure 4.29: A panoramic image of an object is retrieved from a single hologram by evaluating a frontal view and two mirror views. Part (a) shows the texture map of a single mirror image, (b) shows sections of the attached measure tape as seen in the frontal and the mirror view.

imaging is demonstrated with a test object.

It is shown in this chapter that facial surface information may indeed be extracted from sectional images of portrait holograms without the need for pattern projection. Pattern projection is still a valuable tool to image smooth surfaces, particularly in combination with axial focus detection (see section 4.5.2). But the option to use the natural skin structure for focus detection in the real image has significant advantages in the medical context: Diffuser plates can be employed to illuminate the face, so the patient may be recorded in an eye-safe manner. Furthermore, the texture map gained from these holograms has a unique quality and matches the surface accurately. This is essential for a high recognizability of a facial model. The texture also provides relevant information to the surgeon for navigated surgery. In conclusion, the presented system exclusively features the combination of ultrafast surface recording, high resolution surface digitization and intrinsic texture mapping, which are the key to medical facial imaging. The combination of all these aspects cannot be found in laser scanning, photogrammetry or fringe projection systems.

In the next chapter, selected applications of the holographic surface measurement system are presented.

Chapter 5

Fields of applications

The main focus of the applications of holographic facial imaging is reconstructive surgery and forensic medicine. In this field, the primary issue is to set up facilities that allow for surveying of a large number of patients in a routine that can be handled by clinic staff. Section 5.1 summarizes the efforts towards such a routine and gives an example of a medical application.

From the master hologram recorded with the holographic camera, a computer model of the recorded object may be extracted. Moreover, a daylight copy of the master hologram can be recorded. These holograms do not require a laser to visualize the recording but may be viewed with an extended white light source which makes them suitable for exhibitions. The combination of an interactive computer model and the genuine three-dimensional impression from a daylight hologram is used for the documentation of cultural heritage and for the presentation of archaeological objects in cases where the original object is not accessible. An example will be shown in section 5.2.

In forensic science, facial reconstructions of skulls are needed to identify dead persons. Several facial reconstruction techniques are commonly employed. Holography may be used in this context to evaluate the results and to establish an accurate three-dimensional automated facial reconstruction process based on a holographic facial data base. A first contribution of holographic facial measurement in forensic science is presented in section 5.3.

5.1 Medical facial measurement

To provide service to clinics on a larger scale, it is made use of the fact that the recording and the read-out of the hologram work independently. The hologram read-out unit can be set up at a stationary laboratory. The recording is performed with a mobile system in a clinical environment. Such mobile holographic camera was designed in cooperation with

the company Geola Technologies Ltd., and installed at the university hospital in Basel for the implementation of a facial measurement routine at the department for maxillo-facial surgery (see Fig.5.1). A central aspect of a recording procedure is stable quality of the resulting holograms. This requires a simple procedure and automation to the greatest possible extent. The automation of the chemical processing of the hologram by using a development machine (see section 3.4) serves this concept and helps to make the results of the hologram recording independent of the person in charge.



Figure 5.1: The latest generation of holographic cameras is mobile: It fits into boxes that may be transported in a car. The hologram plate is put behind a shutter, so the recording works at any ambient light condition.

Fig. 5.2 shows an application of holographic data, which was done in cooperation with Prof. Dr. Dr. Fritzemeier (University Hospital Düsseldorf). It displays a Rapid Prototyping (RP) model manufactured by the *Rapid Prototyping* group at the research center caesar (center of advanced European studies and research) in Bonn, that visualizes the process of the adaption of an epithesis to a patient's face. Part (a) of the figure shows the RP model of the patient's face which was manufactured according to a computer model from a hologram. The facial defect is then compensated virtually by performing a mirror operation on the facial surface that projects the intact side of the face onto the defect. The difference volume is then used as basis for the adaption of an epithesis to the face. The difference volume which is added to the face is shown in part (b) of the figure as light red inset to the facial model.

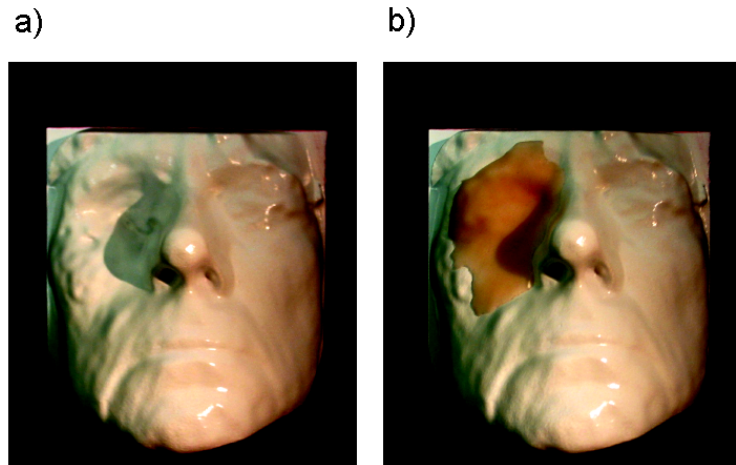


Figure 5.2: (a) RP model of a patient's face. Based on this model an epithesis is adapted to the facial surface which is shown in part (b). (The RP model was fabricated by the *Rapid Prototyping Group* at the research center *caesar*)

5.2 Imaging cultural heritage

Holography as means for the documentation of cultural heritage offers great detail of the replayed object or scene in the real image as well as the option to observe the virtual image three-dimensionally. Image plane copies of a hologram can be recorded as volume holograms. The hologram then acts as a reflecting grating and the image is reconstructed under white light illumination. Such a daylight copy gives a realistic impression of the object which is far more spectacular than a photograph, so it may be distributed and exhibited instead of the object itself. This has been demonstrated for the imaging of the bog body of Husbäke [FBG+03], [Nat02], [Sci02]. Mirrors can be used to record lying objects, and mobile holography makes it unnecessary to move sensitive objects from their positions. Scenes at excavation sites may be recorded with the mobile holography camera.

Using the texture based approach allows to generate computer models including texture information. This provides a fast and cheap method to gain data which can, for example, be used as basis for the fabrication of a replica of the object. Using the mobile holography system makes the transportation of the object unnecessary. Therefore, holography is a valuable imaging technique besides photography and computer tomography.

Holographic imaging of the Windeby child bog body is presented as selected application. The ongoing examination and interpretation of the burial circumstances keep the mummy in the news and confirms its status as one of the most famous bog bodies from northern Germany. The bog body is dated to the Iron Age, approximately 500 B.C. to A.D. 800.

To give an idea of the controversial discussion that is still going on about this bog body, its history is summarized in brief: The bog body was found in the year 1952 near a place called Windeby, and is named Windeby I, to differ it from a second bog body the was found nearby (Windeby II). It is exhibited in the *Stiftung Schleswig-Holsteinische Museen Schloss Gottorf* in Schleswig in northern Germany as shown in 5.3 (taken from the museum's webpage *www.schloss-gottorf.de*). The skull of the bog body is separated from the shown skin fragments.

The bog body was found at the edge of a bog and especially the face and hand of the body were in a good state of preservation. It was concluded to be most likely the body of a girl at the age of 13-14 years. Therefore "Windeby girl" became the common name of the bog body. The Windeby child was probably not drowned in the bog, but was buried in an inhumation grave. The grave also contained a birch stick, stones and sherds of pottery. A band covering the eyes of the child, close cropped hair on one side of the skull and the posture of the right arm led to the theory of discriminating treatment of the Windeby child and death punishment for committing adultery. Meanwhile, this theory had been revised [Geb79]: It has been emphasized that the burial circumstances can be interpreted in many ways. For instance, the theory of death punishment is in contradiction to the grave artifacts (pottery) that rather point to a burial which displays evidence of affection towards the subject. The other characteristics of the burial can be ascribed to practices of popular belief, for example against return of the undead.

In the course of a re-examination of six bog bodies of the Museum Schloss Gottorf [GR05] the sexing of the body is under renewed debate: It is suggested that the Windeby child bog body might actually belong to a boy.

The form of the skull, in particular, the strongly developed supraorbital ridges gave a first impulse for the new sexing of the bog body. As is shown Fig. 5.4, this can be demonstrated using the three-dimensional information about the outer appearance of the front of the skull that was extracted from the hologram of the bog body's skull.

Testing of different imaging techniques of the skull is a central part of the re-examination of the bog body. In this context, a high resolution CT was also made of the Windeby child skull. The sex determination is now subject to current examination using DNA analysis.

5.3 Forensic facial reconstruction

Three-dimensional facial reconstruction from a skull is a standard method in criminalistic work. Several reconstruction techniques are used that differ substantially with regard to the data used for the reconstruction and the reconstruction procedure. An overview of these methods is given for in [Wil04]. The contribution of holographic facial measurement to this



Figure 5.3: The Windeby child bog body (taken from *www.schloss-gottorf.de*)



Figure 5.4: The skull of the Windeby child bog body: (a) photograph, (b) computer model from holography

field is to provide precise soft tissue data. A data base of facial soft tissue in combination with skull data from computer tomography may be the basis for three-dimensional facial reconstructions on a highly automated level. Furthermore, facial measurement is used to study the existing facial reconstruction methods and compare their results. Questions that are to be answered are in how far the anatomical structure of the facial soft tissue has to be considered, whether digital methods can compete with manual reconstructions, and in how far the data base of the reconstruction methods influences the result. A first step towards

this direction is taken by a project carried out in cooperation with the *Academy of Visual Arts Maastricht / Faculty of Medicine, Maastricht University* and Prof. Wittwer-Backofen of the *Department of Human Genetics and Anthropology of the University of Freiburg*.

The face of a living human person was reconstructed from skull data gained by Computer Tomography. Different methods were used for the facial reconstruction. The face of the person was recorded with holography to allow a comparison of these methods with regard to the appearance of the actual person.

A high resolution Computer Tomography (CT) of a skull, originally made for medical necessity, was provided by Prof. Dr.Dr. H.-F. Zeilhofer (University Hospital Basel, Switzerland) (see Fig. 5.5). The patient agreed to be part of the project, and a hologram of the person was recorded, as well as photographs. The skull was fabricated from the CT data by using a 3D printing technique. This was done by the Rapid Prototyping group at the caesar foundation in Bonn. Henrike Stratomeier, a student at the *Academy of Visual Arts Maastricht / Faculty of Medicine, Maastricht University*, received the skull model and wrote her master thesis on the facial reconstruction of the skull by several methods [Stred]. A drawing method, the *Gerassimov method* and two-dimensional computer superposition were applied. These methods are now reviewed in brief.

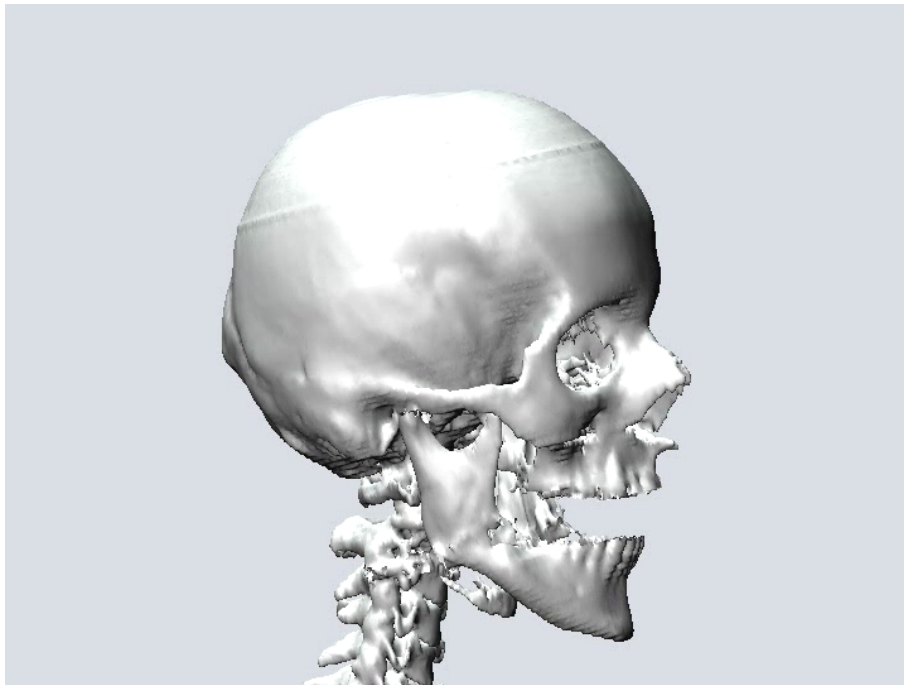


Figure 5.5: This skull data, gained from computer tomography, is the basis for facial reconstruction of a real living person.

According to the *Gerassimov method*, the reconstruction is based on an anatomical

model of the face. Muscles, fat tissue and skin are added in that order. In contrast, in other methods, soft tissue is added to the skull without reference to the anatomical substructure. Markers are placed on the skull and soft tissue is added at the marker positions according to data that determines the thickness of the soft tissue at these markers depending on further information of the person that is reconstructed (age, sex, constitution and ethnic origin). The method is carried out using a model of the skull or the skull itself. The face is then modeled by adding plasticine.

To make facial reconstruction more cost-effective and faster, two-dimensional computer superposition is an alternative: A digital photograph of the skull is superimposed with digital photographs of faces that are chosen according to the additional information that is known about the person belonging to the skull. A data bank provides whole faces and facial parts in many variations. The positions are chosen according to the skull geometry, and the selected image parts are manipulated digitally to adjust them to the skull contours. The age of the person may be varied by adding wrinkles or smoothing the digital images. The software *ISIS Phantom Professional* for two-dimensional digital facial reconstruction was used.

Two-dimensional facial reconstruction can also be performed manually by means of drawing. For the drawing reconstruction H. Stratomeier prepared the skull with 34 markers following a method and data base by Helmer [R.P84]. The drawing reconstruction is then made based on photographs of the skull.

For a more detailed description of the procedures and the results the reader is referred to the master thesis of H. Stratomeier [Stred].

The results of the reconstructions are shown in Fig. 5.6 (a)-(c). Part (d) shows a screenshot of the facial model gained from holographic facial measurement. A photography of the real person is shown Fig. 5.7.

The results of the reconstructions that are to be compared stem from two-dimensional methods and a three-dimensional method. This makes a quantitative comparison difficult, so the presented data is in a first step used for a qualitative evaluation of the results which is based on a subjective estimation of the recognizability of the real person from the reconstructed faces. Developing adequate criteria for the objective comparison for the recognizability exceeds the scope of this work, particularly as such a comparison requires the incorporation a larger number of test persons. Nevertheless, this project demonstrates that the reconstruction results from different methods differ strongly, and holographic facial data is generally suitable for a valuing comparison of reconstruction results.

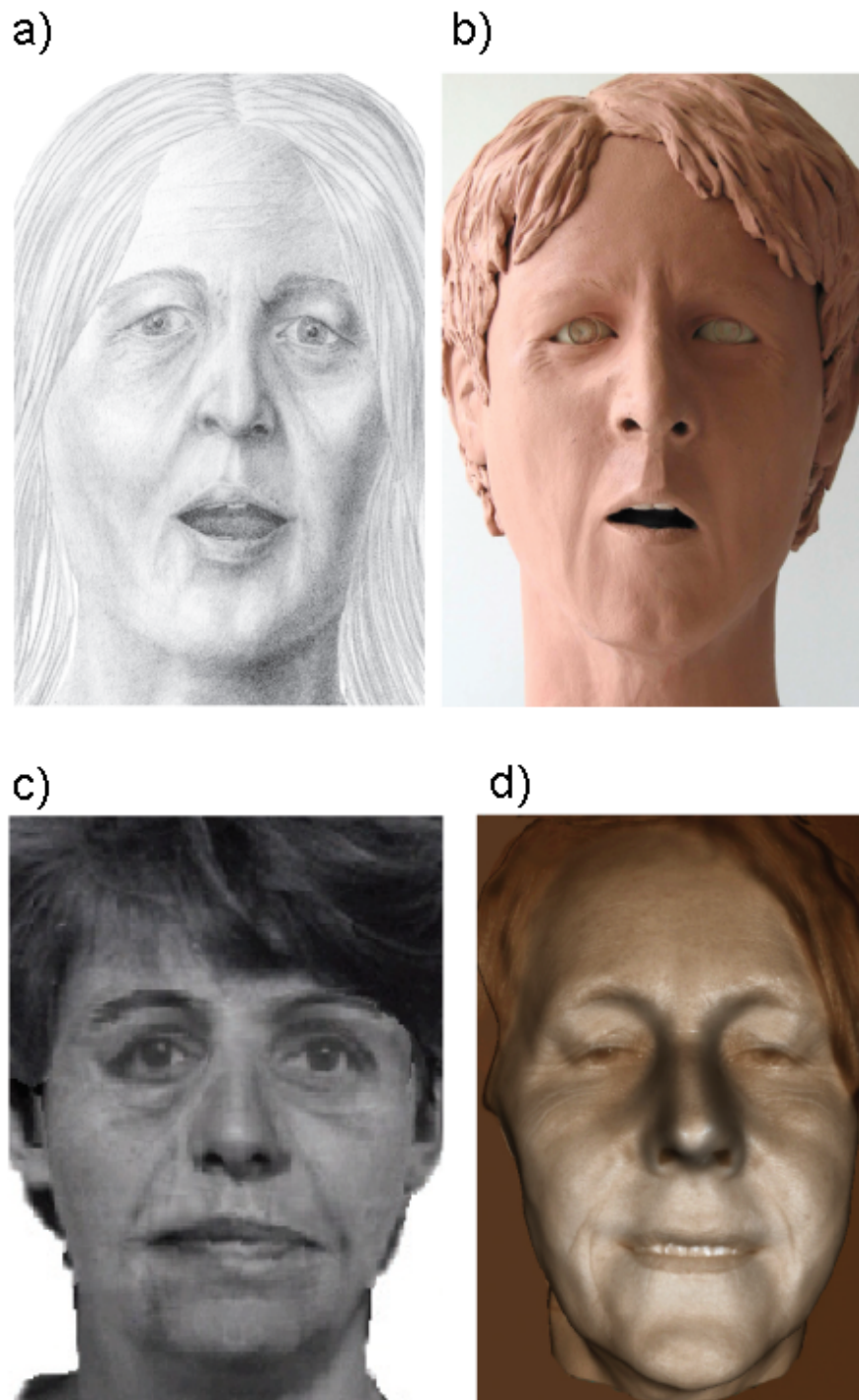


Figure 5.6: The face of the person is reconstructed (a) using the drawing method, (b) using the Gerassimov method and (c) using 2d computer superposition. Part (d) show the 3d facial computer model from a portrait hologram.

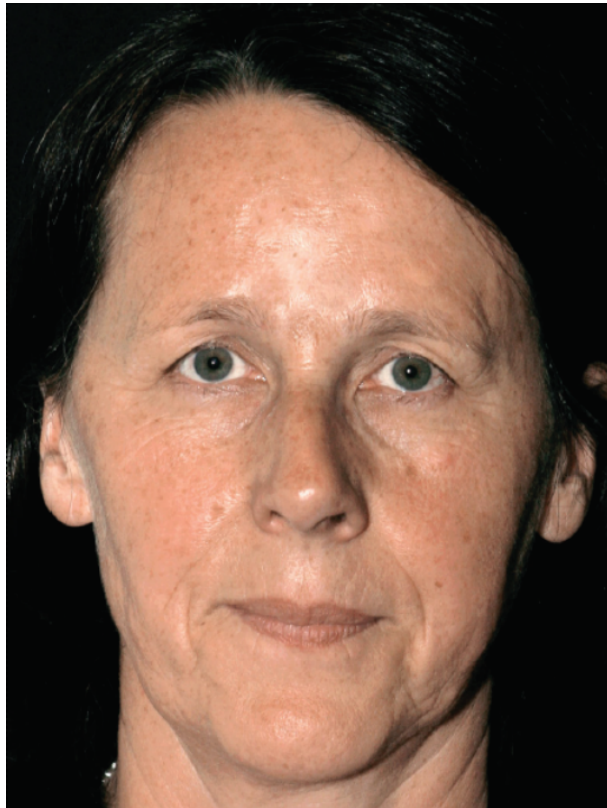


Figure 5.7: Photography of the real person

Chapter 6

Summary

The process for three-dimensional facial measurement from eye-safe portrait holograms is introduced by combining optical and numerical hologram processing. In preceding work [Bon02], [Gie03], [The03], facial measurement based on analogue pulsed holography was presented using a high contrast pattern that was projected onto the face of a person. The high contrast was achieved using stripe projection or speckle projection which both led to an illumination of the face with a laser intensity that exceeds the exposure limit for eye-safe recordings by two orders of magnitude. Eye-safe hologram recordings were discussed in [Gie03] and [The03] but no computer model or texture map from such a recording could be presented because the results were of minor quality.

The importance of eye-safety for recordings in a clinical environment is obvious: The convenience for the patient and the operator of the recording system is improved, because the positioning and the alignment of the system is easier, and it is unnecessary to wear protective goggles during the recording. Furthermore, the recognizability of the facial models greatly increases for eye-safe recordings because the intensity distribution from the hologram of a face without pattern projection serves as high resolution pixel-matching texture.

To make the holographic facial measurement system work eye-safely, several aspects of the procedure have been identified as sources of noise or unwanted artifacts. They impede holographic facial measurement based on the natural contrast from skin pores in the real image, and the respective processing steps have been improved.

An optical imaging system is presented that allows to reconstruct and digitize the real image of a large-scene hologram by projection imaging with a lateral image resolution $< 100 \mu\text{m}$. If a portrait hologram is read out optically and digitized at this image resolution, skin pores are displayed in the digitized real image volume. The image contrast of these skin pores is rather low, so special care has to be taken to reduce noise sources in the digitization step, which is accomplished by scanning the real image with a CMOS line scanner. Spatial filtering is used to deblur the images and remove image distortions introduced by the scan

procedure. To extract the shape of the object surface that is recorded holographically, focus detection in a set of sectional images of the real image is carried out. A standard approach to the shape-from-focus problem is contrast maximization in a local pixel window. The results of such a procedure are analyzed and compared to a newly developed focus detection method based on axial focus features. It is concluded that contrast maximization with a large pixel window yields a good first guess of the surface shape due to a good robustness against image noise, which increases with the window size. Improvement of the detected surface is then achieved by refining the search strategy using axial focus features. The results of this procedure are precisely textured computer models of frontal views of facial surfaces which may be supplemented by mirror views in the set-up. Side views of a sitting person are then recorded in a single shot hologram, and panoramic recordings are possible. Additionally, the concept of object localization from the hologram by using an interferometric signal of the original reference beam and the virtual image of the reference beam is investigated experimentally.

Examples of applications of holographic facial models are given from the fields of medical, forensic and archaeological imaging. The adaption of an epithesis based on holographic measurement is presented, and a set-up consisting of a mobile holographic camera with automated hologram development and a stationary reconstruction unit is introduced which allows for recordings in a clinical environment.

For archaeological imaging both display holograms and textured computer models are provided by processing the master hologram. Imaging of the Windeby child bog body is shown as example.

The feasibility of the holographic system to contribute to the field of facial reconstructions in forensic science is demonstrated. A facial reconstruction of a real living person was made based on CT data. Several reconstruction techniques were applied by H. Stratomeier ([[Stred](#)]) and holographic facial imaging of the real living person is used to compare the reconstruction results with regard to the provided recognizability.

In conclusion, the presented surface measurement system provides ultra-fast holographic recording and high resolution digital reconstruction of facial surfaces based on the natural image contrast from skin pores. Furthermore, the system now works calibration free without scaling lenses in the recording and the reconstruction unit. The mobile system features a great robustness against environmental conditions. The improvements presented in this work not only enhance the resolution of the resulting models, they also lead to an intrinsic high resolution gray scale texture that fits the surface accurately without any registration step. The additional texture information may be used by the surgeon to plan the surgery and can be included in data sets for navigated surgery. These characteristics are essential for medical imaging in cranio-facial surgery and the provided features of the system are unique in the field of range sensors.

6.1 Future developments

The project of holographic facial measurement has originally been initiated to provide facial data to surgeons for a better surgery planning, so the primary aim is to put the presented system into clinical practice. This requires further automation of the process concerning for example the alignment procedure of the hologram for the optical read-out. Further noise reduction in the digitization unit is still desirable to gain reliable results for facial shapes, because facial surfaces vary in their reflectivity (which decreases with age) and the contrast of the skin pores (which increases with age). Furthermore, a fully digital recording procedure using a synthetic aperture to improve the resolution and the viewing angle of the digital recording would be a great step towards real-time applications [Mas02].

Besides facial measurement, the holographic system bears the potential for shape measurement of metallic surfaces which is relevant in many industrial applications. Bright reflexes from these surfaces lead to overexposure in optical scanning systems, and therefore, the surfaces are treated with a matting coating. Not only does this mean an additional processing step, the coating also distorts the scan result. In the holographic reconstruction, metallic reflexes appear as bright foci, in analogy to the bright reflexes from the cornea of the eyes, and can thus be detected. Because the hologram is recorded without lenses bright spots on the object surface spread out over the whole extent of the hologram and overexposure is not expected. Nevertheless, in the scan of the real image, bright spots are refocused and so in this step special care has to be taken to stay within the dynamical range of the image sensor, for example, by adjusting the power of the read-out laser. Moreover, the focus detection process in the digitized image volume has to be adapted to this task as well. A further improvement of the image resolution in the real image reconstruction down to the theoretical limit in the range of $10\ \mu\text{m}$, or even below by using shorter wavelengths, would then lead to a number of new applications.

Appendix A

Seidel aberrations in holographic imaging

In section 2.3 the general concept of wavefront matching is introduced, which allows to relate the reference and reconstruction wavefronts to the wavefront of the image wave, emerging from the hologram. Any deviation of the phase front of the reconstruction wave from the original reference wave leads to image aberrations. Aberration-free imaging is described by a Gaussian reference sphere, which belongs to the spherical wavefront of the sharpest possible image point. Third-order aberrations of the actual image phase front from this reference sphere are calculated by considering path lengths in the reconstruction geometry. While this procedure is regarded as instructive for the understanding the requirements on the hologram reconstruction geometry, the explicit calculation of the aberration terms is now given in addition for the sake of completeness, according to [Mei65].

With polar coordinates ρ and θ in the hologram plane, replacing $x = \rho \cos \theta$ and $y = \rho \sin \theta$, the third-order deviation of the actual wavefront from the Gaussian reference sphere W is given by

$$W = \frac{2\pi}{\lambda_c} \left[\begin{array}{ll} - \frac{1}{8} \rho^4 S & \text{spherical aberration} \\ + \frac{1}{2} \rho^3 (C_x \cos \theta + C_y \sin \theta) & \text{coma} \\ - \frac{1}{2} \rho^2 (A_x \cos^2 \theta + A_y \sin^2 \theta + 2A_{xy} \cos \theta \sin \theta) & \text{astigmatism} \\ - \frac{1}{4} \rho^2 F & \text{field curvature} \\ + \frac{1}{2} \rho (D_x \cos \theta + D_y \sin^2 \theta) & \text{distortion} \end{array} \right]$$

A change in the reconstruction wavelength λ_c with respect to the recording wavelength

λ_r enters in the factor $\mu = \lambda_c/\lambda_r$, a magnification of the hologram is denoted by the factor m , Z_R , a_R and b_R are the coordinates of the real Gaussian (undistorted) image point. The coefficients for the respective aberrations are

- Spherical aberration:

$$S = \frac{1}{z_c^3} - \frac{\mu}{m^4 z_o^3} + \frac{\mu}{m^4 z_r^3} - \frac{1}{Z_R^3} \quad (\text{A.1})$$

- Coma:

$$C_x = \frac{x_c}{z_c^3} - \frac{\mu x_o}{m^3 z_o^3} + \frac{\mu x_r}{m^3 z_r^3} - \frac{a_R}{Z_R^3} \quad (\text{A.2})$$

- Astigmatism:

$$A_x = \frac{x_c^2}{z_c^3} - \frac{\mu x_o^2}{m^2 z_o^3} + \frac{\mu x_r^2}{m^2 z_r^3} - \frac{a_R^2}{Z_R^3} \quad (\text{A.3})$$

- Curvature of field:

$$F = \frac{x_c^2 + y_c^2}{z_c^3} - \frac{\mu(x_o^2 + y_o^2)}{m^2 z_o^3} + \frac{\mu(x_r^2 + y_r^2)}{m^2 z_r^3} - \frac{a_R^2 + b_R^2}{Z_R^3} \quad (\text{A.4})$$

- Distortion:

$$D_x = \frac{x_c^3 + x_c y_c^2}{z_c^3} - \frac{\mu(x_o^3 + x_o y_o^2)}{m z_o^3} + \frac{\mu(x_r^3 + x_r y_r^2)}{m z_r^3} - \frac{a_R^3 + a_R b_R^2}{Z_R^3} \quad (\text{A.5})$$

Non-paraxial imaging has been included in this formalism in [Cha67]. Based on these relations, ray tracing techniques have been used to evaluate hologram aberrations for varying recording geometries [Abr69], [Lat71a], [Lat71b], and with special emphasis on aberrations appearing for $\mu \neq 1$, if m is not scaled for the same amount, a problem that becomes severe in holographic microscopy, as it was intended by Gabor [Gab48].

Bibliography

- [Abr69] I.A. Abramowitz. Evaluation of hologram imaging by ray tracing. *Applied Optics*, 8(2):403–410, 1969.
- [Abr76a] Nils Abramson. Holographic contouring by translation. *Applied Optics*, 15(4):1018–1022, 1976.
- [Abr76b] Nils Abramson. Sandwich hologram interferometry. 3: Contouring. *Applied Optics*, 15(1):200–205, 1976.
- [AFM98] Naoki Asada, Hisanaga Fujiwara, and Takashi Matsuyama. Edge and depth from focus. *International Journal of Computer Vision*, 26(2):153–163, 1998.
- [AMR04] M.D. Abramoff, P.J. Magelhaes, and S.J. Ram. Image processing with imageJ. *Biophotonics International*, 11(7):36–42, 2004.
- [Ans70] D.A. Ansley. Techniques for pulsed laser holography of people. *Applied Optics*, 9:815, 1970.
- [ART73] A.D.Gara, R.F.Majkowski, and T.T.Stapleton. Holographic system for automatic surface mapping. *Applied Optics*, 12(9):2172–2179, 1973.
- [AY71] A.D.Gara and F.T.S. Yu. Effect of emulsion thickness variations on wavefront reconstruction. *Applied Optics*, 10(6):1324–1328, 1971.
- [BHWB65] R.E. Brooks, L.O. Heflinger, R.F. Wuerker, and R.A. Briones. Holographic photography of high-speed phenomena with conventional and q-switched ruby lasers. *Appl. Phys. Lett.*, 7:92, 1965.
- [Bie03] Daniel Bielser. *A Framework for Open Surgery Simulation*. PhD thesis No. 14900. PhD thesis, Department of Computer Science, ETH Zürich, 2003.
- [Bje95] H.I. Bjelkhagen. *Silver-Halide Recording Materials for Holography and Their Processing*. Springer-Verlag, Berlin Heidelberg New York, 1995.

- [BKV88] I. Banyasz, G. Kiss, and P. Varga. Holographic image of a point source in the presence of misalignment. *Applied Optics*, 27(7):1293–1297, 1988.
- [Bla04] F. Blais. Review of 20 years of range sensor development. *Journal of Electronic Imaging*, 13(1):231–240, 2004.
- [Bon02] Jens R. Bongartz. *Hochauflösende dreidimensionale Gesichtsprüfvermessung mit kurzgepulster Holographie* [<http://www.ulb.uni-duesseldorf.de/diss/mathnat/2002/bongartz.html>]. PhD thesis, Mathematisch-Naturwissenschaftliche Fakultät der Heinrich-Heine-Universität Düsseldorf, 2002.
- [BPG] F. Blais, M. Picard, and G. Godin. Accurate 3d acquisition of freely moving objects. *Second International Symposium on 3D Data Processing, Visualization and Transmission. Thessaloniki, Greece. September 6-9, 2004. NRC 47141*.
- [BW02] Max Born and Emil Wolf. *Principles of Optics, Electromagnetic Theory of Propagation, Interference and Diffraction of Light, Seventh (Expanded) Edition*. Cambridge University Press, 2002.
- [CBL71] Robert J. Collier, Christoph B. Burckhardt, and Lawrence H. Lin. *Optical Holography*. Academic Press, New York and London, 1971.
- [CBS00] Frank Chen, Gordon M. Brown, and Mumin Song. Overview of three-dimensional shape measurement using optical methods. *Optical Engineering*, 39(1):10–22, 2000.
- [Cha67] Edwin B. Champagne. Nonparaxial imaging, magnification, and aberration properties in holography. *Journal of the Optical Society of America*, 57(1):51–55, 1967.
- [CKWvB04] D. Carl, B. Kemper, G. Wernicke, and G. von Bally. Parameter optimized digital holographic microscope for high-resolution living-cell analysis. *Applied Optics*, 43(36):6536–6544, 2004.
- [CMD99] E. Cuhe, P. Marquet, and C. Depeursinge. Simultaneous amplitude-contrast and quantitative phase-contrast microscopy by numerical reconstruction of Fresnel off-axis holograms. *Applied Optics*, 38(34):6994–7001, 1999.
- [D’A] Nicola D’Apuzzo. Modeling human faces with multi-image photogrammetry. *Three-Dimensional Image Capture and Applications V, Proc. of SPIE, San Jose, California*, 4661.

- [dFCJ01] Luciano da Fontoura Costa and Roberto Marcondes Cesar Jr. *Shape Analysis and Classification: Theory and practice*. CRC Press, Boca Raton; London; New York; Washington, D.c., 2001.
- [dFuE] Berufsgenossenschaft der Feinmechanik und Elektrotechnik. Berufsgenossenschaftliche Vorschrift für Sicherheit und Gesundheit am Arbeitsplatz. Unfallverhütungsvorschrift Laserstrahlung vom 1. April 1988 in der Fassung vom 1. Januar 1997 mit Durchführungsanweisungen vom Oktober 1995.
- [Die02] Tobias Dierig. *Gewinnung von Tiefenkarten aus Fokussereien*. PhD thesis, Fakultät für Physik und Astronomie der Ruprecht-Karls-Universität Heidelberg, 2002.
- [ELS⁺04] S. Eisebitt, J. Lüning, W.F. Schlotter, M. Lörger, O. Hellwig, W. Eberhardt, and J. Stör. Lensless imaging of magnetic nanostructures by x-ray spectroholography. *Nature*, 432:885–888, 2004.
- [FBG⁺03] S. Frey, J. Bongartz, D. Giel, A. Thelen, and P. Hering. Ultrafast holographic technique for 3d in situ documentation of cultural heritage. *Proc. SPIE Int. Soc. Opt. Eng.*, 5146:194, 2003.
- [FH98] Xiao Fang and P.R. Hobson. Effect of spherical aberration on real-image fidelity from replayed in-line holograms of underwater objects. *Applied Optics*, 37(15):3206–3214, 1998.
- [Gab48] D. Gabor. A new microscopic principle. *Nature*, 161:777–778, 1948.
- [Gab49] D. Gabor. Microscopy by reconstructed wave-fronts. *Proc. Roy. Soc. (London) A*, 197:454–487, 1949.
- [Gat86] J.W.C. Gates. The influence of holography on measurement technology. *J. Phys. E: Sci. Instrum.*, 19:998–1006, 1986.
- [Geb79] Michael Gebühr. Das Kindergrab von Windeby - Versuch einer "Rehabilitation". *Offa Berichte und Mitteilungen zur Urgeschichte, Frühgeschichte und Mittelalterarchäologie*, 36:75–107, 1979.
- [Gie03] Dominik Giel. *Hologram tomography for surface topometry* [<http://www.ulb.uni-duesseldorf.de/diss/mathnat/2003/giel.html>]. PhD thesis, Mathematisch-Naturwissenschaftliche Fakultät der Heinrich-Heine-Universität Düsseldorf, 2003.

- [GKB⁺00] F. Grawert, S. Kobras, G.W. Burr, H. Coufal, H. Hanssen, M. Riedel, C.M. Jefferson, and M. Jurich. Content-addressable holographic databases. *SPIE Conference on Critical Technologies for the Future of Computing, Paper 4109-30*, 2000.
- [G.L52] G.L.Rogers. Artificial holograms and astigmatism. *Proc. Roy. Soc. Edinburgh*, 63 A:313–325, 1952.
- [Gla02] Evgeny Gladilin. *Biomechanical modeling of soft tissue and facial expressions for craniofacial surgery planning*. PhD thesis, Fachbereich Mathematik und Informatik der Freien Universität Berlin, 2002.
- [GR05] H.C. Gill-Robinson. *The Iron Age Bog Bodies of the Archaeologisches Landesmuseum, Schloss Gottorf, Schleswig, Germany. Unpublished PhD Dissertation*. PhD thesis, Department of Anthropology, University of Manitoba, 2005.
- [Gri03] D.G. Grier. A revolution in optical manipulation. *Nature*, 424:810–816, 2003.
- [Har96] P. Hariharan. *Optical Holography: Principles, Techniques, and Applications, 2nd edition*. Cambridge Studies in Modern Optics. Cambridge University Press, 1996.
- [HH65] K. Haines and B.P. Hildebrand. Contour generation by wavefront reconstruction. *Physics Letters*, 19(1):10–11, 1965.
- [HH66] B.P. Hildebrand and K.A. Haines. The generation of three-dimensional contour maps by wavefront reconstruction. *Physics Letters*, 21(4):422–423, 1966.
- [Hin02] K.D. Hinsch. Holographic particle image velocimetry. *Meas. Sci. Technol.*, 13:R61–R72, 2002.
- [HL80] G. Haussmann and W. Lauterborn. Determination of size and position of fast moving gas bubbles in liquids by digital 3-d image processing of hologram reconstructions. *Applied Optics*, 19(20):3529–3535, 1980.
- [HO84] P. Hariharan and B.F. Oreb. Two-index holographic contouring: Application of digital techniques. *Optics Communications*, 51(3):142–144, 1984.
- [Hup00] Jürgen Huppertz. *2-D CMOS Bildsensorik mit integrierter Signalverarbeitung*. PhD thesis, University of Duisburg, Department of electrical engineering, 2000.

- [HZL85] W. Hentschel, H. Zarschizky, and W. Lauterborn. Recording and automatical analysis of pulsed off-axis holograms for determination of cavitation nuclei size spectra. *Optics Communications*, 53(2):69–73, 1985.
- [JFBRM04] A. Jesacher, S. Fürhapter, Stefan Bernet, and M. Ritsch-Marte. Diffractive optical tweezers in the Fresnel regime. *Optics Express*, 12(10):2243–2250, 2004.
- [JP89] S. Johansson and K.G. Predko. Performance of a phase-shifting speckle interferometer for measuring deformation and vibration. *J. Phys. E: Sci. Instrum.*, 22:289–292, 1989.
- [Lad04] Natalie Ladrière. Optische und chemische Aspekte der hochauflösenden, vollautomatischen Hologrammentwicklung. Diplomarbeit. Fachbereich Photoingenieurwesen und Medientechnik Fachhochschule Köln, 2004.
- [Lam82] William Lama. Optical properties of grin fiber lens arrays: Dependence on fiber length. *Applied Optics*, 21(15):2739–2746, 1982.
- [Lat71a] J.N. Latta. Computer-based analysis of hologram imagery and aberrations. I. Hologram types and their nonchromatic aberrations. *Applied Optics*, 10(3):599–608, 1971.
- [Lat71b] J.N. Latta. Computer-based analysis of hologram imagery and aberrations. II. Aberrations induced by a wavelength shift. *Applied Optics*, 10(3):609–618, 1971.
- [LFT⁺04] Natalie Ladrière, Susanne Frey, Andrea Thelen, Sven Hirsch, Jens Bongartz, Dominik Giel, and Peter Hering. Ultraschnelle holografische Gesichtsprofilvermessung mit vollautomatischer Hologrammentwicklung. *Aktuelle Methoden der Laser- und Medizinphysik. Hartmann, Kohl-Bareis, Hering, Lonsdale, Bongartz, Buzug (Herausgeber). 2. Remagener Physiktage 2004. VDE-Verlag*, pages 272–274, 2004.
- [LGC⁺04] Yi Liao, Yunbo Guo, Liangcai Cao, Xiaosu Ma, Qingsheng He, and Guofan Jin. Experiment on parallel correlated recognition of 2030 human faces based on speckle modulation. *Optics Express*, 12(17):4047–4052, 2004.
- [LKW99] W. Lauterborn, T. Kurz, and M. Wiesenfeld. *Coherent Optics, Fundamentals and Applications, 2nd printing*. Springer-Verlag, Berlin Heidelberg New York, 1999.

- [LU62] Emmet N. Leith and Juris Upatnieks. Reconstructed wavefronts and communication theory. *Journal of the Optical Society of America*, 52 (10):1123–1130, 1962.
- [LU63] Emmet N. Leith and Juris Upatnieks. Wavefront reconstruction with continuous-tone objects. *Journal of the Optical Society of America*, 53 (12):1377–1381, 1963.
- [Lug64] A. Vander Lugt. Signal detection by complex spatial filtering. *IEEE Trans. Inform. Theory*, 10:139–145, 1964.
- [Mas02] J.H. Massig. Digital off-axis holography with a synthetic aperture. *Optics letters*, 27(24):2179 – 2181, 2002.
- [Mei65] Reinhard W. Meier. Magnification and third-order aberrations in holography. *Journal of the Optical Society of America*, 55(8):987–992, 1965.
- [MNV01] E. H. W. Meijering, W. J. Niessen, and M. A. Viergever. Quantitative evaluation of convolution-based methods for medical image interpolation. *Medical Image Analysis*, 5(2):111–126, 2001.
- [MPPW04] Hui Meng, Gang Pan, Ye Pu, and Scott H. Woodward. Holographic particle velocimetry: from film to digital recording. *Meas. Sci. Technol.*, 15:673–685, 2004.
- [MR75] E.S. Marrone and W.B. Ribbens. Dual index holographic contour mapping over a large range of contour spacings. *Applied Optics*, 14(1):23–24, 1975.
- [MT80] Kazuo Matsushita and Minoru Toyama. Unevenness of illuminance caused by gradient-index fiber arrays. *Applied Optics*, 19(7):1070–1075, 1980.
- [MWLJ04] Lihong Ma, Hui Wang, Yong Li, and Hongzhen Jin. Numerical reconstruction of digital holograms for three-dimensional shape measurement. *J. Opt. A: Pure Appl. Opt.*, 6:396–400, 2004.
- [Nat02] Hologram technique to flush out features of bog body. *Nature*, 418:908, 2002.
- [NN94] Shree K. Nayar and Yasuo Nakagawa. Shape from focus. *IEEE Transactions on Pattern Analysis and Machine Intelligence*, 16(8):824–831, 1994.
- [NVSLCR04] A. Nava-Vega, L. Salas, E. Luna, and A. Cornejo-Rodriguez. Correlation algorithm to recover the phase of a test surface using phase-shifting interferometry. *Optics Express*, 12(22):5296–5306, 2004.

- [oNIRP00] International Commission on Non-Ionizing Radiation Protection. Revision of guidelines on limits of exposure to laser radiation of wavelengths between 400nm and 1.4 μm . *Health Physics*, 79(4):431–440, 2000.
- [otFifAOI01] Annual Report 2001 of the Fraunhofer Institute for Applied Optics and Precision Engineering IOF, 2001.
- [P⁺02] M.A. Papadopoulos et al. Three-dimensional craniofacial reconstruction imaging. *Oral Surgery, Oral Medicine, Oral Pathology, Oral Radiology, and Endodontics*, 93(4):382–393, 2002.
- [PM] Gang Pan and Hui Meng. Digital holographic piv for 3d flow measurement. *Proceedings of IMECE 2002, 2002 ASME International Mechanical Engineering Congress and Exposition, New Orleans, Louisiana, November 17-22, 2002*, IMECE2002-33173.
- [RA72] R.F.Majkowski and A.D.Gara. Accuracy of holographic images. *Applied Optics*, 11(8):1867–1869, 1972.
- [Ras] W.S. Rasband. ImageJ, U.S. National Institutes of Health, Bethesda, Maryland, USA, <http://rsb.info.nih.gov/ij/>, 1997-2005.
- [R.P84] R.P.Helmer. *Schädelidentifizierung durch elektronische Bildmischung*. Kriminalistik Verlag, Heidelberg, 1984.
- [S⁺03] A. Stein et al. Diffractive x-ray optics using production fabrication methods. *J. Vac. Sci. Technol. B*, 21(1):214–219, 2003.
- [SB03] A. Sinha and G. Barbastathis. Volume holographic imaging for surface metrology at long working distances. *Optics Express*, 11(24):3202–3209, 2003.
- [SBHR90] J.C. Solem, K. Boyer, W. Haddad, and C.K. Rhodes. Prospects for x-ray holography with free electron lasers. *Proc. SPIE*, 1227:105 – 115, 1990.
- [Sci02] A face for german bog man. *Science*, 297:1271, 2002.
- [SCN93] M. Subbarao, T. Choi, and Arman Nikzad. Focusing techniques. *Optical Engineering*, 32(11):2824–2836, 1993.
- [Sie67] L.D. Siebert. Front-lighted pulse laser holography. *Appl. Phys. Lett.*, 11:326, 1967.

- [Sie68] L.D. Siebert. Large-scene front-lighted hologram of a human subject. *Proc. IEEE*, 56:1242, 1968.
- [Ste68] Karl A. Stetson. Holographic surface contouring by limited depth of focus. *Applied Optics*, 7(5):987–989, 1968.
- [Stred] Henrike Stratomeier. Methods of forensic facial reconstruction. Master’s thesis, Academy of Visual Arts Maastricht, Faculty of Medicine, Maastricht University, 2004 (unpublished).
- [TBG⁺05] Andrea Thelen, Jens Bongartz, Dominik Giel, Susanne Frey, and Peter Hering. Iterative focus detection in hologram tomography. *J. Opt. Soc. Am. A*, 22(6):1176–1180, 2005.
- [The03] Andrea Thelen. Holographische Topometrie. Diplomarbeit. Universität Bonn, 2003.
- [TW63] B.A. Tozer and J.M. Webster. Holography as a measuring tool. *Journal of the Optical Society of America*, 53 (12):1377–1381, 1963.
- [Wil04] Caroline Wilkinson. *Forensic Facial Reconstruction*. Cambridge University Press, Cambridge, 2004.
- [WSN⁺00] D. Weiß, G. Schneider, B. Niemann, P. Guttman, D. Rudolph, and G. Schmahl. Computed tomography of cryogenic biological specimens based on x-ray microscopic images. *Ultramicroscopy*, 84:185 – 197, 2000.
- [WYJ03] Yuxin Wang, Wenbing Yun, and Chris Jacobsen. Achromatic Fresnel optics for wideband extreme-ultraviolet and x-ray imaging. *Nature*, 424:50–53, 2003.

Acknowledgements

It is a pleasure for me to thank some of the persons who gave me their helpful support and added valuable contributions to this work.

In the first place, I wish to thank Prof. Dr. P. Hering for giving me the opportunity to work with the holography group at the caesar foundation in Bonn, for his support, advise and encouragement, the opportunities to present my work in many places and for conceding me organizational freedom to develop my thesis.

I am grateful to Prof. Dr. G. Pretzler for taking over the part of the second referee, and I like to thank for his advise and for giving me the idea for the experiment that is realized in chapter 3.7.

I wish to acknowledge the support of the *caesar* foundation in Bonn, Germany, that provided excellent working conditions.

I sincerely thank my colleagues Andrea Thelen, Natalie Ladrière and Sven Hirsch for the steady support that released me from routine work while writing the thesis, and also for the pleasant collaboration in the past years.

I also wish to thank my former colleagues Prof. Dr. Jens Bongartz and Dr. Dominik Giel for their valuable contributions to my thesis in form of ideas and pioneering work on holographic surface measurement. Prof. Dr. Jens Bongartz is also acknowledged for providing software support for 3d visualization.

All other members of the *Holography and Laser Technology Group* have provided help whenever needed and a friendly atmosphere, which is greatly appreciated.

Many collaborators from medical, forensic and archaeological science have given support and feedback, contributed their work to a further development of the holographic system and gave valuable and sometimes spectacular opportunities to test and to demonstrate the potential of the holographic system.

In particular, I express my gratitude to Prof. Dr. Dr. C.U. Fritzeimer (University Hospital Düsseldorf, Germany) for involving us in many interesting medical applications and for the constant collaboration since the start of the holography project.

Prof. Dr. Dr. H.-F. Zeilhofer (University Hospital Basel, Switzerland) is gratefully acknowledged for supporting the establishment of the holographic system at the University hospital in Basel.

I also wish to thank Dr. Dr. K. Schwenzer (University Hospital Basel, Switzerland) for her valuable support and feedback.

I sincerely thank Henrike Stratomeier, who contributed excellent work making forensic facial reconstructions.

The fruitful cooperation with Heather Gill-Robinson, who brought the Windeby child bog body to our laboratory, is also gratefully acknowledged.

Erklärung

Hiermit erkläre ich, die vorliegende Dissertation eigenhändig und ohne unerlaubte Hilfen angefertigt und diese in der vorgelegten oder in ähnlicher Form noch keiner anderen Institution eingereicht zu haben.

Düsseldorf, den 9.6.2005

Susanne Frey